

THROUGH THE WALL TARGET DETECTION USING TEXTURAL FEATURES

A THESIS SUBMITTED TO
THE GRADUATE SCHOOL OF NATURAL AND APPLIED SCIENCES
OF
MIDDLE EAST TECHNICAL UNIVERSITY

BY

EMRE GEDİK

IN PARTIAL FULFILLMENT OF THE REQUIREMENTS
FOR
THE DEGREE OF MASTER OF SCIENCE
IN
ELECTRICAL AND ELECTRONICS ENGINEERING

SEPTEMBER 2019

Approval of the thesis:

**THROUGH THE WALL TARGET DETECTION USING TEXTURAL
FEATURES**

submitted by **EMRE GEDİK** in partial fulfillment of the requirements for the degree
of **Master of Science in Electrical and Electronics Engineering Department,**
Middle East Technical University by,

Prof. Dr. Halil Kalıpçılar
Dean, Graduate School of **Natural and Applied Sciences** _____

Prof. Dr. İlkey Ulusoy
Head of Department, **Electrical and Electronics Engineering** _____

Prof. Dr. Gözde Bozdağı Akar
Supervisor, **Electrical and Electronics Engineering, METU** _____

Prof. Dr. Gönül Turhan Sayan
Co-supervisor, **Electrical and Electronics Engineering, METU** _____

Examining Committee Members:

Prof. Dr. İlkey Ulusoy
Electrical and Electronics Engineering, METU _____

Prof. Dr. Gözde Bozdağı Akar
Electrical and Electronics Engineering, METU _____

Prof. Dr. Gönül Turhan Sayan
Electrical and Electronics Engineering, METU _____

Prof. Dr. Ziya Telatar
Electrical and Electronics Engineering, Ankara University _____

Assoc. Prof. Dr. Cüneyt F. Bazlamaçcı
Electrical and Electronics Engineering, METU _____

Date: 09.09.2019

I hereby declare that all information in this document has been obtained and presented in accordance with academic rules and ethical conduct. I also declare that, as required by these rules and conduct, I have fully cited and referenced all material and results that are not original to this work.

Name, Surname: Emre Gedik

Signature :

ABSTRACT

THROUGH THE WALL TARGET DETECTION USING TEXTURAL FEATURES

Gedik, Emre

Master of Science, Electrical and Electronics Engineering

Supervisor: Prof. Dr. Gözde Bozdağı Akar

Co-Supervisor: Prof. Dr. Gönül Turhan Sayan

September 2019, 162 pages

Through the wall imaging(TWI) is a important technology for detection and identification of human or other objects behind the wall especially for military and civilian applications. However, the clutter, multipath ghost, and wall distortions decrease the accuracy of current TWI-based human detection and identification methods. Various algorithms use various techniques such as shape-based, image-based, and physics-based techniques.

In this thesis, we summarize all the techniques used for TWI and analyze the GPR-based detection techniques and evaluate their performances with simulated data. Images are obtained by simulation using gprMax software. After, the flash effect removal, image segmentation and feature extraction methods are applied. Finally, obtained features are classified with SVM as targets or other objects. 108 different scenarios are generated and used in the evaluation of the algorithms.

Keywords: Through the Wall imaging, Human Identification, Physic-based Tech-

nique, Shape-based Technique, gprMax, Feature Extraction

ÖZ

YAPISAL ÖZELLİKLERİ KULLANARAK DUVAR ARKASI HEDEF TESPİTİ

Gedik, Emre

Yüksek Lisans, Elektrik ve Elektronik Mühendisliği Bölümü

Tez Danışmanı: Prof. Dr. Gözde Bozdağı Akar

Ortak Tez Danışmanı: Prof. Dr. Gönül Turhan Sayan

Eylül 2019 , 162 sayfa

Duvardan görüntüleme (TWI), özellikle askeri ve sivil uygulamalar için duvarın arkasındaki insan veya diğer nesnelerin algılanması ve tanımlanması için önemli bir teknolojidir. Bununla birlikte, karışıklık, çok yollu hayalet ve duvar bozulmaları, mevcut TWI tabanlı insan algılama ve tanımlama yöntemlerinin doğruluğunu azaltır. Çeşitli algoritmalar, şekil tabanlı, görüntü tabanlı ve fizik tabanlı teknikler gibi çeşitli teknikleri kullanır.

Bu tezde TWI için kullanılan tüm teknikleri özetliyor ve GPR tabanlı algılama tekniklerini analiz ediyor ve performanslarını simülasyon verileriyle değerlendiriyoruz. Görüntüler, gprMax yazılımı kullanılarak simülasyonla elde edilir. Ardından, flaş efekti kaldırma, görüntü segmentasyonu ve özellik çıkarma yöntemleri uygulanır. Son olarak, elde edilen özellikler SVM ile hedefler veya diğer nesnelere olarak sınıflandırılır. Algoritmaların değerlendirilmesinde 108 farklı senaryo oluşturulmakta ve kullanılmaktadır.

Anahtar Kelimeler: Duvardan Görüntüleme, İnsan Teşhisi, Fizik Tabanlı Teknik, Şekil Tabanlı Teknik

Mustafa Kemal'e ve Mustafa Kemal'lere

ACKNOWLEDGMENTS

The author wishes to express his deepest gratitude to his supervisor Prof. Dr. Gözde Bozdağı Akar for her guidance, advice, criticism, encouragement, and insights throughout the research.

The author would also like to thank his family for their encouragement and supports. The author would also like to thank Aselsan company for their encouragement and supports.

TABLE OF CONTENTS

ABSTRACT	v
ÖZ	vii
ACKNOWLEDGMENTS	x
TABLE OF CONTENTS	xi
LIST OF TABLES	xiv
LIST OF FIGURES	xvii
LIST OF ABBREVIATIONS	xxiii
CHAPTERS	
1 INTRODUCTION	1
1.1 Through the Wall Imaging	1
1.2 Methods and Sensors	7
1.2.1 Synthetic Aperture Radar Systems	7
1.2.1.1 SAR System Design Considerations	8
1.2.1.2 Synthetic Aperture Radar Imaging Algorithms	17
1.2.1.3 Synthetic Aperture Radar for TWRI in Literature	23
1.2.2 Doppler Radar Systems	25
1.2.2.1 Doppler Effect	26
1.2.2.2 Micro-Doppler Effect in Radar	27

1.2.2.3	Doppler Radar for Through-the-Wall in Literature	28
1.2.3	Wi-Fi RF Capturing Systems	31
1.3	Outline of Thesis	33
2	BACKGROUND	35
2.1	Ground Penetrating Radar	35
2.1.1	A-Scan	37
2.1.2	B-Scan	38
2.1.3	C-Scan	38
2.2	Reflection and Propagation Theory of Electromagnetic Signals	41
2.2.1	Reflection and Transmission of Electromagnetic Signal at the Interface between Two Different Dielectrics	41
2.2.2	Attenuation of Electromagnetic Signal Propagating Through a Medium	43
2.2.3	Velocity of Electromagnetic Signal Through a Medium	44
2.3	Current Through the Wall Target Detection and Identification Methods	44
2.3.1	Flash Effect Removal	45
2.3.2	Segmentation	47
2.3.3	Feature Extraction	48
2.3.4	Classification	51
3	METHODS USED IN THIS THESIS	55
3.1	Mean Based Flash Effect Removal for Flash Effect Removal	55
3.2	Between-Class Variance Thresholding for Image Segmentation	57
3.3	Entropy-Based Segmentation for Image Segmentation	59
3.4	K-Means Clustering for Image Segmentation	62

3.5	Textural Feature Based Method for Feature Extraction	65
3.6	Histogram of Oriented Gradients for Feature Extraction	70
3.7	Support Vector Machine for Classification	74
4	RESULTS AND DISCUSSIONS	79
4.1	Dataset and Simulation Results	79
4.2	Textural Features / HoG Features SVM Classification for Entropy Based Segmentation Images and Comparison ROC Curves	91
4.2.1	Kernel Selection and Parameter Optimization	94
4.2.2	Performance Evaluation	106
4.2.3	Comparison of Accuracy of Textural Features	111
4.3	Comparison of This Study and Reference Paper	113
5	CONCLUSION	115
	REFERENCES	117
	APPENDICES	
A	GPRMAX INPUT FILE SAMPLE	135
B	SIMULATION MODELS OF ALL 108 SCENARIOS	139
C	WALL PERMITTIVITY, OBJECT PERMITTIVITY, WALL THICKNESS, HUMAN TYPE, OBJECT TYPE, OBJECT DEPTH, AND HUMAN DEPTH OF ALL 108 SCENARIOS	143
D	IMAGES OF DIFFERENT OBJECTS	153
E	SIMULATION RESULT FOR 6 CM WALL	161

LIST OF TABLES

TABLES

Table 1.1	Sample building materials, dimensions, and permittivity at 5GHz . . .	3
Table 1.2	Dielectric constant and effective loss tangent calculation techniques	13
Table 1.3	Wideband Microstrip antenna elements for TWRI	14
Table 1.4	Comparison of Wi-Vi and UWB radar systems	33
Table 3.1	Types of kernel functions	78
Table 4.1	Electromagnetic properties of the human material in 108 scenarios .	86
Table 4.2	Electromagnetic properties of different wall types in 108 scenarios .	87
Table 4.3	Electromagnetic properties of different objects(not human) in 108 scenarios	89
Table 4.4	Different wall thickness in 108 scenarios	90
Table 4.5	Different human size in 108 scenarios	90
Table 4.6	Accuracy of SVM for group 1 textural features by using different kernels	97
Table 4.7	Accuracy of SVM for group 1 HoG features by using different kernels	98
Table 4.8	Accuracy of SVM for group 2 textural features by using different kernels	100
Table 4.9	Accuracy of SVM for group 2 HoG features by using different kernels	101

Table 4.10 Accuracy of SVM with 30 object and 30 human data for textural features by using different kernels	104
Table 4.11 Accuracy of SVM with 30 object and 30 human data for HoG features by using different kernels	105
Table 4.12 Type of feature vectors, kernel and optimum parameters for all different datasets	107
Table 4.13 Confusion matrices and accuracy values of SVM for group 1 textural, and HoG features by using polynomial kernel and optimum parameters	107
Table 4.14 Confusion matrices and accuracy values of SVM for group 2 textural, and HoG features by using polynomial kernel and optimum parameters	109
Table 4.15 Confusion matrices and accuracy values of SVM for textural, and HoG features of 30 human and 30 object data by using polynomial kernel and optimum parameters	111
Table C.1 Wall permittivity, object permittivity, wall thickness and human type of scenarios between 1 and 27	144
Table C.2 Wall permittivity, object permittivity, wall thickness and human type of scenarios between 28 and 54	145
Table C.3 Wall permittivity, object permittivity, wall thickness and human type of scenarios between 55 and 81	146
Table C.4 Wall permittivity, object permittivity, wall thickness and human type of scenarios between 82 and 108	147
Table C.5 Object type, object depth, and human depth of scenarios between 1 and 27	148
Table C.6 Object type, object depth, and human depth of scenarios between 28 and 54	149

Table C.7 Object type, object depth, and human depth of scenarios between 55 and 81	150
Table C.8 Object type, object depth, and human depth of scenarios between 82 and 108	151

LIST OF FIGURES

FIGURES

Figure 1.1	Policeman is scanning the room with terrorists and hostage[1]	2
Figure 1.2	The general principle of through the wall imaging[2]	2
Figure 1.3	UWB and narrow band spectrum[3]	5
Figure 1.4	Ridge Horn Antenna[4]	15
Figure 1.5	Impulse Radiating Antenna[4]	15
Figure 1.6	Bowtie Antenna[4]	16
Figure 1.7	Travelling of the signal between target and transceiver[5]	18
Figure 1.8	DSAR system[6]	21
Figure 1.9	SAR imaging for triangular target[6]	21
Figure 1.10	D-SAR imaging for triangular target[6]	22
Figure 1.11	Circular SAR data collection geometry[7]	23
Figure 1.12	Multi-static radar system[4]	28
Figure 1.13	Bar-graph on RADAR Flashlight[8]	30
Figure 1.14	ISAR[2]	32
Figure 2.1	Basic working principle of GPR[9]	36
Figure 2.2	Through the wall imaging environments	37

Figure 2.3	A-Scan representation[9]	38
Figure 2.4	Location of GPR antennas to obtain B-Scan	39
Figure 2.5	B-Scan representation[9]	39
Figure 2.6	Location of GPR antennas to form C-Scan	40
Figure 2.7	C-Scan[9]	40
Figure 2.8	Reflection and transmission at the air-wall boundary	42
Figure 2.9	Block diagram of received raw data processing	44
Figure 2.10	Flash effect removing of B-scan raw data	46
Figure 2.11	Flash effect removing of A-Scan raw data	46
Figure 2.12	Flash effect removal process	46
Figure 2.13	Segmentation of C-Scan data	48
Figure 2.14	Training phase of supervised learning algorithms	51
Figure 3.1	Representation of flash effects	56
Figure 3.2	Representaion of eliminating of side wall flash	56
Figure 3.3	Representation of BCV binary image	59
Figure 3.4	Representation of BCV masked image	60
Figure 3.5	Representation of entropy-based segmentation binary image	62
Figure 3.6	Representation of entropy-based segmentation masked image	63
Figure 3.7	Representation of K-means clustering binary image	65
Figure 3.8	Representation of K-means clustering masked image	66
Figure 3.9	Representation of construction of GLCM	68
Figure 3.10	Representation of image gradients	72

Figure 3.11 Representation of HoG cells	72
Figure 3.12 Representation of bin number, bin center and boundaries for B=9	73
Figure 3.13 Representation of blocks of HoG feature extraction methods	74
Figure 3.14 Example of representation of two classes applied linearly seperable SVM	76
Figure 3.15 Example of linearly non-seperable two classes	77
Figure 4.1 Comparison of speed of simulation at different parameters	82
Figure 4.2 B-Scan and C-Scan images of different discretization spatial steps	83
Figure 4.3 Representation of images at different time window values	84
Figure 4.4 Representation of time domain and power spectrum of the gaussian waveform	84
Figure 4.5 Representation of size and position of the room	85
Figure 4.6 The distance between antennas and wall, and the distance between transmitter and receiver antennas	85
Figure 4.7 Representation of forming of B-Scan and C-Scan datas	86
Figure 4.8 Effect of wall relative permittivity on C-Scan image	88
Figure 4.9 Data allocation for parameter optimization and performance evaluation	93
Figure 4.10 Data allocation for parameter optimization and performance evaluation-2	93
Figure 4.11 Parameter optimization and performance evaluation steps	94
Figure 4.12 Accuracy values of SVM for group 1 textural features by using RBF kernel	96

Figure 4.13 Accuracy values of SVM for group 1 textural features by using polynomial kernel	96
Figure 4.14 Accuracy values of SVM for group 1 HoG features by using RBF kernel	97
Figure 4.15 Accuracy values of SVM for group 1 HoG features by using polynomial kernel	98
Figure 4.16 Accuracy values of SVM for group 2 textural features by using RBF kernel	99
Figure 4.17 Accuracy values of SVM for group 2 textural features by using polynomial kernel	100
Figure 4.18 Accuracy values of SVM for group 2 HoG features by using RBF kernel	101
Figure 4.19 Accuracy values of SVM for group 2 HoG features by using polynomial kernel	102
Figure 4.20 Accuracy values of SVM with 30 human and 30 object data for textural features by using RBF kernel	103
Figure 4.21 Accuracy values of SVM with 30 human and 30 object data for textural features by using polynomial kernel	104
Figure 4.22 Accuracy values of SVM with 30 human and 30 object data for HoG features by using RBF kernel	105
Figure 4.23 Accuracy values of SVM with 30 human and 30 object data for HoG features by using polynomial kernel	106
Figure 4.24 ROC curves of the textural features/ HoG features of group 1	108
Figure 4.25 ROC curves of the textural features/ HoG features of group 2	110
Figure 4.26 ROC curves of the textural features/ HoG features of 30 object and 30 human data	112

Figure A.1	Sample of gprMax input file	136
Figure A.2	Representation of model created by example input file	136
Figure B.1	Simulation models of scenarios 1-6 and 7-12	140
Figure B.2	Simulation models of scenarios 13-18 and 19-24	140
Figure B.3	Simulation models of scenarios 25-30 and 31-36	140
Figure B.4	Simulation models of scenarios 37-42 and 43-48	141
Figure B.5	Simulation models of scenarios 49-54 and 55-60	141
Figure B.6	Simulation models of scenarios 61-66 and 67-72	141
Figure B.7	Simulation models of scenarios 73-78 and 79-84	142
Figure B.8	Simulation models of scenarios 85-90 and 91-96	142
Figure B.9	Simulation models of scenarios 97-102 and 103-108	142
Figure D.1	Images of the scenario 7 with object model table	154
Figure D.2	Images of the scenario 25 with object model prism	154
Figure D.3	Images of the scenario 37 with object model sphere with radius 2 cm	155
Figure D.4	Images of the scenario 43 with object model sphere with radius 3 cm	155
Figure D.5	Images of the scenario 49 with object model sphere with radius 4 cm	156
Figure D.6	Images of the scenario 55 with object model two sphere with radius 2 cm	156
Figure D.7	Images of the scenario 61 with object model two sphere with radius 3 cm	157
Figure D.8	Images of the scenario 67 with object model two sphere with radius 4 cm	157

Figure D.9 Images of the scenario 73 with object model such as human a	158
Figure D.10 Images of the scenario 79 with object model such as human d	158
Figure D.11 Images of the scenario 85 with object model such as human	159
Figure D.12 Images of the scenario 103 with object model two cylinder with radius 1 cm and length 10 cm	159
Figure E.1 Simulation result for 6 cm wall	162

LIST OF ABBREVIATIONS

ABBREVIATIONS

ABC	Absorbing Boundary Conditions
AFRL/IF	Air Force Research Laboratory Information Directorate
AUC	Area Under Curve
BAE	British Aerospace
BCV	Between-Class Variance
BPA	Backprojection Algorithm
CEM	Computational Electromagnetics
CS	Compressive Sensing
DARPA	Defense Advanced Research Projects Agency
DFDA	Dual-feed Dual-arm
DOJ	Department of Justice
DRDC	Defence Research and Development Canada
DSAR	Differential Synthetic Aperture Radar
DSEP	Dual-Stacked E-shaped Patch
DT	Diffraction Tomographic
EHD	Edge Histogram Descriptors
EMARS	Enhanced Motion and Ranging Sensor
ESCE	E-shaped Patch with Self-complementary Element
FDTD	Finite-Difference Time-Domain
FETD	Finite-Element Time-Domain
FFT	Fast Fourier Transform
FMCW	Frequency-Modulated Continuous Wave
GHz	Gigahertz

GLCM	Gray-level Co-occurrence Matrix
GLRLM	Gray-level Run Length Matrix
GMM	Gaussian Mixture Model
GPR	Ground Penetrating Radar
GTRI	Georgia Tech Research Institute
HMM	Hidden Markov Model
HoG	Histograms of Oriented Gradients
IFSAR	Interferometric Synthetic Aperture Radar
ISAR	Inverse Synthetic Aperture Radar
ISM	Industrial Scientific Medical
LOG	Laplacian of Gaussian
LPDA	Log-periodic Dipole Array
MFMS	Multi-feed Multi-slot
MHz	Megahertz
MIMO	Multiple-input and Multiple-output
NIJ	National Institute of Justice
PFA	Polar Format Algorithm
PML	Perfectly Matched Layer
RBF	Radial Basis Function
RCS	Radar Cross Section
RF	Radio Frequency
ROC	Receiver Operating Characteristics
SAIC	Science Applications International Corporation
SAR	Synthetic Aperture Radar
SIRE	Synchronous Impulse Reconstruction
SVM	Support Vector Machine
TEM	Transverse Electromagnetic Waves

TWI	Through the Wall Imaging
TWRI	Through the Wall Radar Imaging
TWS	Through the Wall Surveillance
UWB	Ultra-Wide Band
VSA	Volcano Smoke Antenna
VSWR	Voltage Standing Wave Ratio
WB	Wide Band
WCSS	Within-cluster Variances
Wi-Vi	Wi-Fi Vision

CHAPTER 1

INTRODUCTION

Mankind has been trying to know the unknown for many years. Our human eyes assist us with seeing objects during these investigations by the reflection of light. However, wavelengths of visible light do not allow some materials to be transparent such as opaque materials. In recent years, researchers and engineers have been working to see what is behind opaque materials such as walls by using electromagnetic waves. In literature such as [4][10], these researches are called through-the-wall imaging.

Through-the-wall imaging (TWI) and detecting are rising as a suitable innovation for giving a vision into optically obscured territories in a variety of important civilian, law enforcement and military applications [4] [5]. For instance, TWI can be utilized by police to detect and locate prisoners, prisoner-takers, and weapons in indoor environments such as in figure 1.1[1]. Also, it enables firefighters to rescue people from fires by avoiding risks. TWI can be utilized to identify buried individuals after natural disasters such as earthquakes. Furthermore, it permits distinguishing and characterizing disguised weapons and explosives and prevent a terrorist attack in military applications.

The main idea of TWI and method and sensors used for TWI will be explained in this chapter, respectively.

1.1 Through the Wall Imaging

Through the wall imaging (TWI) and detecting is rising as an important area of research and development in military and civil areas[5] [11] [8] [12] [13] [14] [15].

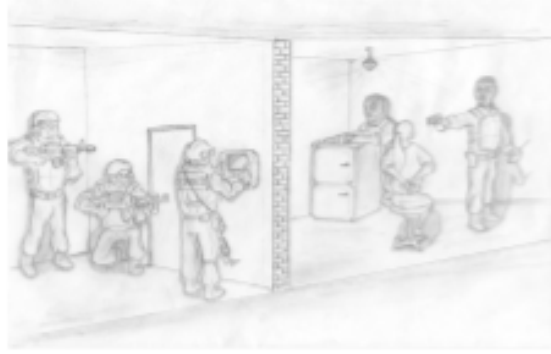


Figure 1.1: Policeman is scanning the room with terrorists and hostage[1]

TWI systems are used to scan objects through behind a wall in military and civil areas. The general principle of TWI is that electromagnetic wave is transmitted via a transmitter, penetrates through the wall, is reflected by the target, again penetrates through the wall and is received via a receiver as seen in figure 1.2[2].

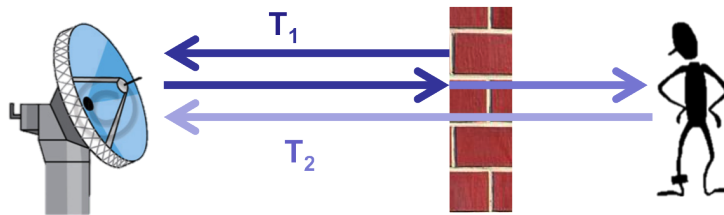


Figure 1.2: The general principle of through the wall imaging[2]

Unfortunately, electromagnetic waves can encounter with amplitude and phase distortion when they move between the transmitter and the receiver, particularly through the wall. The main reasons for these distortions are dispersion and attenuation properties of the medium and wall during propagation[4]. There are several effects that cause dispersion and attenuation such as the material of the wall, thickness of the wall, multiple reflections within the wall, bandwidth and the center frequency of the system, etc.

First of all, the material of the wall is the most important factor affecting the amplitude and phase distortions. The large relative permittivity of the wall, conductivity loss, and reflection loss, which are called electromagnetic properties of the wall and depend on the material of the wall, can cause attenuation on a wall. Also, if dispersive material is used as the wall, this may cause dispersion. Naturally, different

Table 1.1: Sample building materials, dimensions, and permittivity at 5GHz

Material	Sample Thickness (cm)	Permittivity
Drywall	1.16992	2.44
Cloth partition	5.9309	1.23
Structure wood	2.06781	2.11
Wooden door	4.44754	2.08
Plywood	1.52146	2.49
Glass	0.235661	6.40
Styrofoam	9.90702	1.11
Brick	8.71474	4.22
Concrete block	19.45	2.22
Reinforced concrete wall	60.96	-

types of wall materials cause different degrees of dispersion and attenuation based on their atomic structures. Moreover, moisture content, aggregate density, homogeneity, porosity, the density of additives, etc. play important roles in dispersion and attenuation. In literature [16] [17] [18] [19] [20] [21], there are several researches about electromagnetic properties of different types of materials such as glass, wooden door, concrete, brick, plywood, reinforced concrete, styrofoam, cloth partition, and chop wood etc. Moreover, the electrical properties of glass vary considerably with glass composition but vary very little with frequency. Temperature affects highly the electrical properties of glass because of mobility characterization for ions. In table 1.1, the values of permittivity and thickness at 5GHz are shown. Using a metal wall causes the flash effect based on the exterior wall because the signal can not propagate through the metal wall.

Secondly, multiple reflections within the wall is another factor causing the amplitude and phase distortions. Multiple reflections within the wall can cause attenuation on a wall. Multiple reflections within the wall occur stronger if the wall is heterogeneous and the wall thickness is much larger than the signal wavelength.

Then, the thickness of the wall is another factor affecting the amplitude and phase distortions. If the thick walls or lossy exterior walls are used, most of the transmitted

signal is absorbed and reflected by the wall. In this case, weak signal levels cannot be measured accurately due to noise at any level.

Finally, bandwidth and the center frequency of the system are another factors affecting the amplitude and phase distortions. At a higher frequency, conductivity loss becomes a significant attenuation factor. That is, higher frequencies result in higher attenuation. Furthermore, frequency-dependent properties of wall materials affect the propagation of electromagnetic waves through the wall. Over such a wide range of frequencies, wall acts as if diverse materials. This causes the electromagnetic wave to propagate at different speeds. If bandwidth of waves increases, the molecular dipoles of the materials can not respond and dispersion occurs, which causes loss of amplitude, signal distortions, loss of bandwidth, loss of accuracy and identification capability. The situation mentioned above can be only observed at dispersive wall materials.

There are, also, several vital issues to consider before creating TWI systems. The first thing to consider is whether moving or stationary objects will be detected. With different TWI systems, stationary or moving objects can be detected and classified. Since both stationary and moving objects cannot be detected by using the same system, one of them should be chosen by designers. In the literature, generally, ultra-wideband(UWB) radar systems[22] are used for detecting and classifying stationary objects. On the other hand, Doppler radar[23] and Wi-Fi RF capturing systems[2] are, generally, used for detecting moving objects.

Other important issues for TWI systems are whether these systems have high range resolution, low-cost, compatibility, portability, hand-held property, accessibility to non-military entities, low power, high power efficiency, and high detectability of targets. Because of these situations, a wide range of TWI systems is modeled by engineers and researchers. These systems will be mentioned in detail in the next section. Before this, what UWB radar systems, Wi-Fi RF capturing systems and Doppler radar systems are will be described briefly.

In the literature, radar and sensor systems used for TWI are UWB radar systems, Doppler radar systems, and Wi-Fi RF capturing systems. The term Ultra-Wideband (UWB) has been presented by the Defense Advanced Research Projects Agency

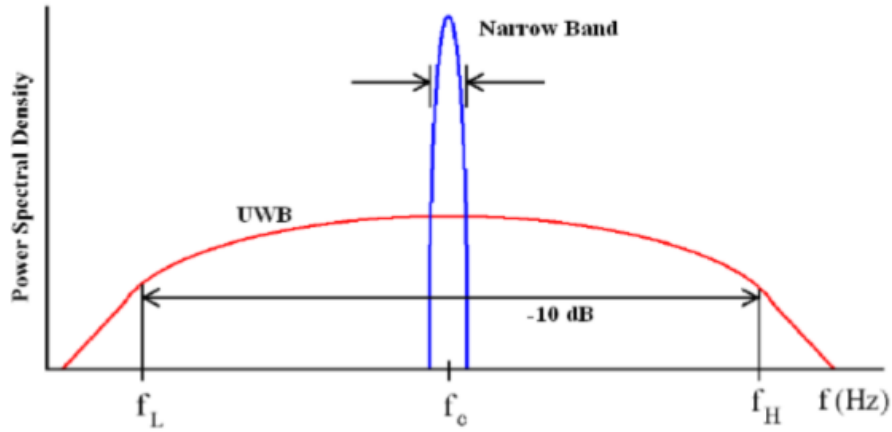


Figure 1.3: UWB and narrow band spectrum[3]

(DARPA) in a radar think about attempted in 1990. UWB innovation was also alluded by: impulse, carrier-free, and baseband technology[3]. The basic meaning of narrowband is

$$(f_H - f_L)/f_c < 1\% \quad (1.1)$$

and common definition of UWB is

$$(f_H - f_L)/f_c > 25\% \quad (1.2)$$

or

$$TotalBandwidth > 500MHz \quad (1.3)$$

as seen in figure 1.3[3]. f_H is the maximum frequency used and f_L is the minimum frequency used.

In literature, generally, short pulse duration signals at a frequency between 1-10 GHz are used as transmitter signals in UWB TWI systems. Higher frequency radar operation is not feasible in UWB TWI systems because of high attenuation and high dispersion. Another essential issue for UWB systems is the sorts of radar. In the literature, SAR[12] and GPR radar systems are utilized for UWB TWI systems. In this part, SAR and GPR will be referred to briefly.

SAR is a radar type that forms 2 and 3-dimensional images. SAR uses the movement

of the radar antenna to form images for giving a better spatial resolution. On SAR platforms, the antenna locations change with time to create synthetic aperture by the combining of the recordings from these multiple antenna positions. Because of this, the large aperture size is not necessary to obtain better spatial resolution[24] [25].

Unlike SAR, Although GPR is a geophysical method used for forming an image of subsurfaces, including rock, soil, ice, freshwater, pavements, and structures, it is also used in TWRI applications[26]. To form a GPR image, progressive pulses of radio waves are transmitted to illuminate a target scene. The receiver can then record the variations in the return signal. The GPR uses the energy change between the receiver and the transmitter for the distance measurement, whereas SAR uses time delay between transmitter and receiver for the distance measurement.

Moreover, Doppler radars are also used in TWI systems. Whereas UWB radar systems are utilized for detecting and classifying stationary objects, Doppler radar is used for detecting moving objects. A Doppler radar is a radar that uses the Doppler effect which is the difference between the observed frequency and the emitted frequency of a wave. In TWI applications, Doppler effects and micro-Doppler signature are used for motion identification.

Finally, Wi-Fi signals are typically information carriers between a transmitter and a receiver[2]. By using Wi-Fi signals, a moving object through the wall can be detected. In the literature, there is a device whose name is Wi-Vi. Wi-Vi is used for non-military applications because it has low-cost, compactibility, portability, hand-held property and low power. MIMO and ISAR techniques are used in Wi-Vi. The advantages and disadvantages of these systems will be examined in detailed in the next section.

As a result, it is necessary to summarize the subjects described above for designers. The designer must first decide whether to detect stationary objects or moving objects before designing the system. After doing this, the designer should look at the requirements. these requirements may be whether these systems have high range resolution, low-cost, compatibility, portability, hand-held property, accessibility to non-military entities, low power, high power efficiency, and high detectability of targets. Considering these, UWB radar systems, Doppler radar systems, and Wi-Fi RF capturing are utilized as TWI systems. These systems have many advantages and disadvantages in

terms of civil and military applications.

1.2 Methods and Sensors

Different applications in the civil and defense industry have gained a reputation for detecting objects behind walls and doors, or generally behind opaque obstacles, using electromagnetic waves[27][28]. In recent years, many studies have been conducted to detect moving or stationary objects in indoor environments. In these studies, there is no system design for detecting both moving objects and stationary objects. According to the selection, the radar and sensor type to be used change. For example, SAR and GPR systems can be used to detect stationary objects, while Doppler radar and Wi-Fi RF capturing systems can be used to detect moving objects. Another point to be considered during system design is whether these systems have high range resolution, low-cost, compatibility, portability, hand-held property, accessibility to non-military entities, low power, high power efficiency, and high detectability of targets. According to the above-mentioned requirements, many methods and sensors are used in TWI applications. In this section, methods and sensors which are utilized in these works will be referred to detailed. These systems are SAR, GPR, Doppler Radars and Wi-Fi RF capturing. Advantage and disadvantage of these systems will be mentioned.

1.2.1 Synthetic Aperture Radar Systems

In the 1950s, an advancement innovation, which is called Synthetic Aperture Radar, was first presented. Synthetic aperture radar(SAR) is a sort of radar, which can be utilized to form two dimensional and three-dimensional image of objects[29]. The first thing to know about SAR is that SAR uses the motion of the radar antenna. To obtain a SAR image, progressive short duration pulses are transmitted to the target scene, and the target scene is illuminated and the echo of each pulse is recorded and received by the receiver. On SAR platforms, the antenna locations change with time. Radar echoes are recorded successively. These echoes are combined by using signal processing algorithms. This process forms the synthetic antenna aperture and provides higher resolution images than real aperture antenna [24] [25].

SAR systems are referred to as UWB radar systems because they use UWB signals. As known, SAR and other UWB radars differ from each other due to their aperture structure. SAR systems produce the image by creating the synthetic antenna aperture, while other UWB systems create the image with the real aperture antenna structure. This gives SAR systems a larger antenna aperture than other UWB radar systems. As known, the larger apertures provide a higher image resolution. Compared to other UWB radar systems, synthetic aperture radar produces finer azimuth resolution without requiring large-size physical antenna since SAR uses the motion of the radar antenna[4]. This gives SAR systems to compactibility, compressibility and low-profile. As a result, SAR systems are used more in TWRI applications because they provide higher spatial resolutions in a more compact, lower profile and more compressible manner than other UWB TWI systems.

SAR systems are suitable for TWI for some reasons. One of them is the development of radar and signal processing technology which can be applied to SAR systems. Another point is that SAR radar works at low frequency, generally lower than 4GHz, to penetrate lossy wall because high frequencies cause high wall losses. However, SAR running at these frequencies provide lower spatial resolution. Therefore, at these frequencies, relatively large bandwidth(short-duration transient pulses) and large antenna apertures are needed to obtain higher spatial resolution. SAR systems which are current implementations employ wideband waveforms and large apertures.

In this section, SAR systems, which are used for TWRI, will be examined in detail. Before examining SAR systems in detail, some TWRI system design considerations, which are the briefly higher spatial resolution, understanding of physics of wave propagation, electromagnetic modeling and measurement of composite walls, and comparisons of antenna and antenna arrays, will be examined in section 1.2.1.1.

1.2.1.1 SAR System Design Considerations

TWRI System Design Considerations are an important issue that must be done before starting the system design by designers and researchers. To avoid mistakes, some considerations must be taken into account and causes must be well known. First of all, the model of propagation of the electromagnetic wave sent from the SAR system

should be known, the effects that cause the deterioration of this electromagnetic wave must be calculated. Moreover, environmental factors such as wall parameters should also be known, and taken into account. Furthermore, dielectric losses and conduction losses are other important issues for SAR system design consideration. These subjects will be explained in detail in this section.

As known, in SAR systems, cross-range resolution is limited by the antenna beamwidth and frequency, and downrange resolution is limited by bandwidth. Antenna beamwidth, frequency, and bandwidth depend on types of antenna. As a result, the type of antenna used influences the spatial resolution of the formed image. The effect of types of the antenna will be mentioned in detail in this section.

Wall parameters, Propagation Models, and Losses

Researchers and engineers consider the frequency range of about 1-4 GHz as the optimal frequency for SAR imaging, so that wideband and ultra-wideband system design becomes mandatory for having a better quality image. Because of this, knowing of the propagation characteristics of wideband and UWB signals is required for the optimal design. Losses, signal dispersion models and signal attenuation models, which depend on wall parameters and system frequency, must be known accurately to model propagation of electromagnetic waves. However, many aspects of UWB-based communication, which are propagation models, losses, and wall parameters, has not been yet investigated so much in literature. In this part, some researches, which are [4] and [30], will be referred to these issues.

In [30], important parameters and propagation of electromagnetic waves through a lossy dielectric material are defined. Assume that a TEM plane wave propagating +z direction can be represented as phasor expression. This expression is in equation 1.4

$$E(z, \omega) = E_0 e^{-\gamma z} \tag{1.4}$$

In equation 1.4, γ represents complex propagation constant given as equation 1.5.

$$\gamma(\omega) = \alpha(\omega) + j\beta(\omega) = j\omega\sqrt{\mu\epsilon} \quad (1.5)$$

where α represents attenuation constant, β denotes the phase constant, ϵ is permittivity and μ is permeability. Generally, walls are non-magnetic for TWRI applications so

$$\mu = \mu_r\mu_0 \approx \mu_0 \quad (1.6)$$

where μ_r is relative permeability.

In equation 1.7, complex permittivity is defined as

$$\epsilon(\omega) = \epsilon'(\omega) - j\epsilon''(\omega) \quad (1.7)$$

where ϵ' and ϵ'' are, respectively, real permittivity and dielectric loss, which can be also called as loss tangent.

In equations 1.8 and 1.9, real permittivity and loss tangent are, respectively, defined as

$$\epsilon' = \epsilon_r\epsilon_0 \quad (1.8)$$

$$p(\omega) = \tan\delta = \epsilon''/\epsilon' \quad (1.9)$$

where ϵ_r is relative permittivity and always greater than 1. The conductivity loss can be added to complex permittivity as imaginary term seen in equation 1.10.

$$\epsilon(\omega) = \epsilon'(\omega) - j(\epsilon''(\omega) + \sigma/\omega) \quad (1.10)$$

where $\sigma(\omega)$ is the macroscopic conductivity of the material of interest. Separation of conductivity loss and dielectric loss is not as easy as assumed. However, two losses may be combined an effective loss tangent as seen in equation 1.11.

$$p_e = \frac{\epsilon'' + \sigma/\omega}{\epsilon'} \quad (1.11)$$

Complex permittivity can be obtained in terms of loss tangent by combining equations 1.10 and 1.11 as seen equation 1.12.

$$\epsilon(\omega) = \epsilon'(\omega)(1 - jp_e(\omega)) \quad (1.12)$$

A complex effective relative permittivity can now be defined as

$$\epsilon_{re}(\omega) = \epsilon_r(\omega)(1 - jp_e(\omega)) \quad (1.13)$$

Angular frequency can now be defined as

$$\omega = 2\pi f \quad (1.14)$$

The speed of light(c) in a vacuum can be defined as

$$c = 1/\sqrt{\mu_0\epsilon_0} \quad (1.15)$$

The complex propagation constant can be defined again by combining equations 1.5, 1.6, 1.8, 1.12 and 1.15 as

$$\gamma = \frac{j\omega}{c}\sqrt{\epsilon_{re}} = \frac{j\omega}{c}\sqrt{\epsilon_r(1 - jp_e)} \quad (1.16)$$

The attenuation constant and the phase constant can be defined, respectively, by com-

binning equations 1.5 and 1.16 as

$$\alpha(\omega) = \frac{\omega}{c} \sqrt{\frac{\epsilon_r}{2} [\sqrt{1 + p_e^2} - 1]} \quad (1.17)$$

$$\beta(\omega) = \frac{\omega}{c} \sqrt{\frac{\epsilon_r}{2} [\sqrt{1 + p_e^2} + 1]} \quad (1.18)$$

Hence, as seen from the equation mentioned above, the dielectric constant and the effective loss tangent must be calculated properly to characterize any wall material[30]. In [30], there are two different methods for calculating dielectric constant and the effective loss tangent, which are single-pass technique and multiple-pass technique. This techniques will not be mentioned here.

As a result, propagation models, wall parameters and losses were explained in this part until now. While explaining the propagation model, the TEM plane wave moving in the z-direction is discussed. By using the TEM plane wave, the complex propagation constant, the phase constant, the complex permittivity, the dielectric constant, the effective loss tangent, and the attenuation constant were described. Here, the main concern for designers is the attenuation constant. Designers should know well what attenuation constant is connected to. As shown in equation 1.17, attenuation constant is proportional to the dielectric constant, the loss tangent and the central frequency of the system. Also, the dielectric constant and loss tangent are also proportional to the frequency. As it is understood from this point of view, the choice of system frequency is very important for the UWB propagation model. The dielectric constant and effective loss tangent is calculated with two different techniques, which are single-pass technique and multiple-pass technique. In [30], there is a comparison of two methods. Moreover, the techniques used to calculate dielectric constant and effective loss tangent are shown in table 1.2.

Types of Antennas for SAR

In general, a SAR system for TWRI is expected to meet satisfactory requirements when designing. These requirements are to obtain high-quality images, to detect a sta-

Table 1.2: Dielectric constant and effective loss tangent calculation techniques

Techniques
Single-pass technique
Multiple-pass technique with exact solution
Multiple-pass technique with approximate solution

tionary object with a minimum error, to have a small dimension and to be cheap[31]. High spatial resolution is required for the SAR system to obtain high image quality and detect stationary objects with minimum error. In general, for a high-resolution SAR system, transmitter and receiver antennas should be operated over a wide frequency band with large aperture size as is known. Furthermore, in order for the designed SAR system to be small and low-cost, the transmitter and receiver antennas used should be physically small and low-profile. As a result, it is clear from the mentioned above that the selection of the antenna to be used in the SAR system is very important. In this part, some of wideband and UWB antennas used in SAR systems will be briefly mentioned. The advantages and disadvantages of these antennas will also be described.

Whereas Microstrip and other printed-type antennas provide physically small, low-profile, low-cost and lightweight requirements, they do not satisfy wide bandwidth. These antenna types suffer from narrow bandwidth in SAR systems [31]. However, this problem can be eliminated with the help of various bandwidth enhancement techniques. Bandwidth enhancement techniques are given detailed for microstrip antenna in [32], [33] and [34]. In general, these techniques result in a bandwidth of 10% to about 50%[4]. These techniques will not be described here. Despite bandwidth limitations, microstrip-based antennas are used for many TWRI applications because they provide nearly unidirectional coverage[4]. In this part, two types of antennas designed using the above-mentioned bandwidth enhancement technique will be described briefly, which are slotted microstrip patch antennas and multi-feed microstrip antennas. Firstly, the examples of the slotted microstrip patch antenna are U-shaped[35] [36], E-shaped slotted patch antennas[37], dual-stacked E-shaped patch(DSEP)[38][39] and E-shaped patch with self-complementary element(ESCE)

Table 1.3: Wideband Microstrip antenna elements for TWRI

Antenna	Thickness(λ_0)	Footprint($\lambda_0 \times \lambda_0$)	Bandwidth(%)	Gain within the Band
Stacked patch	0.093	0.35x0.37	27	>7.3dBi
U-patch	0.096	0.39x0.44	30	>6.1dBi
E-shaped patch	0.083	0.36x0.43	31	>6.58dBi
Dual-stacked E-patch	0.12	0.38x0.41	40	>7dBi
MFMS patch	0.096	0.41x0.50	51	>4.9dBi
DFDA patch	0.099	0.24x0.31	70	>2dBi

[37][38]. In terms of construction, the E-shaped patch antenna is simpler than a U-slot microstrip patch antenna. Satisfactory performances can be obtained by adjusting the length, the width and the position of the slots. Then, the examples of the multi-feed multi-slot antennas are MFMS and DFDA. Thickness, footprint, bandwidth, and gain within the band of microstrip antennas are shown in table 1.3[31][38][4]. The values in table 1.3 should be evaluated in terms of the above-mentioned requirements. In terms of these requirements, the DFDA patch antenna draws attention. Considering the size, it has the smallest footprint between the specified antenna types. However, although it appears to be disadvantageous for thickness, its thickness is not very different from the thickness of other antenna types. Here, the DFDA patch antenna has a very wide frequency bandwidth for microstrip-type antennas. Therefore, in high-resolution applications, the DFDA patch antennas are more advantageous than other microstrip-type antennas. Although there are such advantages, the DFDA patch antennas have a major disadvantage in terms of gain within the band.

Different from microstrip antennas, another antenna group commonly used in SAR applications is UWB antennas. In general, UWB antennas elements provide a minimum of 2:1 bandwidth. Many examples of UWB antenna types may be given but suitable antenna types for SAR applications are antennas such as corrugated horn antenna, biconical antenna, ridge horn antenna, impulse radiating antenna, log-periodic antenna, bowtie antenna, printed spiral antenna, volcano smoke antenna, diamond dipole antenna, circular E and circular E complementary monopoles and Vivaldi antennas.

In the following, the geometry and characteristics of some of these antennas will be

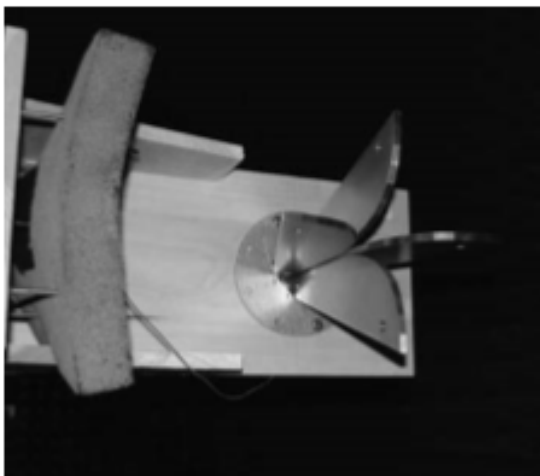


Figure 1.4: Ridge Horn Antenna[4]

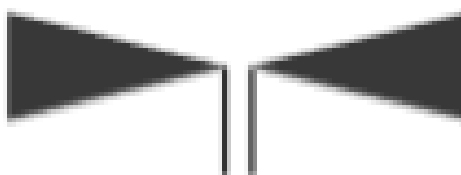


Figure 1.5: Impulse Radiating Antenna[4]

discussed. The discussion will be started with ridge horn antenna.

A standard horn antenna does not provide the bandwidth which is required for SAR applications. However, the ridge horn antenna provides the bandwidth required by reducing the required size. Moreover, standard rectangular horn antennas are heavy, bulky and not suitable for SAR applications whereas the ridge horn antenna is most suitable when it is used as a single receive element for SAR applications. Ridge horn antennas have 9:1 impedance bandwidth, which operates between 700 MHz and 6GHz. Example of ridge horn antenna can be seen in figure 1.4 [4].

Secondly, impulse radiating antenna radiates a short pulse with a narrow beam. An example of this antenna, which radiates short pulse with a UWB beam, can be seen in figure 1.5 for SAR developed by Eureka Aerospace [4].

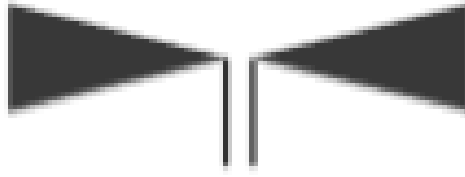


Figure 1.6: Bowtie Antenna[4]

Thirdly, the log-periodic antennas consist of the log-periodic dipole array (LPDA), which is dipole elements whose length, diameter and spacing are logarithmic. Since it has a large length, it is not suitable for UWB operations when using as receiving elements.

Then, bowtie antennas are examined detailed in [40] and [41]. In the bowtie antenna, tapering off the diameter of a dipole antenna increases its bandwidth. Bowtie antenna can be seen in figure 1.6 [4].

Moreover, the printed spiral antenna is a frequency-independent antenna, which can be completely specified by an angle. This antenna is capable of achieving a fractional bandwidth of $2/3$. This antenna operates frequency between 300 MHz and 6GHz [4].

Then, the volcano smoke antenna(VSA), firstly, is proposed by John Kraus in [42]. The UWB performance of VSA is quite good. Generally, a standard VSA has produced an operating bandwidth of 10:1, from 1.5 to 15 GHz [4].

Finally, between these antennas, Vivaldi antennas are excellent candidates for various SAR and TWRI applications [43][44][45][46]. The Vivaldi antenna is suitable due to its simplicity, wide bandwidth, high gain at microwave frequencies. Moreover, Vivaldi antennas minimize the antenna distortion of the shape of the transmitted UWB pulses.

As a result, many of the antennas used in SAR and TWRI applications were mentioned. DFDA patch antennas are the most suitable in terms of bandwidth and footprint between microstrip antennas for SAR and TWRI applications. Moreover, between UWB antennas, Vivaldi antennas are excellent candidates for SAR and TWRI

applications in terms of wide bandwidth, high gain, and simplicity[4].

1.2.1.2 Synthetic Aperture Radar Imaging Algorithms

Synthetic Aperture Beamforming for Through-the-Wall Imaging

In this part, synthetic aperture beamforming will be specified and formulated by using ray perturbation methods. In [5], synthetic aperture beamforming that accounts for the effects of transmission through a single uniform wall is presented by using ray perturbation theory. In this system, a single transceiver is used for realizing the M-element array by moving this transceiver, which forms a synthetic array aperture. Assume that the wall is uniform with a thickness d and a dielectric constant is ϵ . The transceiver is moving parallel to the x-axis in the (x,z) plane whereas the wall is located through (x,y) plane. Assume that, mth location of transceiver is at $x_{tm} = (x_{tm}, -z_{off})$, illuminate the scene with a wideband signal $s(t)$. Assume that a single point target is located at $x_p = (x_p, z_p)$ and $r_m(t)$ is measured at mth location of transceiver. Moreover, $r_m(t)$ is given by

$$r_m(t) = a(x_p)s(t - \tau_{mp}) \quad (1.19)$$

where $a(x_p)$ is the complex reflectivity of the point target and τ_{mp} is the propagation delay encountered by the signal traveling between the same transceiver. As shown in figure 1.7, the propagation delay is given by

$$\tau_{mp} = \frac{2I_{mp,air,1}}{c} + \frac{2I_{mp,wall}}{v} + \frac{2I_{mp,air,2}}{c} \quad (1.20)$$

$$v = \frac{c}{\sqrt{\epsilon}} \quad (1.21)$$

where c is the speed of light, v is the speed of propagation through the wall, $I_{mp,air,1}$ is the traveling distance of the signal before the wall, $I_{mp,wall}$ is the traveling distance of the signal through the wall, $I_{mp,air,2}$ is the traveling distance of the signal after the wall. This process is repeated for all locations of the transceivers.

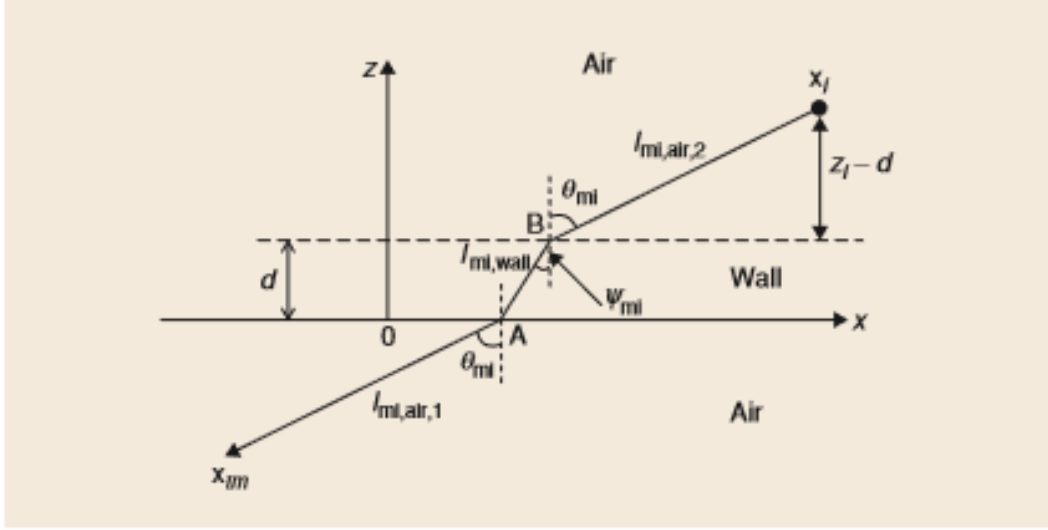


Figure 1.7: Travelling of the signal between target and transceiver[5]

Then, (x,z) plane is divided into a finite number of pixels. Assume that the image pixel is located at $x_q = (x_q, z_q)$. The complex composite signal of received from the pixel is obtained by time delaying and weighting M measurements and summing the results. The equations are given by

$$y_q(t) = \sum_{m=1}^M [w_m r(t + \tau_{mq})] \quad (1.22)$$

$$y_q(t) = \sum_{m=1}^M [a(x_p) w_m s(t + \tau_{mq} - \tau_{mp})] \quad (1.23)$$

where w_m is the weight and τ_{mq} is the focusing delay applied to the output of the m th location of transceiver. The complex amplitude image value $I(x_q)$ for the pixel located at x_q is obtained by passing the signal $y_q(t)$ through a filter matched to the transmitted pulse $s(t)$ and sampling the output of the filter as follows[5]:

$$I(x_q) = (y_q(t) * h(t))|_{t=0} = \left(\sum_{m=1}^M [a(x_p) w_m s(t + \tau_{mq} - \tau_{mp})] * h(t) \right)|_{t=0} \quad (1.24)$$

where $h(t) = s^*(-t)$ is the impulse response of the matched filter. This process is

applied to all pixels in the region to obtain the image.

For P point target scene, $I(x_q)$ is given by

$$I(x_q) = \left(\sum_{p=1}^P \sum_{m=1}^M [a(x_p) w_m s(t + \tau_{mq} - \tau_{mp})] \right) * h(t) \Big|_{t=0} \quad (1.25)$$

Moreover, focusing delay can be calculated by using Snell's law. The equation obtained to calculate focusing delay is the transcendental equation and can be solved numerically. In [5], there is a practical example.

2D synthetic aperture beamforming can be extended 3D beamforming by moving transceiver to form a planar array. 3-D beamforming provides information about the length, height, and width of the target. For 3-D imaging, (x,y,z) plane is divided into a finite number of voxels, which is volume pixels. 3D beamforming can be reviewed in [47]. 2-D imaging algorithms can be applied directly with some modification for 3-D imaging.

As a result, in this part, we have examined and formulated a 2-D beamforming technique for a single uniform wall whose thickness and dielectric constant is known. Since it is accepted that the properties of the wall are known in the techniques examined here, the reduction of the propagation speed of the wave and the wave refraction can be easily modeled. However, unless the properties of the wall are known, the method of beamforming described above will not work. Instead, a beamforming algorithm can be developed using the work that appears in references [48] and [49].

Differential Synthetic Aperture Radar

In the previous part, through-the-wall imaging was obtained by using a synthetic aperture beamforming algorithm. However, in the image obtained by this algorithm, the reflection of the wall is visible, which is called the flash effect. Flash effect occurs due to sidelobes of signals directly reflected from the wall. This situation makes the detection of relatively small objects such as human behind the wall difficult. To remove wall reflection and increase the signal-to-clutter ratio, different approaches have been proposed in [50][51][52]. Moreover, Differential Synthetic Aperture Radar(DSAR)

is proposed as seen in the [6] to reduce the flash effect. In this part, the differential SAR method will be examined and formulated by using reference [6]. The DSAR method utilizes a frequency-modulated continuous-wave radar system to form an image. In this approach, unlike synthetic aperture beamforming, the image is formed by subtracting two consecutive signals instead of individual backscattered signals. This way, since the wall reflection at every consecutive two points are the same, the flash effect is eliminated without the need to know the wall parameters.

In backscattering SAR imaging systems, the flash effect is eliminated by modeling the wall parameters and wall. However, image quality does not increase as expected due to differences in wall modeling and the actual wall. On the other hand, the DSAR technique eliminates the flash effect without the need to model the wall by subtracting two consecutive signals. Since the reflection of the wall is generally similar at different consecutive points, difference signals work to eliminate the flash effect. In general, the idea of using the difference of signals is utilized in the identification of moving objects for narrow-band and narrow-beam systems. However, there are two major differences between the narrow-band and narrow-beam systems and DSAR. These are the ultrawideband waveform used in the DSAR system and the wide-angle and nearfield-field focusing[6]. Here, the main issue is to remove wall glint and maintain and reconstruct the image of stationary point targets. DSAR system can be seen in figure 1.8.

[6].

As shown in figure 1.8, the reflections of the wall are very similar in the consecutive antenna positions whereas the reflections from the point target are not alike due to the phase difference.

Moreover, in figure 1.9 and figure 1.10 taken by reference [6], respectively, SAR imaging for triangular target and D-SAR imaging for triangular target can be seen. As seen from figures, the D-SAR technique improves image quality by eliminating the flash effect.

As a result, in this part, the D-SAR method which reduces the flash effect without modeling the wall and wall parameters were examined. Wall reflection was elimi-

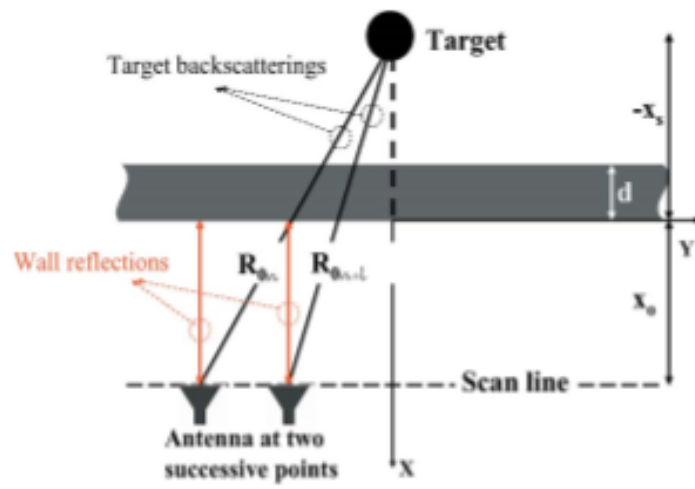


Figure 1.8: DSAR system[6]

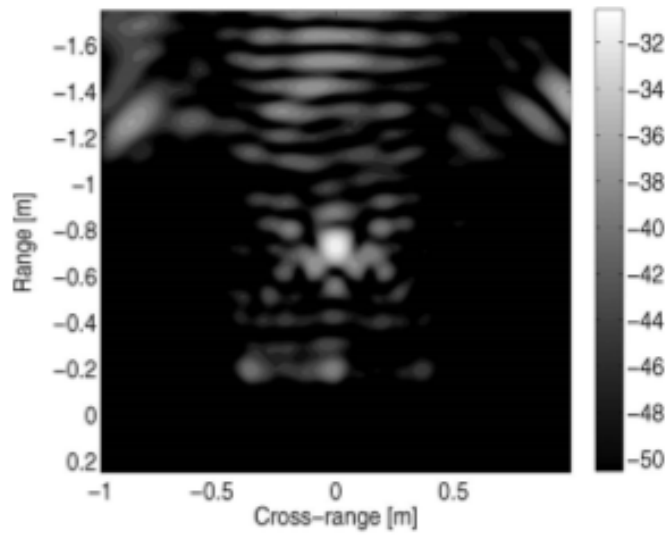


Figure 1.9: SAR imaging for triangular target[6]

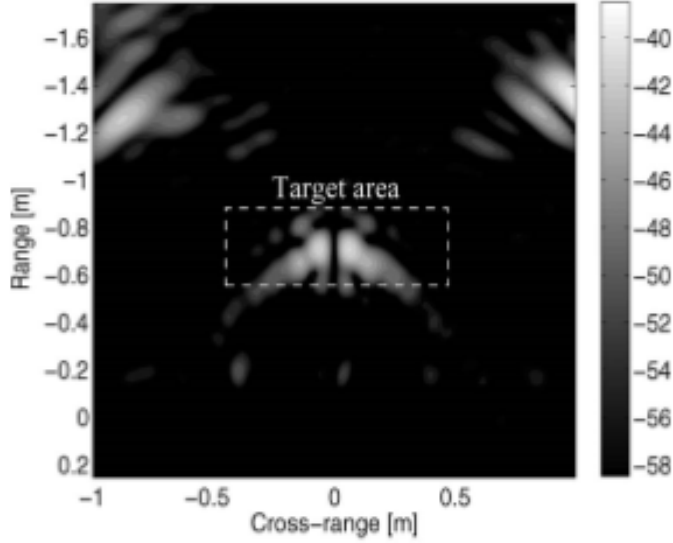


Figure 1.10: D-SAR imaging for triangular target[6]

nated by taking the difference of signals from two consecutive antennas. In systems where the wall cannot be modeled correctly, the D-SAR method increases the image quality more than the SAR method.

Two-pass Interferometric Circular Synthetic Aperture Radar

In this part, two-pass interferometric circular synthetic aperture radar (IFSAR) for TWI described in reference [7] will be examined. Unlike other algorithms mentioned above, an airborne Synthetic Aperture Radar(SAR) system is utilized here. The measurement in this system is carried out by the radar in the aircraft following a circular path above the building. As seen in figure 1.11, θ and ϕ , respectively, refer to elevation and azimuth angle of aircraft. Measurements at θ_1 and θ_2 , so closely each other, enables interferometric SAR (IFSAR) processing techniques. Moreover, in [7], estimation and feature extraction algorithms are mentioned detailed. However, in this part, these algorithms will not be referred to.

SAR system utilized in [7] collects coherent backscatter measurements on circular aperture over azimuth angles Φ covering $[0, 2\pi]$ at two closely spaced elevation angles $(\theta_1, \theta_2) = (\theta_c - \Delta\theta/2, \theta_c + \Delta\theta/2)$. Circular SAR data collection geometry can be seen in figure 1.11. For sufficiently high frequencies, the returns from a complex scat-

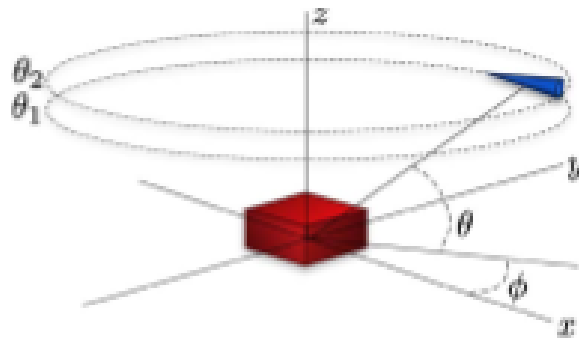


Figure 1.11: Circular SAR data collection geometry[7]

tering object can be expressed as the sum of the responses from individual scattering mechanisms[7][53].

As a result, in this part, interferometric circular synthetic aperture radar was briefly examined. The system used in this part is integrated into the aircraft and the image is obtained by the circular movement of the aircraft. The two consecutive elevation angles must be nearly identical to apply the IFSAR method.

1.2.1.3 Synthetic Aperture Radar for TWRI in Literature

SAR is a UWB radar type and is the most preferred radar in TWI applications among UWB radar types. Popular SAR algorithms used in TWI applications are described in 1.2.1.2. In this section, TWI studies with UWB radar types other than SAR and other studies with SAR will be mentioned in the literature. However, in this section, the applications mentioned in the literature will only be given as a reference and no detailed examination will be made.

[54], [55], [56], [57], [58], [59], and [60] can be browsed to gain a deeper view of the SAR. In most of the applications mentioned in the literature, simulation results are available instead of actual systems, because the actual construction of the systems is expensive for SAR imaging for TWI. Several computational electromagnetic (CEM) codes have been used specifically for modeling scenarios of interest in TWRI[4]. AFDTD[61], developed by ARL, and XFDTD[62], developed by Rem-

com, are both based on the finite-difference time-domain (FDTD) method. Large models of a building were reported by the Lawrence Livermore National Laboratory via a finite-element time-domain(FETD) algorithm[63]. Other codes, based on ray-tracing and other high-frequency methods, include Xpatch[64], developed by Science Applications International Corporation (SAIC) under a grant from the U.S. Air Force. AFDTD and Xpatch methods for TWRI medium were directly applied in [65][66][67][68]. Moreover, computer simulation of the human body radar signature for TWI by using AFDTD method is presented in [69].

Also, various simulation studies have been made to model indoor environments and compile images. For example, in [70], a generalized Green's function-based approach for the imaging of targets behind the wall with compressive sensing(CS) is proposed for SAR and MIMO radar. Simulation results can be examined in [70]. Moreover, in [71], TWRI simulation for the complex room is conducted by Arm Research Laboratory. The linear inverse scattering algorithm, another through-the-wall imaging algorithm, is described, formulated and simulated in [72]. In [73], a two-dimensional (2D) diffraction tomographic (DT) algorithm based on the first-order Born approximation is proposed for through-the-wall radar imaging (TWRI). Moreover, various simulation studies of through-the-wall imaging can be seen in references [74], [75], [76], and [77].

In the literature, there are a lot of simulation studies about through-the-wall imaging. Some of these are referenced above. In general, studies on TWRI remain in the simulation stage since the actual system to be created is expensive. Studies that do not remain in the simulation stage are generally tried to be implemented in the laboratory. However, these studies in the laboratory are not intended to make a device. These studies are mostly aimed at obtaining real data. Moreover, it is available on devices made with UWB and SAR systems. In this section, experimental studies in the laboratory and implementation of devices will be given as a reference. For example, in [78], the experimental setup was established and the image was obtained by wideband synthetic aperture beamforming method. In [79], the construction of SAR images is developed by using analytical, numerical and experimental techniques. Moreover, a 3-D diffraction tomographic algorithm is proposed for real-time through-the-wall radar imaging (TWRI). The algorithm, simulation results and experimental results

are mentioned in [80]. Moreover, various experimental studies of through-the-wall imaging can be seen in references [81], [82], [83], [84], [85], [86], [87], [88], [89], [90].

As mentioned above, besides the experimental studies, there are also systems and devices for UWB TWRI. For example, in [91], the SIRE radar system designed by ARL is mentioned. SIRE radar is a vehicle-borne UWB impulse-based system, designed to create SAR images in various configurations. Moreover, in [92], TWI is created using the MIMO radar system designed by DRDC.

1.2.2 Doppler Radar Systems

A Doppler radar is a type of radar that uses the Doppler effect to generate velocity and motion information about objects. A microwave signal is sent to the desired destination and the motion of the object is analyzed, depending on how the frequency of the returning signal changes. This change gives direct and very accurate measurements of the speed of a target.

As known, the detection of a stationary object was examined by using synthetic aperture radar systems. In this part, detection of moving object will be examined by using doppler radar systems. The detection of the motion of the object behind an opaque material is an important part of through-the-wall radar applications. Examples of such applications are the location of humans in post-earthquake or explosion scenarios, surveillance, and monitoring of hostages, evaluation of security threats, etc. The movement of the chest during a person's inspiration process is detected by the doppler radar. This is done by the measurement of micro-Doppler signatures of human movements for indoor environments. In the presence of the wall, the micro-Doppler effect has a similar form as in free-space. However, the only thing that changes is the absolute value of the micro-Doppler signature. As a result, radar micro-Doppler signature can be used to detect human motions[4].

In this section, before examining the samples of Doppler radar systems, the Doppler effect and the micro-Doppler signature, which form the basis of the doppler radar, will be discussed.

1.2.2.1 Doppler Effect

Doppler effect, which forms the basis of doppler radars, should be mentioned before going on to explain doppler radar systems. The Doppler effect changes in frequency or wavelength of a wave relative to an observer moving relative to the wave source[93]. Since the source of the waves moves towards the observer, each successive wave peak is emitted from the position close to the observer by the previous wave. Therefore, each wave takes less time than the previous wave to reach the observer. Therefore, the time between the successive wave peaks in the observer decreases and causes an increase in frequency. As they travel, the distance between consecutive wavefronts decreases, so the waves are collected together[94][95]. A similar situation applies when the source of the wave moves away from the observer. However, in this case, the waves are spread out instead of gathering together.

Doppler frequency is the difference between the observed frequency and the emitted frequency of a moving observer. Doppler frequency is given by

$$f_d = f_r - f_t \quad (1.26)$$

where f_r and f_t represent, respectively, the observed frequency and the emitted frequency of a moving observer. f_r is given by

$$f_r = f_t \left(\frac{c + v}{c - v} \right) \quad (1.27)$$

By combining equations 1.26 and 1.27, Doppler frequency is given by

$$f_d = 2v \left(\frac{f_t}{c - v} \right) \quad (1.28)$$

Motion and velocity are detected using the above-mentioned doppler effect. Using Doppler radars, the velocity of aircrafts and cars is measured. In addition, the doppler effect is exploited for the moving target indication.

1.2.2.2 Micro-Doppler Effect in Radar

In most cases, a target may have oscillating motion such as a man waving his arms, a rotating propeller of a helicopter, etc. This causes frequency modulation over the returned echo signal. This frequency modulation is combined with the doppler frequency shift and called micro-Doppler signature[96][97][98]. As a result of the micro-Doppler shift, a time-varying frequency modulation occurs. The micro-Doppler shift is less because of the relatively lower frequency in the through-the-wall radars because the micro-Doppler frequency shift depends on the radar's operating frequency. Since the Fourier transform cannot provide time-dependent frequency information, its use is not suitable for analyzing time-varying frequency features. The commonly used analysis techniques for this purpose are the instantaneous frequency analysis technique[99] [100][101], which is only suitable for mono-component signals and the joint time-frequency analysis technique[102][103][104], which is suitable for both mono-component and multi-component signals. In this part, detailed equations will not be mentioned.

Micro-Doppler signatures depend on the target aspect angle. As a result, the blind spots in certain areas prevent certain parts of the target from being viewed by the radar. The resulting blind spots could prevent the whole micro-Doppler signature. If so, overcoming these target aspect angle dependencies is critical for the proper operation of radar automatic target recognition systems. Since spatially diverse geometry allows data collection over multiple viewing angles in multiple static radars, a radar system with a multi-static configuration can be utilized to prevent clogging. Multi-static configurations are obtained using several separate transmitters and receivers. The multi-static configuration provides the convenience to achieve complementary target information, avoid blind velocities, and to block null or low mono-static radar cross-section (RCS) positions in all channels. Moreover, multi-static radar comprises channels, which are either mono-static or bi-static channels[4]. If the transmitter and receiver nodes are placed together, the channel is mono-static; if the nodes are separated by a considerable distance, the channel is bi-static. Multi-static configuration can be seen in figure 1.12[4].

Human makes periodic movements during walking, breathing, and heartbeat. Thanks

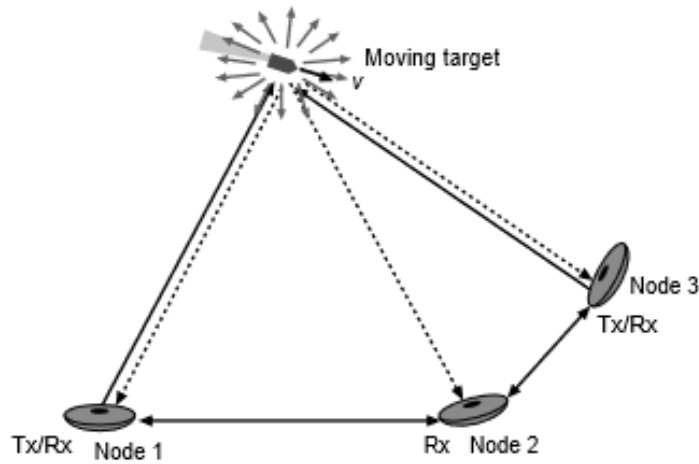


Figure 1.12: Multi-static radar system[4]

to these periodic movements, the micro-Doppler signature of the human occurs and can easily be achieved even if it is behind the wall. The different human motion has a different micro-Doppler signature. The micro-Doppler signature of a walking person is examined in [96][105]. Information about a person's identity, action and intent can be recognized using the micro-Doppler signature. In this way, the actions and activities of the malicious people are prevented by identifying these persons. Moreover, human body movement, heartbeat, breathing, which are biometric features, can be detected for behind-wall systems by the micro-Doppler signature method. However, it will occur in the background clutter during the perception of human motion. Even in the return radar signal, the clutter effect can be seen more. To eliminate the reflected radar signal from the clutter, the different Doppler frequency characteristics of the radar signals reflected from the clutter and reflected from the human are used. Human motions can be achieved by applying a suitable range gating and a notched frequency filtering[4].

1.2.2.3 Doppler Radar for Through-the-Wall in Literature

In 1.2.2.2 and 1.2.2.1, the micro-Doppler signature and Doppler effect which form the basis of Doppler radar were examined. In this part, examples of moving target detection by using Doppler Radar systems for indoor environments will be examined.

TWS systems are used by today's military and civilian organizations for Homeland Security, Law Enforcement and Justice communities. The Air Force Research Laboratory Information Directorate(AFRL/IF), under the sponsorship of the Department of Justice's (DOJ), National Institute of Justice(NIJ) Office of Science and Technology is currently developing advanced Through the Wall Surveillance(TWS) technologies[8]. These technologies are inexpensive, handheld and portable systems. The five prototype devices, which are Enhanced Motion and Ranging Sensor(EMARS) from Raytheon Corporation; Mono-Static Through Wall Sensor from British Aerospace (BAE); Radar Flashlight from Georgia Tech Research Institute (GTRI); Through the Wall Imaging Radar from Akela, Incorporated; and RadarVision from Time Domain Corporation, were developed for detecting moving objects. In this part, just only RADAR Flashlight will be examined because only RADAR Flashlight between five prototype devices uses the Doppler shift principle. Reference [8] can be examined for detailed explanations of other systems. The RADAR Flashlight, developed by Georgia Tech Research Institute (GTRI), will be examined in this part by referenced [8]. RADAR Flashlight is designed to detect objects behind non-metallic walls. Since any body movement creates a sensation, a microwave signal is utilized to detect human body movement. For example, an individual who remains stationary can be detected with a RADAR Flashlight, because the slight motion of the individual's chest during the respiration process produces a large signal return. This signal return can be easily recognized by the unit's display. The RADAR Flashlight's X Band signal will successfully penetrate any non-metallic obstruction that does not pass visible or infrared energy. The RADAR Flashlight works with the principle of Doppler shift. Therefore, a very slight movement will produce a very low-frequency Doppler shifted signal as it is about the breathing of a human body. The return of these and all other motion signals is shown by the operator as a time-varying signal on a bar-graph light-emitting diode display located on the upper surface of the housing of the unit[8]. The number of light-emitting diodes illuminated in the bar graph display is directly proportional to the amount of motion that occurs during the observation period. In contrast, stationary objects in the antenna beam of the unit are ignored because they do not produce a change between the transmitted and received frequency. Bar-graph on RADAR Flashlight can be seen in figure 1.13[8].

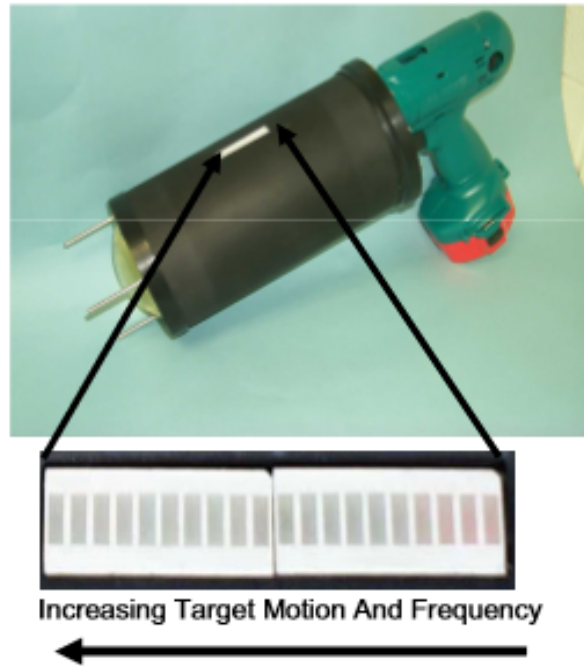


Figure 1.13: Bar-graph on RADAR Flashlight[8]

In [106], micro-doppler signals for indoor environments are analyzed by using linear FM basic decomposition. In this part, the analysis will be briefly mentioned. As mentioned above, periodic movements such as rotation and vibration form a frequency band in addition to the doppler frequency. This phenomenon is called the micro-Doppler signature. Micro-Doppler signals, which are characterized by sinusoidal instantaneous frequency, are similar to baseband sinusoidal frequency modulated signals. Fourier transform, single or Hough transform time-frequency (TF) distributions, Wigner-Hough transform of a signal, other estimation methods based on polynomial phase transformation are insufficient for analysis for various reasons. The linear basis decomposition applied to the Micro-Doppler signals uses the FM basic functions to remove the vibration/rotation frequencies and the phases of the micro-Doppler components in the radar turns. Decomposition may suffer from due to the presence of harmonics with non-orthogonal basic properties. The first harmonic is the most dominant. No prior knowledge of the number of components for decomposition is required, but the maximum instantaneous frequency deviation information of the micro-Doppler signal is required. Detailed analysis and simulation results are provided in reference [106].

In [23], the micro-Doppler signatures of rotational/vibrational targets enduring simple harmonic motions are examined to detect motion in a populated scene and the presence of heavy clutter and classify the type of motion, as described above. As known, the simple harmonic motions such as rotation and vibration induces frequency modulation on received signals by the Doppler radar. For a human, simple harmonic motions can be defined as the movement of the arms when walking. Such different movements of the target constitute different features in the target signature. The instantaneous frequency of the micro-Doppler signature is required for motion detection and identification. In this paper, high-resolution time-frequency techniques, along with a new basis decomposition method and the Hough transform are applied to estimate the instantaneous frequency of the target[23]. Paper can be examined for experimental setup and detailed information about methods.

In addition to the references mentioned above, there are also studies on motion detection behind the wall using doppler radar and micro-doppler signatures in the literature such as [13], [107], [108], [109]. Apart from the use of Doppler radar, there are also studies to detect moving objects behind the wall such as [110], [111], [112], [113], [114], [115], [116], [117].

1.2.3 Wi-Fi RF Capturing Systems

Wi-Fi is the popular name of wireless networking technology and is the information carrier between a transmitter and a receiver. Wi-Fi uses radio waves to provide wireless high-speed network connections and the Internet. Wi-Fi technology has great importance in the development of humanity because people today have Wi-Fi connectivity from their laptops, desktop computers, mobile phones, tablets, and various gadgets. In this way, they can access information from anywhere they want. In addition to accessing information wherever desired, in recent years, Wi-Fi signals are also used to detect objects behind non-metallic obstacles. In this section, a few of these studies using Wi-Fi signals will be mentioned.

In [2], Wi-Vi is introduced as the see-through-wall device that employs Wi-Fi signals in the 2.4 GHz ISM band[2]. Wi-Vi device is utilized to see moving objects behind non-metallic obstacles. Unlike UWB radar systems, Wi-Vi limits itself to

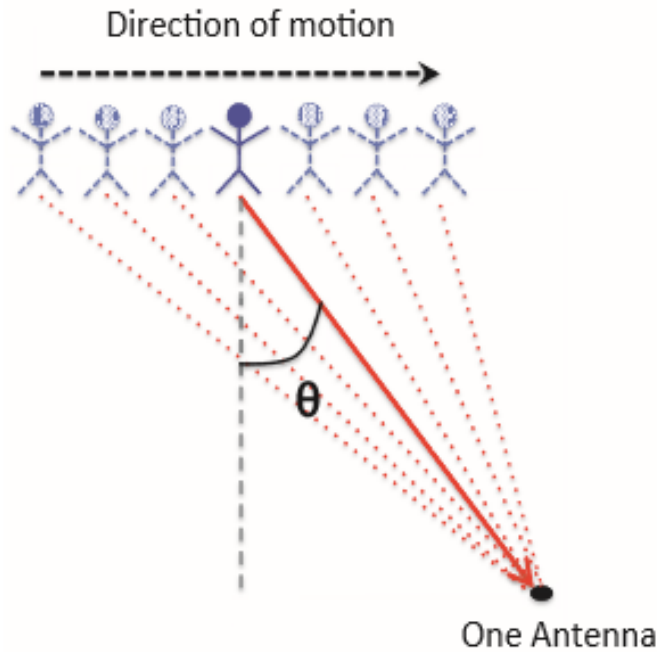


Figure 1.14: ISAR[2]

low-bandwidth such as 20 MHz[2]. In UWB systems, the flash effect can be eliminated by using various systems such as DSAR or using image processing in GHz of bandwidth. So, how does Wi-Vi eliminate the flash effect by using low-bandwidth? MIMO communications are adapted to Wi-Vi. Since, in MIMO, the signal is nulled at a particular receive antenna by using multiple antenna elements, unwanted receiver signal is eliminated by MIMO systems[2]. In a Wi-Vi device, two transmit antennas and a receive antenna is used. Reflections off static objects, including the wall, are nulled in receive antenna. In this way, the flash effect is eliminated. Second, how does Wi-Vi track moving objects without an antenna array? A technique called inverse synthetic aperture radar (ISAR) is utilized to track moving objects. As is known, the Wi-Vi has one receive antenna. Therefore, a single measurement is captured at any point in time. The ISAR technique utilizes the motion of the target to generate an antenna array behavior. By processing such consecutive measurements using standard antenna array beam steering, Wi-Vi can identify the spatial direction of the human. ISAR can be seen in figure 1.14[2]. Here, the discussion about the Wi-Vi device ends. Detailed analysis is provided in reference [2].

Table 1.4: Comparison of Wi-Vi and UWB radar systems

	Wi-Vi	UWB Radar Systems
Resolution	Low resolution	High resolution
Cost	Low-cost	High-cost
Portability	More portable	Less portable
Hand-held property	Have hand-held property	Not have hand-held property
Accessibility to non-military entities	Accessible	Not accessible
Power	Low power	High power
Detectability of targets	Less detectable	More detectable

Apart from Wi-Vi devices, there are several studies in the literature using Wi-Fi signals such as [118][119].

In this section, through-the-wall imaging systems are examined such as UWB radar systems, doppler radar systems, and Wi-Vi. Although some UWB radar systems can detect moving objects, UWB radar systems, such as SAR systems, are generally used to detect stationary objects. In contrast, doppler radar systems and Wi-Vi are generally used to detect moving objects. Here the Wi-Vi and UWB radar systems will be compared in various ways. This comparison can be examined in table 1.4. As mentioned above, Wi-Vi uses the ISAR technique to describe motion. However, various deficiencies may arise in the use of this technique. If the amount of motion of the object whose movement is defined is low, TWI resolution is less. This problem does not occur in UWB radar systems so detectability of target is more. Also, UWB systems are more expensive, less portable than Wi-Vi and do not have hand-held property because they use large transmitters and receivers in size. Also, UWB radar systems are generally used by military entities, while Wi-Vi can be used by non-military entities. Moreover, Wi-Vi uses less power than UWB radar systems.

1.3 Outline of Thesis

Thesis outline can be expressed as follows:

In Chapter 2, background information will be given. Background information in-

cludes ground penetrating radar, reflection and propagation theory of electromagnetic signals, current through the wall target detection and identification methods.

In Chapter 3, methods used in this thesis will be described in detail. Methods used in this thesis include mean based flash effect removal for flash effect removal, entropy-based segmentation for image segmentation, k-means clustering for image segmentation, the textural feature-based method for feature extraction, histogram of oriented gradients for feature extraction, support vector machine for classification for classification.

In Chapter 4, results and discussions will be given.

Conclusion will be given in Chapter 5.

CHAPTER 2

BACKGROUND

2.1 Ground Penetrating Radar

GPR is a geophysical method used for forming an image of subsurfaces, including rock, soil, ice fresh water, pavements, structures, and landmine etc.[26]. In introduction part, TWI systems in the literature are discussed. In this thesis, the ground penetrating radar(GPR) system will be used to obtain the image of the stationary object behind the wall. This is generally beyond the intended use of GPR. However, in this thesis, GPR will be theoretically used as same as it is used in landmine detection, etc. In GPR systems, depending on the application, it uses radio waves in the frequency range of 300 MHz to 4GHz. These applications can be seen in references [120], [121], [122]. During GPR studies, there is a trade-off between penetration depth and resolution in the selection of the center frequency of GPR signals. As is known, low center frequency signals can penetrate deeper into the wall while low center frequency signals form a low resolution image. In contrast, high center frequency signals can generate high-resolution images while high center frequency signals penetrate less deeply into the wall[9]. In this study, the operating frequency used to create the image of humans and other objects behind the wall is chosen as 1.5 GHz. At 1.5 GHz operating frequency, it has been seen that the resulting image provides the required high resolution and penetration depth.

There are two types commonly used in GPR systems, which are time-domain radar and frequency-domain radar. In time-domain type GPR, the transmitter sends a short-duration pulse, while in frequency-domain type GPR the transmitter sends a continuous wave. For time-domain GPR, the reflected signal is received as a function of time

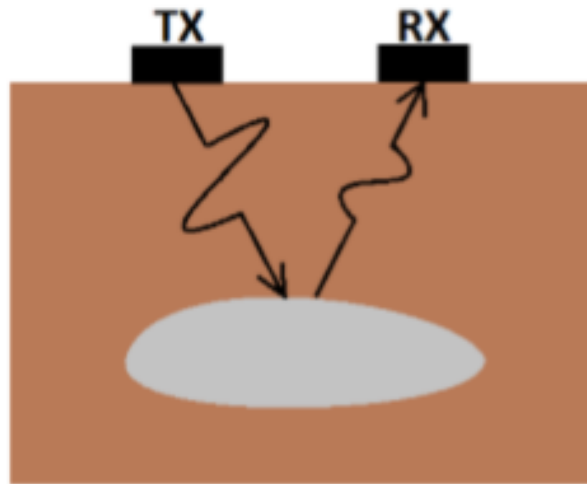


Figure 2.1: Basic working principle of GPR[9]

and the image is obtained by looking at the change in the energy of the reflected signal. Time-of-flight principle can be used for calculating the target position[122][123]. In this thesis, time-domain GPR signals will be used for through-the-wall imaging. For continuous wave GPR, the reflected signal is received simultaneously. It is impossible to detect the position of the target using these signals because no change in the signal is observed. The modulation technique is applied in the frequency domain to make detection possible[9]. Also, frequency-domain GPR signals suffer from interference and flash effect. Various techniques are used to solve these problems. These techniques will not be discussed here. To examine these techniques in detail, references [122][123][124] can be reviewed.

As mentioned above, GPR will be used for through-the-wall imaging in this study. However, it is necessary to explain the basic working principle of GPR, which is widely used in subsurface surveys, and what GPR is generally. The basic working principle of GPR for subsurface surveys can be seen in figure 2.1[9]. As shown in 2.1, Basic GPR consists of a transmitter and a receiver, which are moved above the surface to form a subsurface image. This movement of the transmitter and receiver creates a line array of transmitting antennas and receiving antennas. The distance between two adjacent antennas is a few cms.

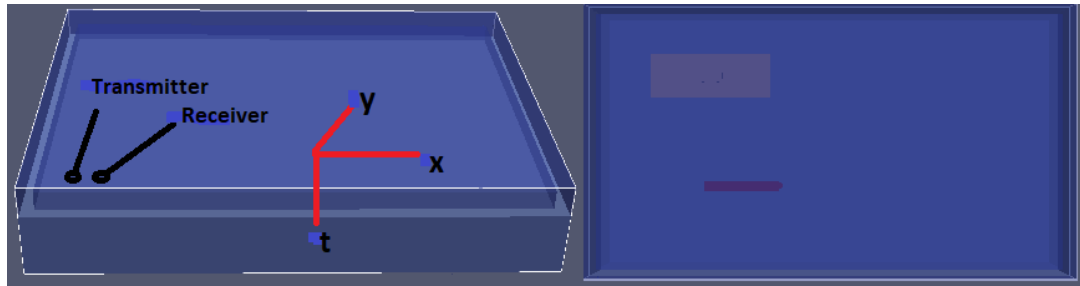


Figure 2.2: a) Location of the receiver and transmitter above the room b) Location of objects in the room

Using the same basic principle, GPR will create images of objects behind the wall in this study. As shown in figure 2.2, a receiver, and a transmitter antenna will be used in this study. These antennas move in the y-direction such that the distance between the transmitter and the receiver is constant, forming the line array transmitter and receiver system. At each position of the antennas, taking into account the change in the energy of the signals obtained by the receiver, images of objects behind the wall are obtained. Here, the distance between the two adjacent antennas is a few cms. That is, the antennas are moved a few cms in the y-direction. Moreover, the distance between a transmitter and a receiver and the amount of movement of the antennas is an important factor for resolution.

The representations of GPR data will be explained in the next subsections. These representations are called A-scan, B-scan, and C-scan, and are one, two, and two-dimensional dataset, respectively.

2.1.1 A-Scan

The single radar trace of the transmitter and receiver at a fixed position is called A-scan, which is a function of t . A-Scan can be shown as $A(x_i, y_i, t)$. x_i and y_i represents, respectively, the location of the transmitter and receiver at a fixed point. In A-scan, the distance of the target to the transmitter and receiver is related to t . In GPR's subsurface surveys, the highest reflection occurs in the air-ground interface, which is called ground bounce. When using GPR for TWI, the highest reflection occurs between the air and front wall and this is called flash effect[2]. Also, the

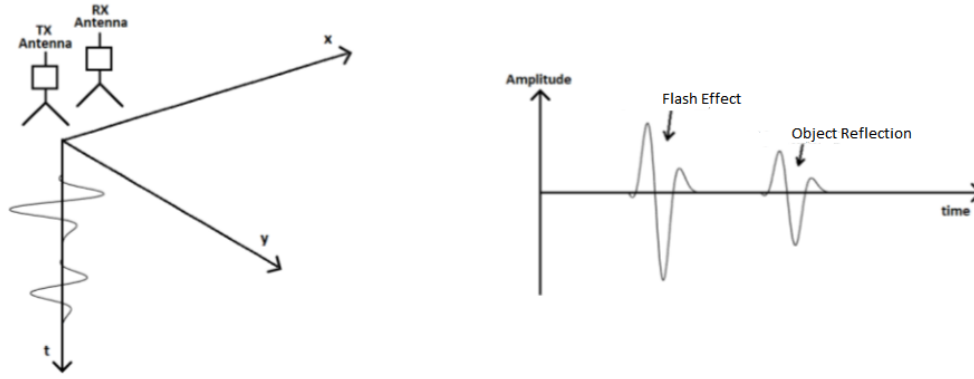


Figure 2.3: A-Scan representation[9]

reflections from the side walls are also very high in this study. As shown in figure 2.3, the flash effect is so high in this study that the reflections of the target are not visible in the A-scan. The image processing algorithms required to remove the flash effect will be discussed in the following sections.

2.1.2 B-Scan

In this study, GPR antennas move along the y-axis and take measurements at each position of antennas as shown in 2.4. As a result of these measurements, the A-scans measured at each position of the GPR antennas are combined to form a B-scan, which is a two-dimensional dataset. B-Scan can be shown as $B(x_j, y, t)$. Here, GPR antennas are fixed on the x-axis and moves along the y-axis. As known, the distance of the target to the GPR antennas is related to t. As shown in figure 2.5, the flash effect is so high in this study that the reflections of the target are not visible in the B-scan. The image processing algorithms required to remove the flash effect will be discussed in the following sections.

2.1.3 C-Scan

In this study, if the GPR antennas move in the x-y plane as shown in 2.6, a three-dimensional $C(x, y, t)$ dataset is obtained[9]. In other words, the B-scans measured

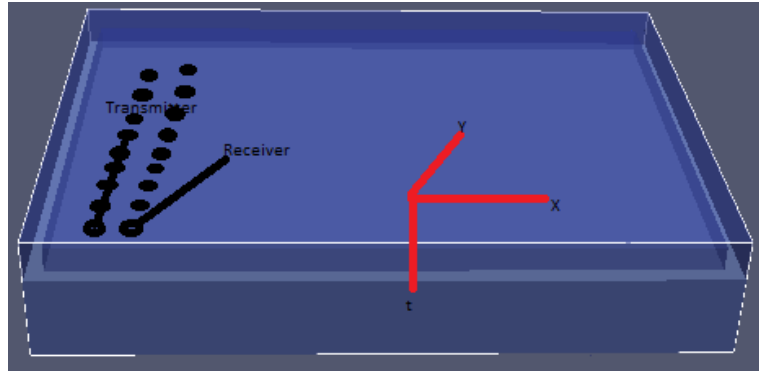


Figure 2.4: Location of GPR antennas to obtain B-Scan

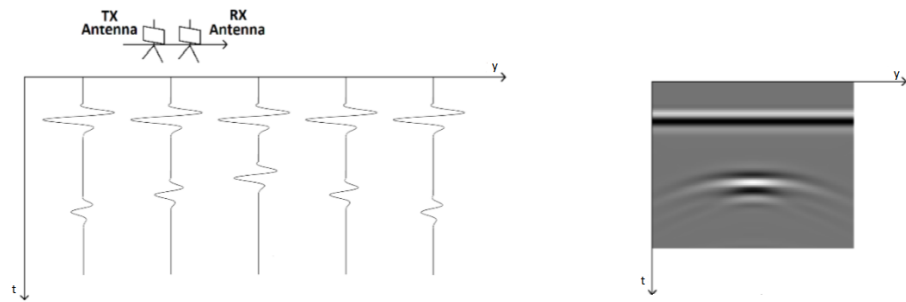


Figure 2.5: B-Scan representation[9]

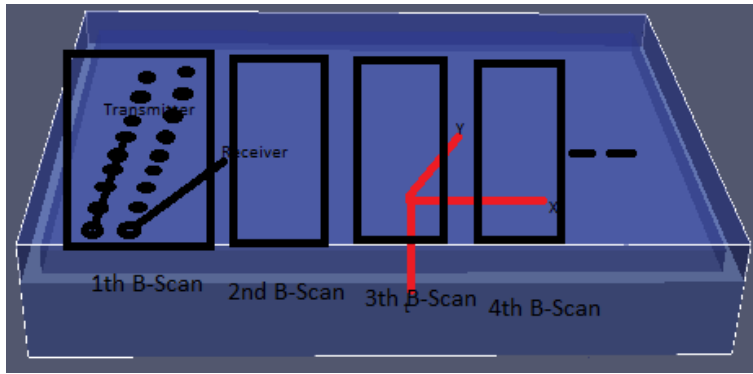


Figure 2.6: Location of GPR antennas to form C-Scan

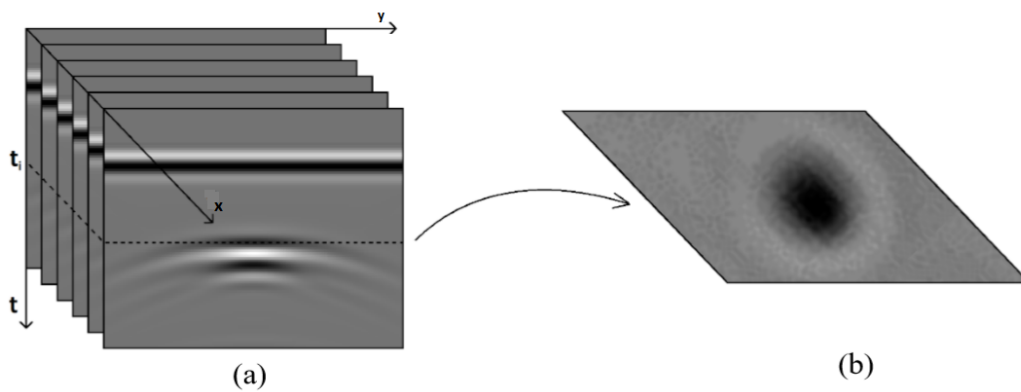


Figure 2.7: a) Three-Dimensional GPR data b) A horizontal slice for obtaining C-Scan[9]

at each position of line array are combined to form a $C(x, y, t)$. The horizontal slice at a certain depth obtained from the three-dimensional data is called C-scan as shown in 2.7.

As shown in figure 2.7, the flash effect is so high that the reflections of the target are not visible in the C-scan. The image processing algorithms required to remove the flash effect will be discussed in the following sections.

After obtaining the GPR data, image processing algorithms are applied to the A-Scan, B-Scan and C-Scan data to detect the human target behind the wall.

2.2 Reflection and Propagation Theory of Electromagnetic Signals

As is known, in this study, TWI will be created by using GPR. With the classification of features extracted by applying various image processing steps, it will be determined whether the object behind the wall is human or not. Of course, before applying these classification and image processing steps, images will be obtained by using physics-based approaches. The physics-based approaches used in this study will theoretically be explained in this section. Respectively, in subsection 2.2.1, 2.2.2, and 2.2.3, reflection, and transmission of electromagnetic signal at the interface between two different dielectrics, attenuation of the electromagnetic signal propagating through a medium, and velocity of the electromagnetic signal propagating through a medium will be mentioned.

2.2.1 Reflection and Transmission of Electromagnetic Signal at the Interface between Two Different Dielectrics

As is known, there is intrinsic impedance in any medium where electromagnetic wave propagates. Intrinsic impedance is represented as η . The intrinsic impedance varies depending on general medium permittivity, permeability, and conductivity. The intrinsic impedance can be calculated as shown in equation 2.1[125][126][127].

$$\eta = \sqrt{\frac{j\omega\mu}{\sigma + j\omega\epsilon}} = \sqrt{\frac{\mu}{\epsilon}} \left(1 - j\frac{\sigma}{\omega\epsilon}\right)^{-\frac{1}{2}} \quad (2.1)$$

In equatin 2.1, ϵ , μ , σ , and ω represents, respectively, permittivity, permeability, conductivity, and angular frequency. At given frequency, permittivity and permeability are given by $\epsilon = \epsilon_r\epsilon_0$, and $\mu = \mu_r\mu_0$. ϵ_r , μ_r , ϵ_0 and μ_0 represents, respectively, relative permittivity, relative permeability, permittivity of free space and permeability of free space.

Assume that, in this study, low-loss condition is provided such as $\frac{\sigma}{\omega\epsilon} \ll 1$. For

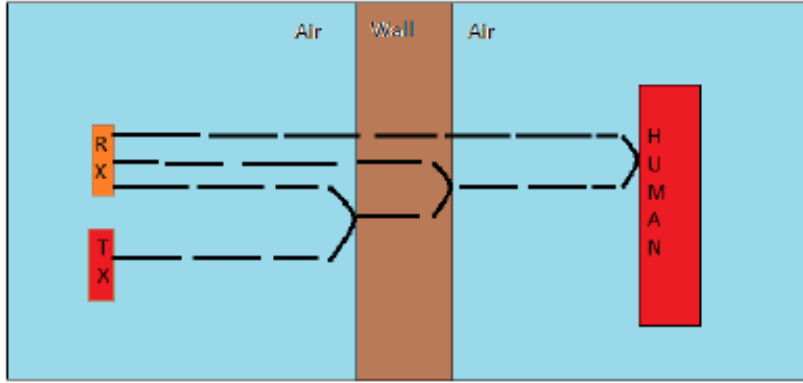


Figure 2.8: Reflection and transmission at the air-wall boundary

low-loss condition, equation 2.1 becomes

$$\eta \approx \sqrt{\frac{\mu}{\epsilon}} \left(1 + j \frac{\sigma}{2\omega\epsilon} \right) \quad (2.2)$$

where $Re(\eta) = \sqrt{\frac{\mu}{\epsilon}}$ and $Im(\eta) = \frac{\sigma}{2\omega\epsilon} \sqrt{\frac{\mu}{\epsilon}}$.

As the electromagnetic wave passes between two different media with different intrinsic impedances, it reflects some of its energy and continues the remaining energy path. Reflection and transmission coefficients can be calculated based on intrinsic impedance as shown in equation 2.3[125].

$$\Gamma = \frac{E_r}{E_i} = \frac{\eta_2 - \eta_1}{\eta_2 + \eta_1} \quad \text{and} \quad \tau = \frac{E_t}{E_i} = \frac{2\eta_2}{\eta_2 + \eta_1} \quad (2.3)$$

The reflection coefficient and transmission coefficient are represented, respectively, as Γ and τ . Moreover, η_1 and η_2 are relative intrinsic impedance values of the mediums[9]. E_i , E_r , and E_t represent, respectively, the amplitude of the incident wave, the reflected wave, and the transmitted wave. In the structure is seen figure 2.8, the amplitude of the electromagnetic wave transmitted and reflected from each region can be calculated by using equations given above.

2.2.2 Attenuation of Electromagnetic Signal Propagating Through a Medium

In this section, the propagation loss and attenuation of the electromagnetic wave propagated in the lossy medium will be mentioned. Assume that electromagnetic wave propagates through z-direction. The electromagnetic wave is represented as shown in equation 2.4.

$$E(z) = E_z = E_0 e^{-\gamma z} \quad (2.4)$$

As seen in equation 2.4, the amplitude and phase of the signal vary with the medium's propagation constant. E_0 is the complex amplitude, γ is propagation constant. As known, propagation constant is a complex quantity. Propagation constant can be calculated as shown in equation 2.5.

$$\gamma = \alpha + j\beta \quad (2.5)$$

where α is called the attenuation constant and β is called the phase constant[125]. As is known, attenuation constant and phase constant were calculated in detail in the introduction chapter 1. Here, in low-loss condition, attenuation and phase constant are calculated as shown in equation 2.6.

$$\alpha = \text{Re}(\gamma) \approx \frac{\sigma}{2} \sqrt{\frac{\mu}{\epsilon}} \quad (\text{Np/m}) \quad \text{and} \quad \beta = \text{Im}(\gamma) \approx \omega \sqrt{\mu\epsilon} \quad (\text{rad/m}) \quad (2.6)$$

Depending on the attenuation constant, the amplitude of the propagating electromagnetic wave changes. The absolute value of the electromagnetic wave can be seen in equation 2.7.

$$|E_z| = |E_0| e^{-\alpha z} \quad (2.7)$$

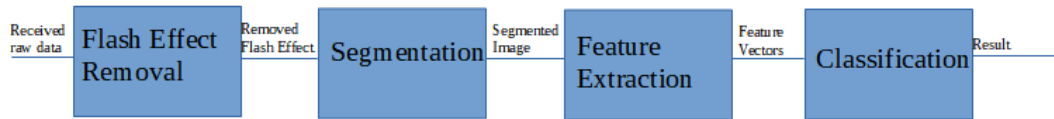


Figure 2.9: Block diagram of received raw data processing

2.2.3 Velocity of Electromagnetic Signal Through a Medium

The propagation velocity of the electromagnetic signal in the medium can be seen in equation 2.8[125][9].

$$v = \frac{1}{\sqrt{\mu\epsilon}} = \frac{c}{\sqrt{\mu_r\epsilon_r}} \quad (2.8)$$

where v is the velocity of an electromagnetic signal in medium, c is the speed of light in free space, ϵ is the permittivity of the medium, and μ is the permeability of the medium.

2.3 Current Through the Wall Target Detection and Identification Methods

As described above, the image of the target behind the wall is obtained using the GPR. However, this image is the raw image. For target detection to be performed, the received raw image must be processed. The block diagram of the processing of the received raw data for target detection can be seen in figure 2.9.

The main steps of through the wall target detection process are written below:

- Flash Effect Removal
- Segmentation
- Feature Extraction
- Classification

2.3.1 Flash Effect Removal

As known, when using GPR for TWI, the highest reflection occurs between the air and front wall and this is called flash effect[2]. This can be seen very clearly in figure 2.3. As shown in figure 2.3, the flash effect is so high that the reflections of the target are not visible in the A-scan. In through-the-wall target detection studies, false alarms generally occur when the flash effect is not removed. Therefore, flash effect removal methods must be used in studies through the wall target detection and identification. In general, as described in the introduction part, measures are taken in image-forming radar or sensor systems to eliminate the flash effect. However, in this thesis, the flash effect will be eliminated in the image processing step.

Flash effect and ground bounce have very similar features. Hence, ground bounce removal techniques can be used to remove the flash effect in this study. In the literature, there are many methods for ground-bounce removal[9]. These methods can be applied to A-scan or B-scan data. One of them is "Simple average operation", which detects the location of flash effect as the mid-point of the maximum and minimum of an A-Scan[128][129]. Also, "PCA and ICA based approach" is utilized for flash effect and clutter reduction[130]. Moreover, another method is "Mean based flash effect removal". In "Mean based flash effect removal method", the flash effect is estimated to be the mean of all the traces of the signal matrix[131][132].Furthermore, another method is "Median based flash effect removal". In "Median based flash effect removal method", the flash effect is estimated as the median of all surrounding traces[131][132].Also, specific filtering operations such as moving median and Wiener filtering can be used for removing the flash effect. Before and after the flash effect is removed, examples of B-Scan and A-Scan can be seen, respectively, in figures 2.10 and 2.11.

It also generates false alarms during target detections due to reflections of sidewalls, except for the front wall flash effect. These reflections resulting from the side walls are eliminated by trimming edges of B-Scan images in the y-direction during image processing. To remove the front wall flash effect, this clipping must be performed before the ground bounce removal method is applied. Raw b-scan data, clipped b-scan data, and flash effect removal applied b-scan data can be seen in figure 2.12.

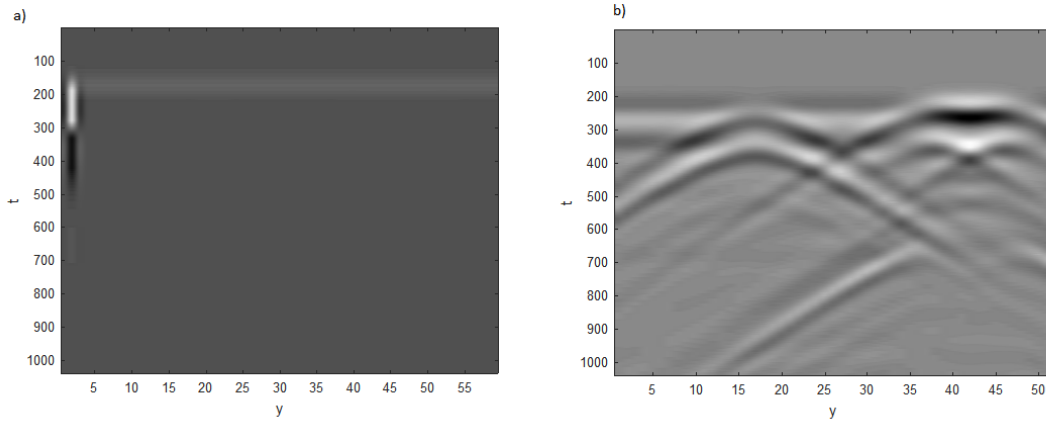


Figure 2.10: a) Received B-Scan raw data b) B-Scan data which flash effect is eliminated

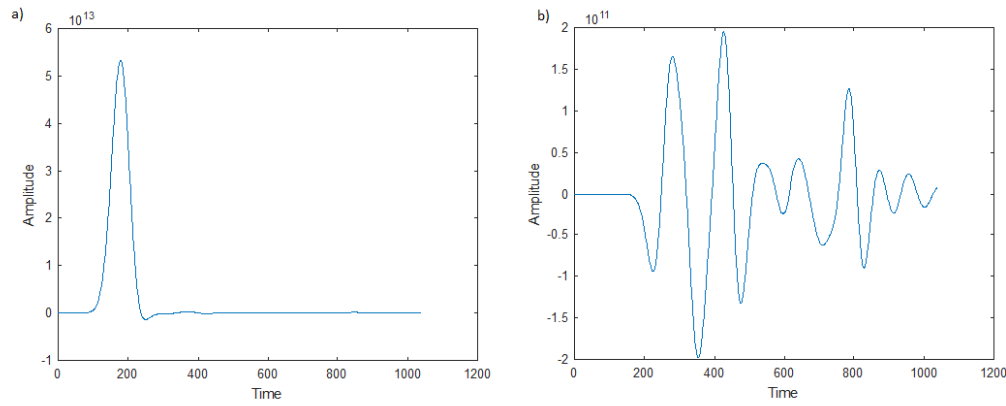


Figure 2.11: a) Received A-Scan raw data b) A-Scan data which flash effect is eliminated

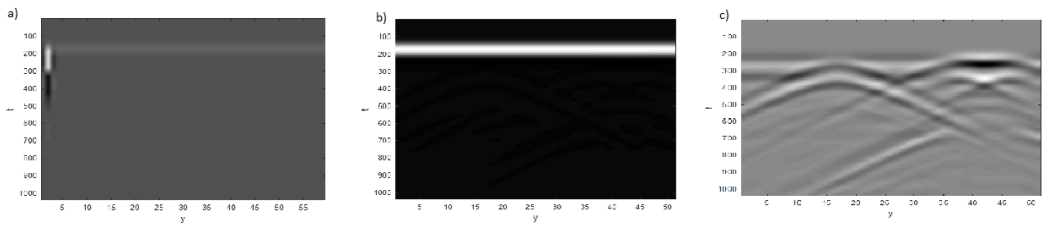


Figure 2.12: a) Raw B-Scan data b) Trimming B-Scan data c) B-Scan data which flash effect is eliminated

2.3.2 Segmentation

In computer vision, classification and pattern recognition, image segmentation is the process of separating an image into meaningful multiple segments. In general, the purpose of segmentation is facilitating the analysis of an image, representing meaningful areas of the image, decomposing the image into parts for further analysis, improving the image quality for subsequent analysis and scene description, being the pre-processing step of target detection, and classification, etc. As in many studies, image segmentation algorithms are used through the wall target detection and identification. There are two main reasons why image segmentation is used in this study. The original image generally contains clutters and noise due to wall, multiple reflections and antenna cross talk[133]. The image segmentation method helps to remove these clutter and noise. The image segmentation technique enhances the images by suppressing clutter regions, which were distinct from target regions[92]. Secondly, the image segmentation step is utilized as the pre-processing of feature extraction and classification steps. Before starting feature extraction, candidate target regions only are obtained. It is ensured that no more processing is performed and the feature vectors of the two different targets do not affect each other. The binary image produced by the image segmentation method masks the original input image to produce an enhanced image with candidate target regions only[92]. One of the important points in image segmentation is that the applied method must not cause data loss.

There are many studies on image segmentation in the literature[134][135][136]. The general headings of segmentation methods are as follows: Thresholding, clustering, edge detection, interest point detection, and region growing. It is not possible to mention all of these segmentation methods in here. Some of the methods used in through the wall imaging segmentation will be discussed here. One of them is "Between-Class variance thresholding". The BCV thresholding method segments an image into two near-uniform regions by maximizing the sum of class variances[133][137][138][92]. The BCV method does this by setting the threshold value. Another method is "Entropy-Based segmentation". "Entropy-Based segmentation" maximizes sum of class entropies by setting the threshold value[133][137][138][92]. Moreover, blob detection can be used for image segmentation step. Blob detec-

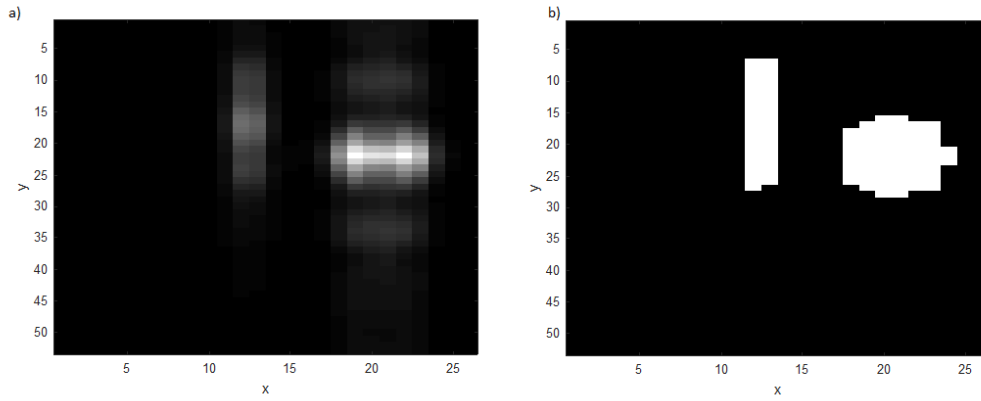


Figure 2.13: a) The received raw data b) The binary mask created with the segmentation step of the received raw data

tion is an interest point detection method. Blob detection methods are used to detect the regions of the digital image that differ in brightness. The laplacian of gaussian and the difference of gaussian approaches are the leading methods of blob detection. Also, although the Gaussian mixture model is generally a classification algorithm[139], it can be used as an image segmentation method in this study. Moreover, although the K-means clustering method is an unsupervised algorithm, it can be used in the image segmentation step in this study[133][137]. The binary mask created with the segmentation step of the image data is shown in figure 2.13. The image is seen in figure 2.13 is the energy sum of the top view of the 3-D data created by combining the B-Scan data.

2.3.3 Feature Extraction

In the previous step, clutter and noise are tried to eliminate using image segmentation algorithms. Image segmentation techniques enhance the images. Also, the targets are segmented alone. In this way, the calculation amount is reduced and the processing of a specific target is allowed. As mentioned above, the image segmentation step is the pre-processing step of the feature extraction step. Feature extraction involves reducing the number of resources required to describe a large set of data. In machine learning, pattern recognition and classification, the data available to the designer is too large to be processed in most cases and many cases may not make sense to the

machine. Because of this, it can be transformed into feature vectors. Feature selection is an important issue when creating a feature vector. The selected features must contain relevant information from the input data. These features are used for classification.

There are several methods in the literature for feature extraction. The textural feature-based extraction method is one of them. Textural features contain information about the spatial arrangement of pixel intensities in an image or a selected region of the image[92]. Commonly used textural features are energy, entropy, contrast, homogeneity, correlation, shade, and prominence. Contrast measures are related to the amount of local intensity change in the image[92]. The correlation feature is a measure of gray level linear dependencies in the image[92]. The energy feature measures the textural uniformity[92]. There are several methods proposed in the literature to capture textural features from an image, such as gray-level co-occurrence matrix(GLCM), gray-level run-length matrix(GLRLM), fractals, Gabor filters, and the wavelet transform [140] [141] [142] [143] [144] [145].The co-occurrence matrix is a two-dimensional histogram of gray-levels created by looking at the specific spatial direction and distance[92]. The gray-level run-length matrix gives the size of homogeneous runs for each grey level. Another method used for texture analysis is the Gabor filter. The Gabor filter is a linear filter that analyzes the presence of certain frequency content in the image in certain directions around the point of analysis. Moreover, the wavelet transform is similar to the Fourier transform with a completely different merit function. The main difference is this: Fourier transform decomposes the signal into sines and cosines, i.e. the functions localized in Fourier space; on contrary, the wavelet transform uses functions that are localized in both the real and Fourier space.

Apart from textural features based extraction, various feature extraction methods are available in the literature. Some of these methods are statistical feature extraction and geometrical feature extraction[146]. Weibull model can be used for statistical feature extraction. Although statistical feature extraction provides important information about a target, it shows limited performance because it neglects features like shape, extent in range, crossrange and height. However, such features are not neglected in geometrical feature extraction[146]. Another feature extraction method is

the hough transform. The purpose of the Hough transform technique is to detect imperfect instances of lines, curves, and objects in an image by a voting procedure. This voting procedure is performed in a parameter space in which the object candidates are obtained as local maxima[147][148][1]. However, a lot of work is being done to improve the hough transform because it requires a lot of storage and computation. Also, another feature extraction method is the Histogram of Oriented Gradients(HoG). In the literature, HoG feature extraction has been used in many studies such as human detection[149][150], underground surveys with GPR[9], pedestrian detection[151], facial expression recognition[152] etc. As a result of the studies[149] conducted by Navneet Dalal and Bill Triggs in 2005, HoG usage became widespread. As a result of literature research, through the wall imaging and detection studies, using HoG feature extraction has not been encountered. However, since the histogram of oriented gradients(HoG) is a feature descriptor used in the purpose of object detection for computer vision, machine learning, pattern recognition, and image processing, etc., in this thesis, the histogram of oriented gradients can be used for feature extraction. Histogram of oriented gradients technique counts the occurrence of gradient orientation in local portions of the image. The basic idea behind the histogram of oriented gradients descriptor is that the appearance and shape of the local object in an image can be defined by the distribution of density gradients or edge directions. The HoG descriptor has several important advantages over other descriptors. Since it works in local cells, it does not change against geometric and photometric transformations except object orientation. Such changes will only appear in larger spatial regions. The HoG identifier is therefore particularly suitable for human detection in images. The histogram of oriented gradients feature extraction is discussed in more detail in chapter 3.

Also, feature extraction techniques used in underground surveys with GPR can be tried in through the wall imaging and detection. Reference [9] should be checked for this. In [9], symmetry feature, the hyperbolic shape, Markov Models, time-frequency domain signature analysis, edge histogram descriptors(EHD), the spectral characteristics, etc. are recommended.

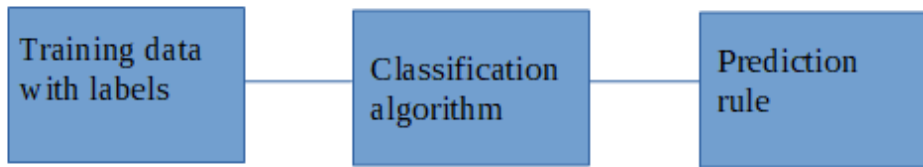


Figure 2.14: Training phase of supervised learning algorithms

2.3.4 Classification

After the feature extraction step, classification is the next-step in through-the-wall target detection and identification. To describe classification, it is necessary to define what the learning algorithm(machine learning) is. Machine learning (ML) is the scientific study of algorithms and statistical models. These algorithms and statistical models allow computer systems to perform a specific task using pattern and inferences rather than explicit instructions. Machine learning mainly has two types of learning algorithms, which are unsupervised learning and supervised learning. Unsupervised learning algorithms take a data set that contains only inputs without their labels. Unsupervised learning algorithms learn prediction rules from these input data[9]. On the other hand, in supervised learning, prediction rule is obtained by using classification or regression algorithms with the help of the training dataset and their labels. This study will focus on classification algorithms, a type of supervised learning. In this study, there are two stages, the training phase, and the test phase, to detect targets. The training phase is the stage of obtaining the prediction rule mentioned above. The block diagram of the training phase can be seen in figure 2.14. Once the prediction rule is obtained, it is determined by using prediction rule during the test phase whether the test data is the target or not[9].

There are several classification algorithms in the literature for this subject. In [153], [154], support vector machine(SVM) is utilized for through-the-wall imaging classification. The purpose of SVM is to construct optimal hyperplane as a decision boundary such that the margin of separation between the two classes in the data is maximized[155]. Support vectors are defined as samples that are used as support for the optimal location of the decision boundary[155]. If any two-classes are lin-

early separable, for a given $(x_1, y_1), \dots, (x_n, y_n)$ where y_i indicate the labeled class to which feature vectors x_i belong, any linear hyperplane can be written as equation 2.9.

$$y = w^T x + b \quad (2.9)$$

where w is the normal vector to the hyperplane and b is bias. If two classes cannot be separated linearly, various kernel functions are used to provide nonlinear separation [156][157][158].

Another classification method used for through-the-wall imaging classification in [159] is Naive Bayes Classifiers, which are a family of simple "probabilistic classifiers" based on applying Bayes' theorem. First of all, according to training data, the probability of each class and the conditional probability of each class given each input data are calculated. Then, the operation of the algorithm calculates the probability of each case for an element and classifies it according to the highest probability value by using Bayes' theorem[160][161].

Another method used for through-the-wall imaging classification in [162] is k-Nearest Neighbors, which are simple classifiers that select the training samples with the closest distance to the query sample[163]. The steps of the K-nearest neighbor algorithm are listed below.

- Determine parameter K =number of nearest
- Calculate the distance between the query-instance and all the training samples
- Sort the distance and determine nearest neighbors based on the K -th minimum distance
- Gather the category of the nearest neighbors
- Use simple majority of the category of nearest neighbors as the prediction value of the query instance

Euclidean distance between i^{th} sample vector and j^{th} sample vector can be calculated

as shown in equation 2.10.

$$d(x_i, x_j) = \sqrt{(x_{i,1} - x_{j,1})^2 + \dots + (x_{i,m} - x_{j,m})^2} \quad (2.10)$$

where d is euclidean distance, x_i and x_j are sample feature vectors, which have m features[164][165].

Apart from the algorithms described above, random forests[166], the mahalanobis distance metric[92], learning vector quantization[167] and hidden markov model[168] can be used as classification algorithm.

CHAPTER 3

METHODS USED IN THIS THESIS

In this chapter, the methods to be used in this thesis will be described in detail. These methods are also available in the literature and are briefly mentioned in previous chapter. In section 3.1, mean based flash effect removal is used for flash effect removal. In section 3.2, 3.3, 3.4, respectively, between-class variance thresholding, entropy-based segmentation and k-means clustering can be used for image segmentation. In section 3.5, and 3.6, respectively, textural feature based method, and HoG can be used for feature extraction. In section 3.7, support vector machine can be used for classification.

3.1 Mean Based Flash Effect Removal for Flash Effect Removal

As shown in figure 3.1, which is a B-Scan data, the flash effect from the sidewall and front wall does not allow the display of targets by dominating the image. These flash effects must be eliminated to avoid false alarms and to detect the target. Two different algorithms are required to remove the flash effects on the sidewall and front wall.

In the literature search to eliminate the flash effect caused by the sidewall, no solution could be found. As a result of my work, the flash effect resulting from the sidewall was eliminated by trimming the b-scan image along the y-axis as shown in figure 3.2. However, in this part of my thesis, there is a point that I feel incomplete because this is not a valid algorithm for real-time studies. Therefore, a better literature search should be made and this algorithm should be developed.

After eliminating the side wall flash, the next step is to eliminate the front wall flash.

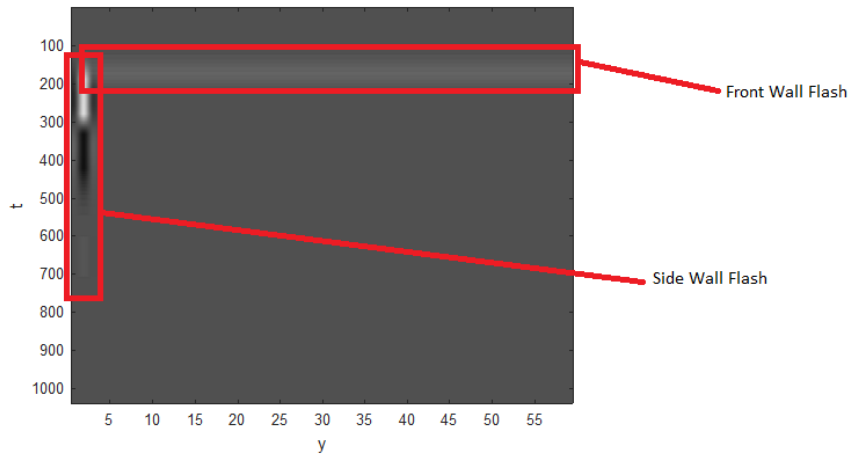


Figure 3.1: Representation of flash effects

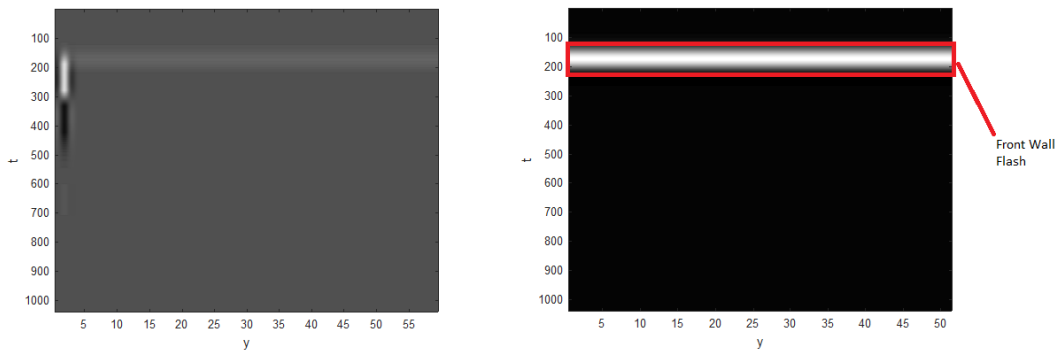


Figure 3.2: Representaion of eliminating of side wall flash

The methods available in the literature, which are simple average operation, PCA and ICA based approach, mean based flash effect removal and median based flash effect removal, are mentioned in previous chapter. Because of the sufficient results and simple application, mean based flash effect removal method are preferred for flash effect removal.

In mean based flash effect removal method, the front wall flash effect is estimated to be the mean of all the traces of the B-Scan signal matrix[131]. In this case, the front wall flash effect is assumed to be constant for each trace. The front wall flash effect for the mean based algorithm can be calculated as shown in equation 3.1 for B-Scan image[131].

$$g = \frac{1}{K} \sum_{i=1}^K (s_{i,j}) \quad (3.1)$$

where K represents the number of A-Scan trace, s represents B-Scan data, which is two dimensional, g represents constant front wall flash effect, which is a vector. If g, which is a constant front wall flash effect, is subtracted from each A-Scan trace contained in the B-Scan data, the front wall flash effect is eliminated. This situation can be formulated as seen in equation 3.2.

$$r_{i,j} = s_{i,j} - g|_{i=1,2,\dots,K} \quad (3.2)$$

where r represents B-Scan data which front wall flash is eliminated. A-Scan and B-Scan data which front wall flash is eliminated, respectively, can be seen in figures 2.11 and 2.10.

3.2 Between-Class Variance Thresholding for Image Segmentation

After applying the flash effect removal algorithm to Raw B-Scan data, the image segmentation stage is started as mentioned in the previous chapter. Between-Class Variance Thresholding method is one of the image segmentation algorithms used in this thesis. Another name for BCV is 'Otsu Method' because it was found by

Nobuyuki Otsu. Between-Class Variance Thresholding method separates the image into two regions by determining the optimal threshold value[169]. The purpose of this method is to choose an optimal threshold value which maximizes the sum of class variances[169]. Since this method is applied to the grayscale image, it is necessary to make the data available to grayscale.

Assume that X is a grayscale image that has a L intensity level. Optimal threshold value for BCV method can be calculated as seen from equation 3.3[92][133].

$$f_{BCV} = \operatorname{argmax}_T (p_1(T)[v_1(T) - v_l(T)]^2 + p_2(T)[v_2(T) - v_l(T)]^2) \quad (3.3)$$

where p_1 and p_2 represent respective region probabilities, v_1 and v_2 represent the means of the respective regions, T is optimal threshold value and v_l is the mean image intensity. The means of the respective regions are given by

$$v_1(T) = \sum_{i=0}^T \left(\frac{i \cdot p_i}{p_1(T)} \right) \quad (3.4)$$

$$v_2(T) = \sum_{i=T+1}^{L-1} \left(\frac{i \cdot p_i}{p_2(T)} \right) \quad (3.5)$$

where p_i is a discrete probability mass function. Discrete probability mass function is given by

$$p_i = \frac{f_i}{N} \quad (3.6)$$

where f_i is the value of any intensity level in histogram and N is the total number of pixel values. The respective probabilities can be expressed as

$$p_1(T) = \sum_{i=0}^T p_i \quad (3.7)$$

$$p_2(T) = \sum_{i=T+1}^{L-1} p_i \quad (3.8)$$

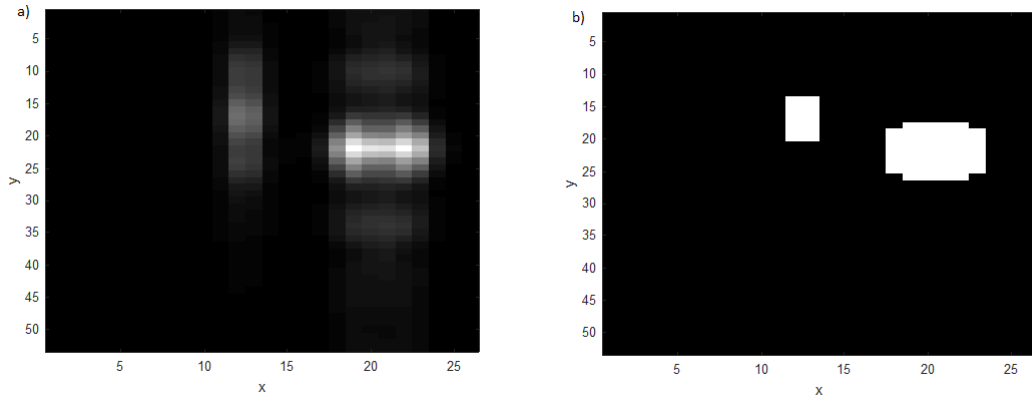


Figure 3.3: a) The image of the energy sum of the top view of the 3-D data created by combining the B-Scan data b) Binary image

After calculating the optimal threshold value according to the above equations, the binary image of the energy sum of the top view of the 3-D data created by combining the B-Scan data is obtained by using the threshold value as seen in figure 3.3. In this image, pixels above the threshold value are assigned to 1, and pixels below the threshold value are assigned to 0. Then, the obtained binary image masks the image of the energy sum of the top view of the 3-D data created by combining the B-Scan data, the image of C-Scan data at a depth of 300, the image of C-Scan data at a depth of 325, and the image of C-Scan data at a depth of 350. Feature vectors are extracted from these 4 masked images. The output of these mask processings can be seen in figure 3.4.

3.3 Entropy-Based Segmentation for Image Segmentation

Another image segmentation method used in this thesis is entropy-based segmentation. The entropy-based segmentation method separates the image into two regions by determining the optimal threshold value[169]. The purpose of this method is to choose an optimal threshold value that maximizes the sum of class entropies instead of maximizing the sum of class variances[169]. Since this method is applied to the grayscale image, the input image must be converted to a grayscale image.

Assume that X is a grayscale image that has a L intensity level. The optimal thresh-

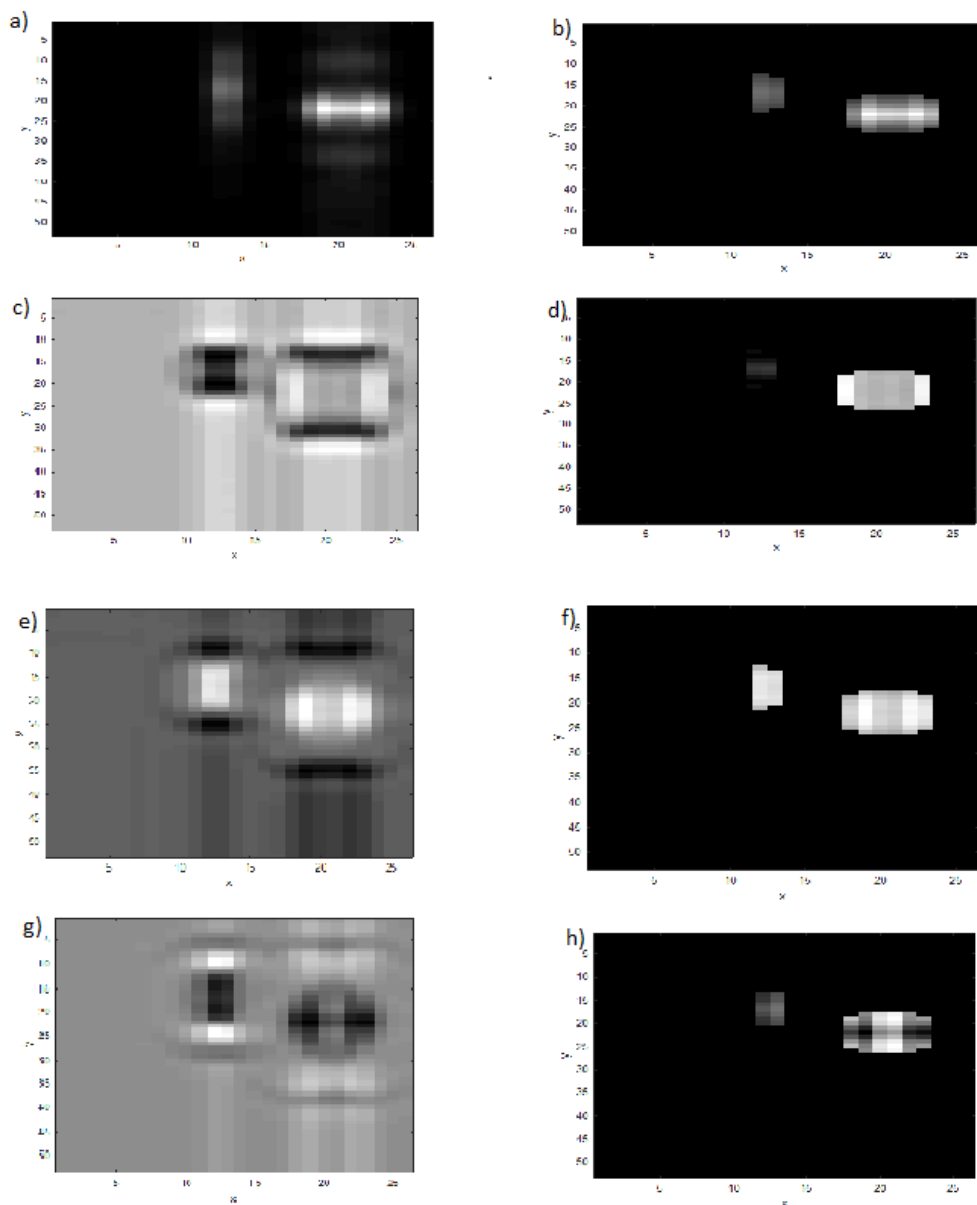


Figure 3.4: a) The image of the energy sum of the top view of the 3-D data created by combining the B-Scan data b) The masked image of the energy sum of the top view of the 3-D data created by combining the B-Scan data c)The image of C-Scan data at depth of 300 d) The masked image of C-Scan data at depth of 300 e)The image of C-Scan data at depth of 325 f) The masked image of C-Scan data at depth of 325 g)The image of C-Scan data at depth of 350 h) The masked image of C-Scan data at depth of 350

old value for the entropy-based segmentation method can be calculated as seen from equation 3.9[92][133].

$$H = \operatorname{argmax}_T(H_1(T) + H_2(T)) \quad (3.9)$$

where $H_1(T)$ and $H_2(T)$ are the respective region entropies. The entropy of each region can be expressed as

$$H_1(T) = - \sum_{i=0}^T \left(\frac{p_i}{P_T} \ln \frac{p_i}{P_T} \right) \quad (3.10)$$

$$H_2(T) = - \sum_{i=T+1}^{L-1} \left(\frac{p_i}{1 - P_T} \ln \frac{p_i}{1 - P_T} \right) \quad (3.11)$$

where P_T is the total probability, T is the optimal threshold, p_i is the probability of intensity level i . P_T can be expressed as

$$P_T = \sum_{i=0}^T p_i \quad (3.12)$$

The entropy for a region and the total entropy of the image can be expressed as

$$H_T = - \sum_{i=0}^T (p_i \ln p_i) \quad (3.13)$$

$$H_{total} = - \sum_{i=0}^{L-1} (p_i \ln p_i) \quad (3.14)$$

Equations 3.10 and 3.11 can be simplified as follows

$$H_1(T) = \ln(P_T) + \frac{H_T}{P_T} \quad (3.15)$$

$$H_2(T) = \ln(1 - P_T) + \frac{H_{total} - H_T}{1 - P_T} \quad (3.16)$$

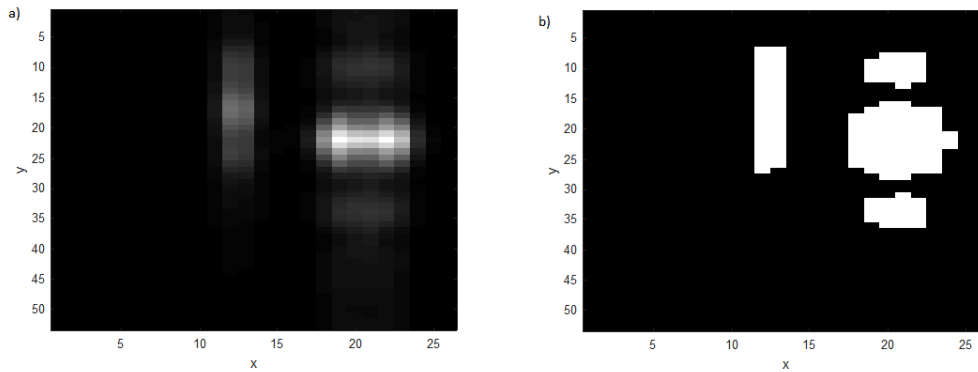


Figure 3.5: a) The image of the energy sum of the top view of the 3-D data created by combining the B-Scan data b) Binary image

After calculating the optimal threshold value according to the above equations, the binary image of the energy sum of the top view of the 3-D data created by combining the B-Scan data is obtained by using the threshold value as seen in figure 3.5. In this image, pixels above the threshold value are assigned to 1, and pixels below the threshold value are assigned to 0. Then, the obtained binary image masks the image of the energy sum of the top view of the 3-D data created by combining the B-Scan data, the image of C-Scan data at a depth of 300, the image of C-Scan data at a depth of 325, and the image of C-Scan data at a depth of 350. Feature vectors are extracted from these 4 masked images. The output of these mask processings can be seen in figure 3.6.

3.4 K-Means Clustering for Image Segmentation

Normally the K-means clustering method is a simple and very popular unsupervised learning method, which is used when you have unlabeled data. In this study, the K-means clustering algorithm is used for segmentation purposes. The purpose of this algorithm is to separate the data in accordance with the number of classes represented by the variable K. Classes are grouped according to similarity measure[169].

Assume that X is an image, which has N pixels. The K-means clustering method is minimizing the sum of the within-cluster variances(WCSS) to separate the image into

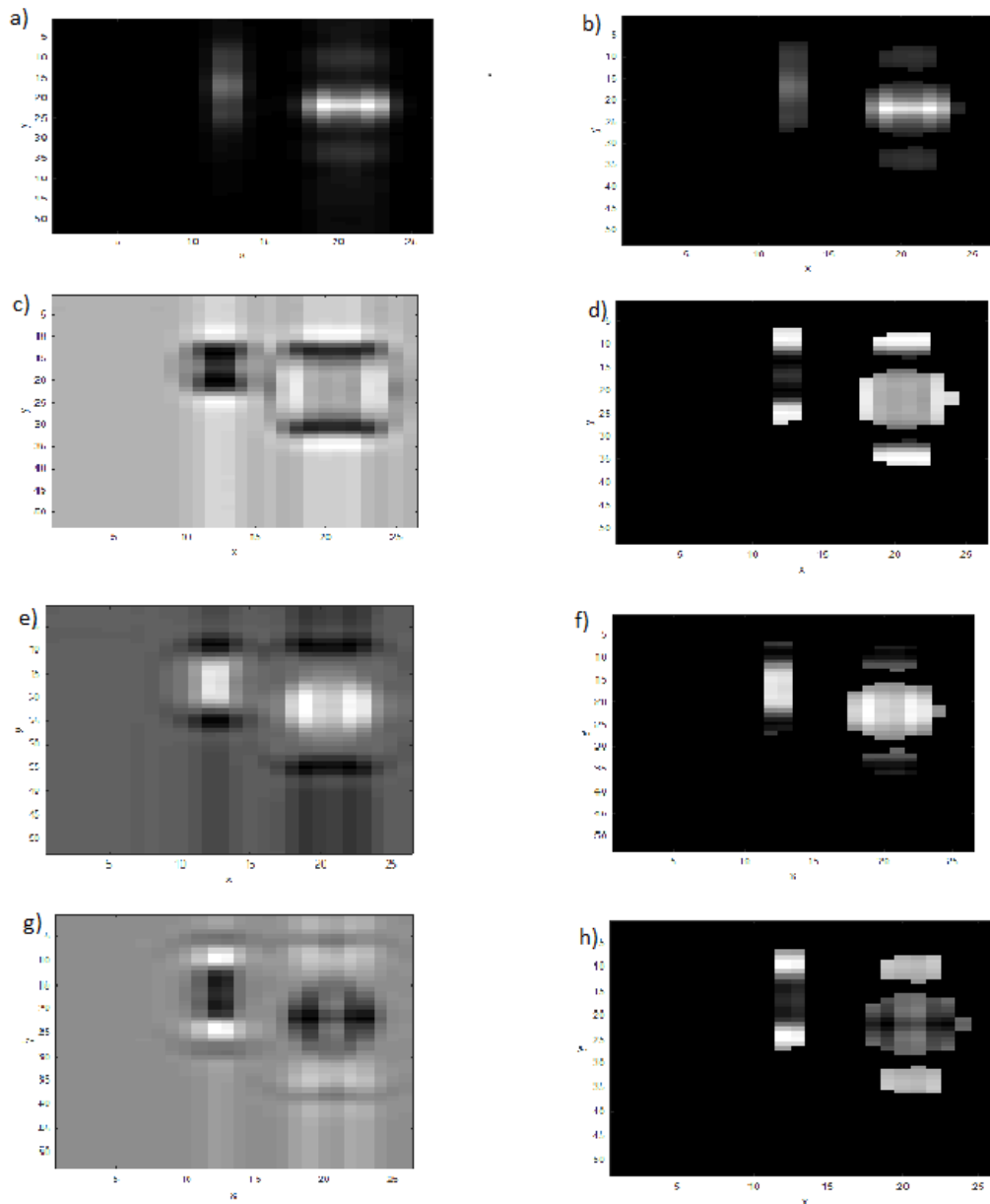


Figure 3.6: a) The image of the energy sum of the top view of the 3-D data created by combining the B-Scan data b) The masked image of the energy sum of the top view of the 3-D data created by combining the B-Scan data c)The image of C-Scan data at depth of 300 d) The masked image of C-Scan data at depth of 300 e)The image of C-Scan data at depth of 325 f) The masked image of C-Scan data at depth of 325 g)The image of C-Scan data at depth of 350 h) The masked image of C-Scan data at depth of 350

K-classes. WCSS can be expressed as shown in equation 3.17[137].

$$WCSS = \sum_{k=1}^K \sum_{i=1}^{N_k} \|x_i^k - c_k\|^2 \quad (3.17)$$

where x_i^k is the i -th sample of the k -th class and c_k is the centroid of the class, N_k represents the number of pixels in class k [137]. The algorithm of K-means clustering can be seen as follows[170][133]:

- Determine number of cluster K and K initial cluster centers
- Compute point-to-cluster-centroid distances of all observations to each centroid.
- Assign each observation to the cluster with the closest centroid.
- Calculate the average of observations in each cluster to calculate K new centroid
- Return to step 2 and Repeat until the position of the centroid in step 4 no longer changes

The K-means clustering method is computationally more efficient than other algorithms for segmentation. However, the desire to give the number of classes and the number of iteration at the beginning of the algorithm is a disadvantage for k-means clustering. In this study, K-value is 2 to be compatible with other methods, which are BCV and entropy-based segmentation, in the K-means clustering algorithm. If K is 2, the K-means clustering method shows similar results to BCV because, in both methods, the objective corresponds to the same situation. As a result of the K-means clustering method where K is 2, the binary image of the energy sum of the top view of the 3-D data created by combining the B-Scan data can be seen in figure 3.7. Then, the obtained binary image masks the image of the energy sum of the top view of the 3-D data created by combining the B-Scan data, the image of C-Scan data at a depth of 300, the image of C-Scan data at a depth of 325, and the image of C-Scan data at a depth of 350. Feature vectors are extracted from these 4 masked images. The output of these mask processings can be seen in figure 3.8.

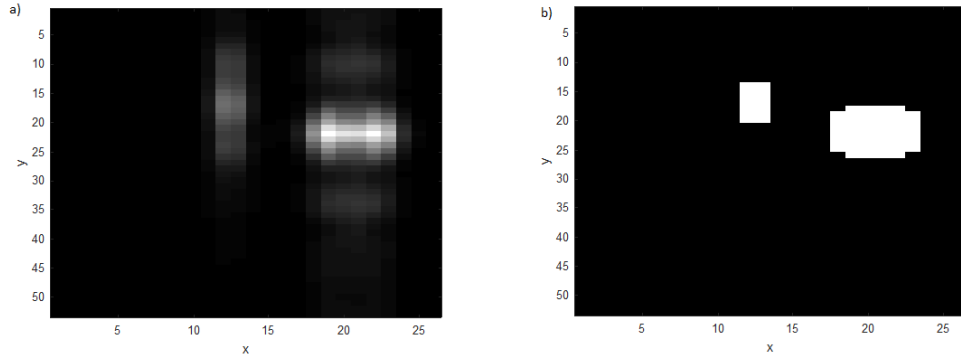


Figure 3.7: a) The image of the energy sum of the top view of the 3-D data created by combining the B-Scan data b) Binary image

3.5 Textural Feature Based Method for Feature Extraction

After applying the image segmentation algorithm to the image of the energy sum of the top view of the 3-D data created by combining the B-Scan data and images of C-Scan, the feature extraction stage is started as mention in the previous chapter. One of the feature extraction algorithms to be used in this thesis is the textural feature-based method. The textural feature contains information about the spatial arrangement of pixel intensities in an image or a selected region of the image[92]. As mentioned above, there are several methods proposed in the literature to capture textural features from an image, such as gray-level co-occurrence matrix(GLCM), gray-level run-length matrix(GLRLM), fractals, Gabor filters, and the wavelet transform. In this thesis, the gray-level co-occurrence matrix(GLCM) is used to capture textural features from an image.

GLCM is one of the well-known and old methods for texture features extraction[140][166][163]. The co-occurrence matrix is a two-dimensional histogram of gray-levels created by looking at the specific spatial direction and distance[92]. GLCM's are calculated between neighboring image pixel pairs for various distance and angle values. Here, δ and θ , respectively, represent distance and angle between neighboring image pixel pairs. The choice of distance δ is important for the detailed capturing of texture features. If the distance δ is selected too large, detailed capturing of textural features will not be possible. In textural feature based studies, distance δ value is generally

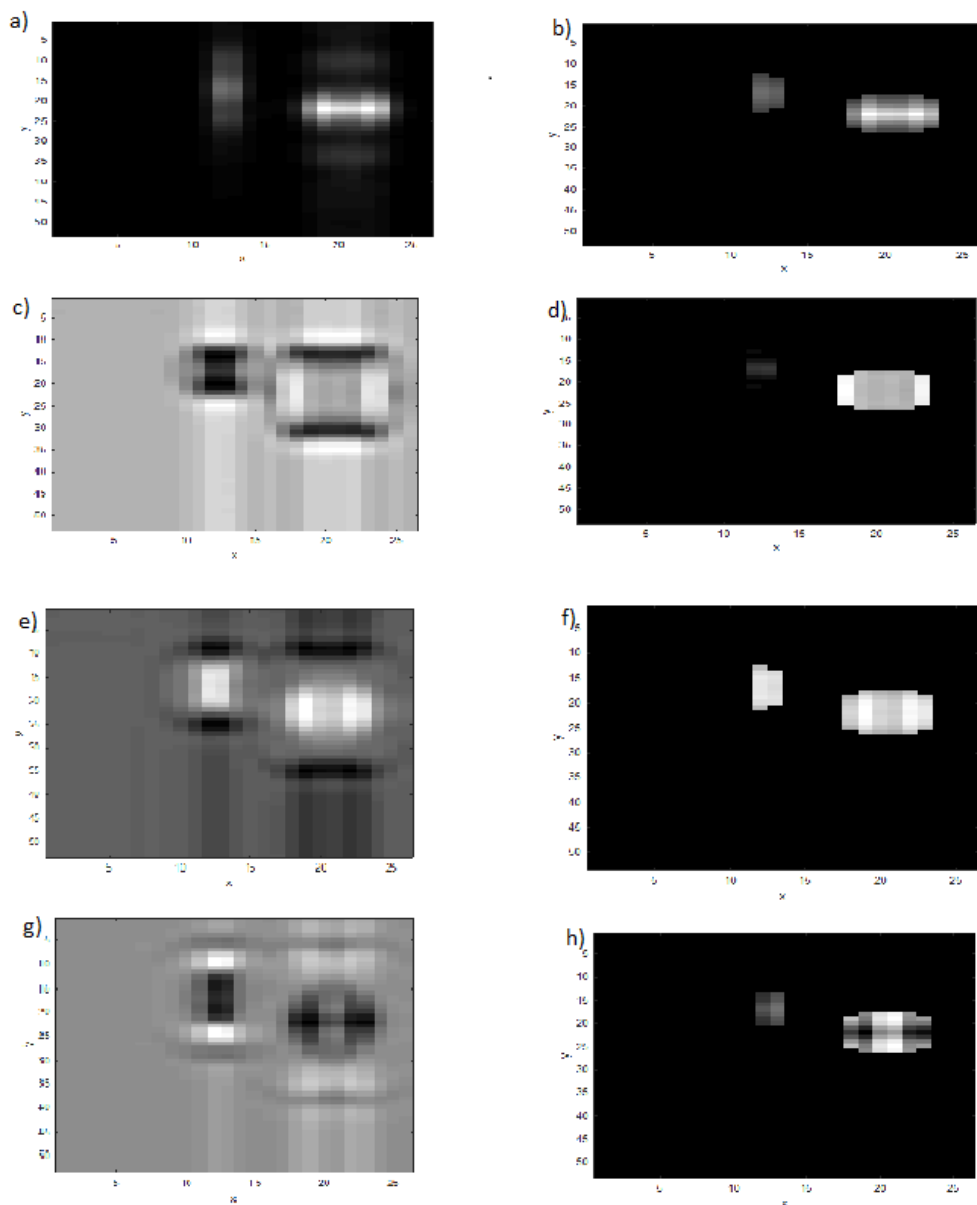


Figure 3.8: a) The image of the energy sum of the top view of the 3-D data created by combining the B-Scan data b) The masked image of the energy sum of the top view of the 3-D data created by combining the B-Scan data c)The image of C-Scan data at depth of 300 d) The masked image of C-Scan data at depth of 300 e)The image of C-Scan data at depth of 350 f) The masked image of C-Scan data at depth of 350 g)The image of C-Scan data at depth of 400 h) The masked image of C-Scan data at depth of 400

selected as 1 or 2. Also, except for edge pixels, each pixel has 8 different neighbors in angular 45 degree increments for calculating GLCM. As a result, θ can take 8 different values, which are $\theta = 0^0, 45^0, 90^0, 135^0, 180^0, 225^0, 270^0,$ and 315^0 . However, when creating the GLCM matrix from an image, the number of values that θ takes is reduced to 4, which are $0^0, 45^0, 90^0,$ and 135^0 , because $\theta = 0^0$ and 180^0 , $\theta = 45^0$ and 225^0 , $\theta = 90^0$ and 270^0 , $\theta = 135^0$ and 315^0 give the same results for GLCM's calculation[92]. The GLCM's for angles $0^0, 45^0, 90^0,$ and 135^0 can be define as[92]

$$G_{\delta,0}(p, q) = \sum_{n=1}^N \sum_{m=1}^M 1 \text{ if } I(n, m) = p \text{ and } I(n, m + \delta) = q, \quad 0 \text{ o.w.} \quad (3.18)$$

$$G_{\delta,45}(p, q) = \sum_{n=1}^N \sum_{m=1}^M 1 \text{ if } I(n, m) = p \text{ and } I(n - \delta, m + \delta) = q, \quad 0 \text{ o.w.} \quad (3.19)$$

$$G_{\delta,90}(p, q) = \sum_{n=1}^N \sum_{m=1}^M 1 \text{ if } I(n, m) = p \text{ and } I(n - \delta, m) = q, \quad 0 \text{ o.w.} \quad (3.20)$$

$$G_{\delta,135}(p, q) = \sum_{n=1}^N \sum_{m=1}^M 1 \text{ if } I(n, m) = p \text{ and } I(n - \delta, m - \delta) = q, \quad 0 \text{ o.w.} \quad (3.21)$$

where $p, q = 0, 1, \dots, L - 1$, I is NXM image which have L intensity level.

After calculating the GLCM for a given δ and θ , the GLCM is normalized so that the sum of the elements is 1[92]. The normalized GLCM can be defined as

$$G_{\delta,\theta}^N(p, q) = \frac{G_{\delta,\theta}(p, q)}{\sum_{p=0}^{L-1} \sum_{q=0}^{L-1} G_{\delta,\theta}(p, q)} \quad (3.22)$$

In here, figure 3.9 can be used as an example to construct glcm. In this example, the GLCM at $\delta = 1$ and $\theta = 0^0$ of 5X4 image which has 4 intensity level is constructed.

After GLCM was constructed, eight different features, which are contrast, correlation, energy, homogeneity, inverse difference moment, entropy, shade feature, and prominence feature are extracted from each normalized GLCM. In fact, there are many

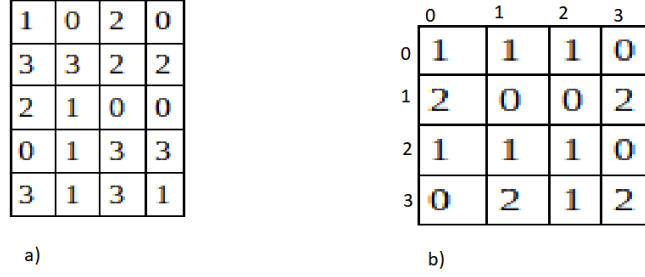


Figure 3.9: a) 5X4 image which has 4 intensity level b) GLCM

textural features except for these eight features mentioned above such as angular second moment, variance, sum average, sum entropy, difference variance, difference entropy, information measures of correlation, and maximal correlation coefficient[140]. However, many of these are not calculated in this thesis because many of them are correlated to these eight properties[140]. Contrast is a measure of the local variations presented in an image and defined as

$$Contrast = \sum_{p,q} (|p - q|^2 G_{\delta,\theta}^N(p, q)) \quad (3.23)$$

Correlation measures the linear dependency of gray levels on those of neighboring pixels or specified points. Correlation is defined as

$$Correlation = \sum_{p,q} \left(\frac{(p - \mu_x)(q - \mu_y) G_{\delta,\theta}^N(p, q)}{\sigma_x \sigma_y} \right) \quad (3.24)$$

where μ_x , σ_x and μ_y , σ_y are the means and standard deviations of the respective marginal distributions[92]. The energy is a measure of the textural uniformity and defined as

$$Energy = \sum_{p,q} (G_{\delta,\theta}^N(p, q))^2 \quad (3.25)$$

The homogeneity is a measure of the closeness of the distribution[92] and defined as

$$Homogeneity = \sum_{p,q} \frac{1}{1 + |p - q|} G_{\delta,\theta}^N(p, q) \quad (3.26)$$

The inverse difference moment measures the local homogeneity of an image and is defined as

$$InverseDifferenceMoment = \sum_{p,q} \frac{1}{1 + |p - q|^2} G_{\delta,\theta}^N(p, q) \quad (3.27)$$

Entropy measures the randomness of the image texture and is defined as

$$Entropy = \sum_{p,q} (-\ln(G_{\delta,\theta}^N(p, q))) G_{\delta,\theta}^N(p, q) \quad (3.28)$$

Shade measures skewness of the GLCM matrix and is defined as

$$Shade = sgn(A)|A|^{\frac{1}{3}} \quad (3.29)$$

where A is given by

$$A = \sum_{p,q} \frac{(p + q - 2\mu)^3 G_{\delta,\theta}^N(p, q)}{\sigma^3 (\sqrt{2(1 + correlation)})^3} \quad (3.30)$$

Prominence measures asymmetry of the GLCM and is defined as

$$Prominence = sgn(B)|B|^{\frac{1}{4}} \quad (3.31)$$

where B is given by

$$B = \sum_{p,q} \frac{(p + q - 2\mu)^4 G_{\delta,\theta}^N(p, q)}{4\sigma^4 (1 + correlation)^2} \quad (3.32)$$

3.6 Histogram of Oriented Gradients for Feature Extraction

Another feature extraction method used in this thesis is the Histogram of Oriented Gradients(HoG). The histogram of oriented gradients(HoG) is a feature descriptor used in the purpose of object detection for computer vision, machine learning, pattern recognition, and image processing, etc. Histogram of oriented gradients technique counts the occurrence of gradient orientation in local portions of the image. The algorithm steps of feature extraction using HoG can be seen as follows[171]:

- Preprocessing
- Calculate the gradient images
- Cell orientation histograms
- Block normalization
- Calculate the HoG feature vector

The first step of calculation in many feature detectors is the image pre-processing step. However, as Dalal and Triggs[151] have noted, the pre-processing step can be omitted in the HoG feature extraction process because the normalization process to be performed in the next step achieves essentially the same result. The pre-processing step provides little benefit in terms of performance[151].

To calculate an HoG descriptor, the second step is the calculation of the gradient images[171]. Firstly, the horizontal and vertical gradients are calculated. These are easily computed, respectively, by filtering the image with the kernels g_x and g_y as seen from equations 3.33 and 3.34[9].

$$I_x = I * g_x \quad (3.33)$$

$$I_y = I * g_y \quad (3.34)$$

where I is grayscale image, I_x, I_y are, respectively, the horizontal and vertical gradients, $g_x = [-1 \ 0 \ 1]$ and $g_y = [-1 \ 0 \ 1]^T$. Then, magnitude and angle of each pixel are computed as shown in equations 3.35 and 3.36[9].

$$\mu(i, j) = \sqrt{I_x(i, j)^2 + I_y(i, j)^2} \quad (3.35)$$

$$\theta(i, j) = \arctan \frac{I_y(i, j)}{I_x(i, j)} \quad (3.36)$$

where $\mu(i, j)$ is the magnitude of the image gradient of each pixel and $\theta(i, j)$ is the angle of the image gradient of each pixel. Here for now, "unsigned" gradients are used because, in the study of Dalal and Triggs, unsigned gradients gave better results. The angles are between 0 and 180 instead of 0 and 360. That is, it's negative are represented by the same numbers. For "signed" gradients, the angles are between 0 and 360. Moreover, although Dalal and Triggs[151] conducted tests using other filters such as 3x3 Sobel mask or diagonal masks, these masks generally performed poorly in detecting humans in images. Also, they experimented with a Gaussian smoothing filter before applying the derivative mask. However, this filter removed useful details in images[151].

Representation of image gradients can be seen in figure 3.10. Horizontal gradient of input image can be seen in figure 3.10 b. Vertical gradient of input image can be seen in figure 3.10 c. Total gradient of input image can be seen in figure 3.10 d.

The third step is cell orientation histograms. In this step, the image is divided into CXC cells, which are adjacent and non-overlapping. A histogram of gradient orientations binned into B bins is calculated for each CxC cells. Here, as C and B values, the values that give the best results in the study of Dalal and Triggs[151] are used to describe the HoG feature extraction method. That is, C is equal to 8 and B is equal to 9. As a result, the image is divided into cells and each cell contains 8x8 pixels as shown in figure 3.11. As shown in figure 3.11, this image contains 18 cells.

Specifically, the bins are numbered 0 through $B - 1$ and have width $w = \frac{180}{B}$. Bin i has boundaries $[wi, w(i + 1)]$ and center $c_i = w(i + \frac{1}{2})$ [171]. For B=9, diagram of

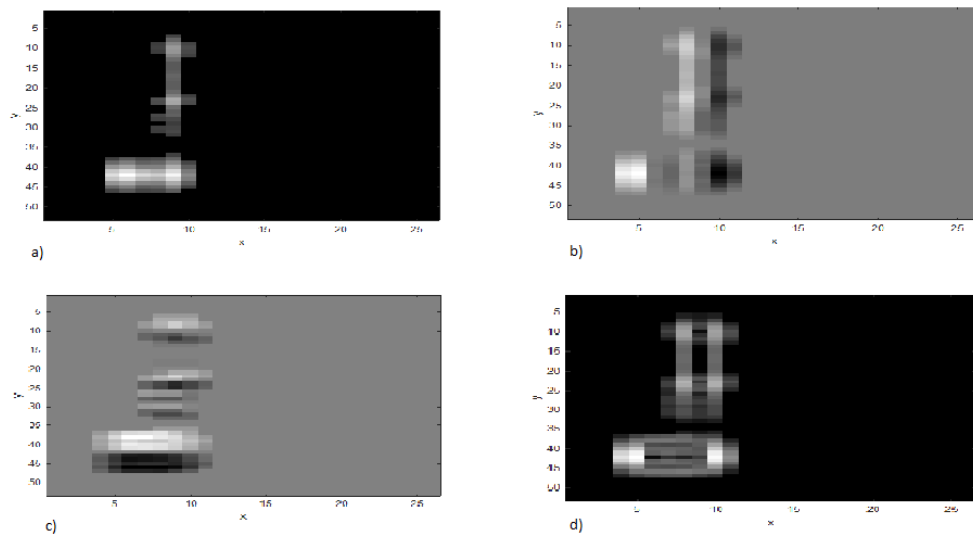


Figure 3.10: a) Input image b) Horizontal image gradient c) Vertical image gradient d) Image gradient

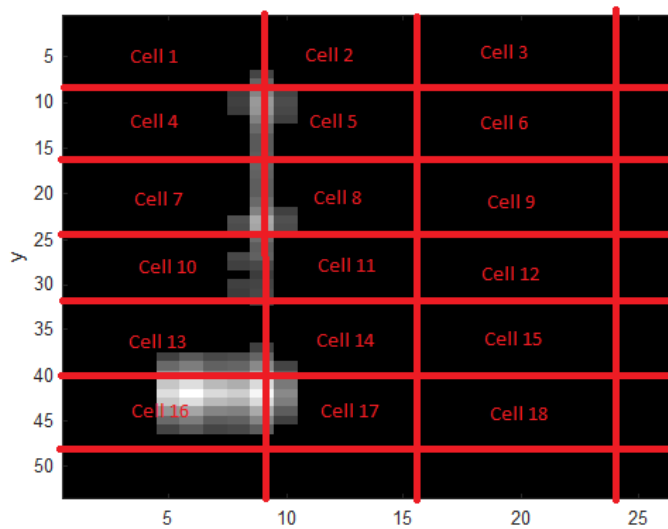


Figure 3.11: Representation of HoG cells

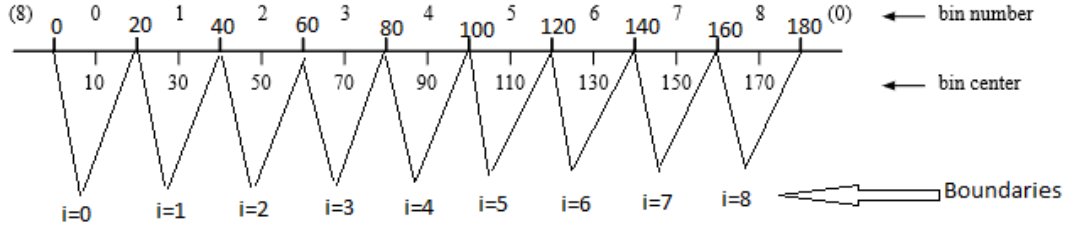


Figure 3.12: Representation of bin number, bin center and boundaries for B=9

bin numbers and bin centers can be seen in figure 3.12. A pixel with magnitude μ and orientation θ contributes a vote[171]

$$v_j = \mu \frac{c_{j+1} - \theta}{w} \text{ to bin number } j \quad (3.37)$$

and a vote

$$v_{j+1} = \mu \frac{\theta - c_j}{w} \text{ to bin number } j + 1 \quad (3.38)$$

According to equations 3.37 and 3.38, for $B = 9$, for instance, a gradient with orientation $\theta = 85$ degrees and magnitude 9 contributes 2.25 to bin 3 and 6.75 to bin 4. The sum of the two contributions always gives magnitude. According to equations 3.37 and 3.38, for $B = 9$, for instance, a gradient with orientation $\theta = 50$ degrees and magnitude 9 contributes 9 to bin 2 and 0 to bin 3. The sum of the two contributions always gives magnitude. The contributions of all the pixels in the 8x8 cells are added up to create the 9-bin histogram. As a result, for each cell, gradient and angle values of 64 pixels are calculated and one histogram is created with length 9.

The fourth step is block normalization. For the input image, blocks can be seen in figure 3.13. Here there are 10 blocks and each neighboring block contains 2 common cells between them as shown in figure 3.13 and each block is shown in different colors. As shown in figure 3.13, first block consists of cells 1, 2, 4 and 5, second block consists of cells 2, 3, 5 and 6, third block consists of cells 4, 5, 7 and 8, fourth block consists of cells 5, 6, 8 and 9, fifth block consists of cells 7, 8, 10 and 11, sixth block consists of cells 8, 9, 11 and 12, seventh block consists of cells 10, 11, 13 and

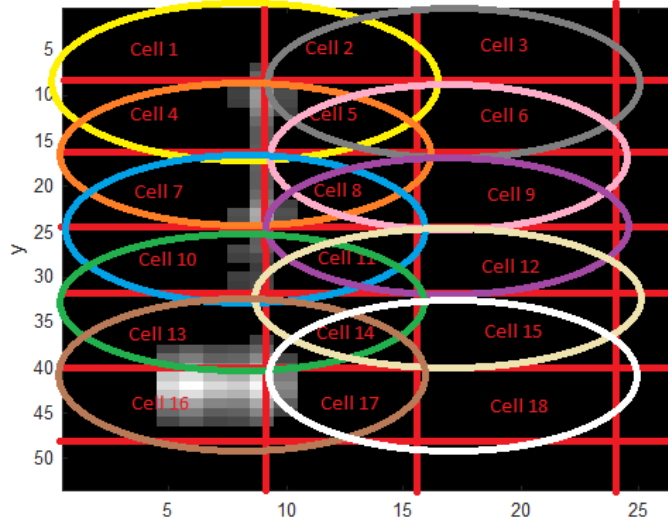


Figure 3.13: Representation of blocks of HoG feature extraction methods

14, eight block consists of cells 11, 12, 14 and 15, ninth block consists of cells 13, 14, 16 and 17, tenth block consists of cells 14, 15, 17 and 18. Let, $H(c_i)$ denotes the histogram of cell- i . For each block, histograms of four cells are concatenated together and normalized to obtain a 36-dimensional feature descriptor. Normalization for block 1 can be seen in equation 3.39. For the other 9 blocks, normalization is performed in the same way.

$$H_1 = \frac{[H(c_1), H(c_2), H(c_4), H(c_5)]}{\sqrt{\|H(c_1)\|_2^2 + \|H(c_2)\|_2^2 + \|H(c_4)\|_2^2 + \|H(c_5)\|_2^2}} \quad (3.39)$$

Finally, these ten vectors ($H_1, H_2, H_3, H_4, H_5, H_6, H_7, H_8, H_9$ and H_{10}) are concatenated to obtain the final 360-dimensional feature vector for one image.

3.7 Support Vector Machine for Classification

After applying the feature extraction algorithms to obtain feature vectors, the classification stage is started as mention in the previous chapter. Classification algorithm to be used in this thesis is the support vector machine(SVM), which is one of the most popular supervised learning algorithm that can be used for binary classification or regression. In this thesis, the two-class support vector machine algorithm is applied to

determine whether the target is a human or irrelevant object. The purpose of SVM is to construct optimal hyperplane as a decision boundary such that the margin of separation between the two classes in the data is maximized[155]. Support vectors are defined as samples that are used as support for the optimal location of the decision boundary[155]. Moreover, support vectors are the nearest data points to the decision boundary. SVM offers different types of solutions for use in the linearly separable case and linearly non-separable case.

Linear SVM algorithm is divided into two as hard margin method and soft margin method. If any two-classes are linearly separable, for a given $(x_1, y_1), \dots, (x_n, y_n)$ where y_i indicate the labeled class to which feature vectors x_i belong, any linear hyperplane can be written as equation 3.40[158]

$$y = w^T x + b \quad (3.40)$$

where w is the normal vector to the hyperplane and b is bias. As shown in figure 3.14, in hard margin method, two parallel hyperplanes are selected to separate the two classes of data, so that the distance between them is as large as possible. With a normalized or standardized dataset, as shown in figure 3.14, for class 1 and class 2, respectively, the equations of these hyperplanes can be defined as

$$w^T x + b = 1 \quad (3.41)$$

$$w^T x + b = -1 \quad (3.42)$$

These hyperplanes are determined using the support vectors as shown in figure 3.14. These hyperplanes are parallel because they have the same w and b values as can be seen from the equations 3.41 and 3.42. The region between these two hyperplanes is called the "margin". As mentioned above, the purpose of the SVM algorithm is to maximize this margin. Since margin is directly proportional to $\frac{2}{\|w\|^2}$, if $\|w\|^2$ is minimized, margin is maximized[9]. The decision boundary is the hyperplane that lies halfway between two parallel hyperplanes[9][154][158]. The equation of decision

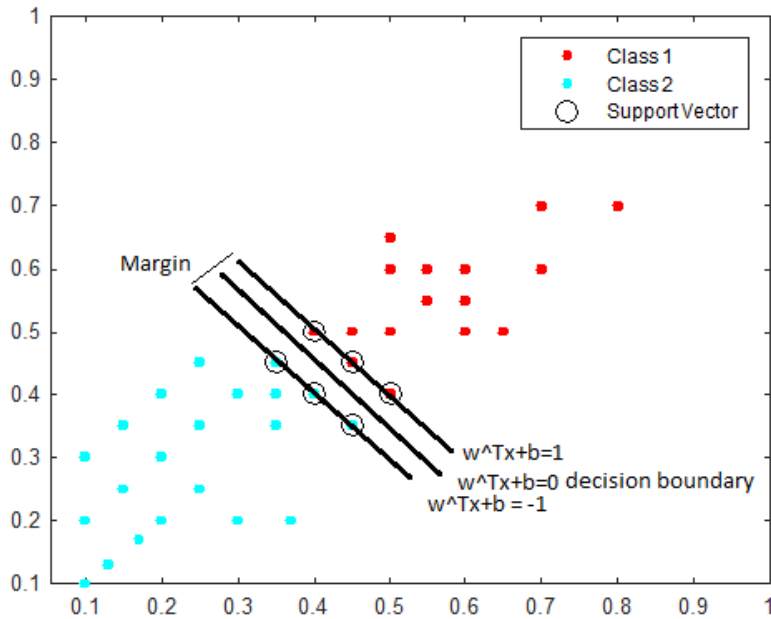


Figure 3.14: Example of representation of two classes applied linearly separable SVM

boundary can be defined as

$$w^T x + b = 0 \tag{3.43}$$

For the linear SVM hard margin method, after finding the decision boundary with the help of training data, it is necessary to find out which class the test data belongs to. Assume that x_i is a test point.

IF

$$w^T x_i + b > 0 \tag{3.44}$$

x_i belongs to class 1 shown in figure 3.14. That is, y_i , which is the label of x_i , is equal to 1.

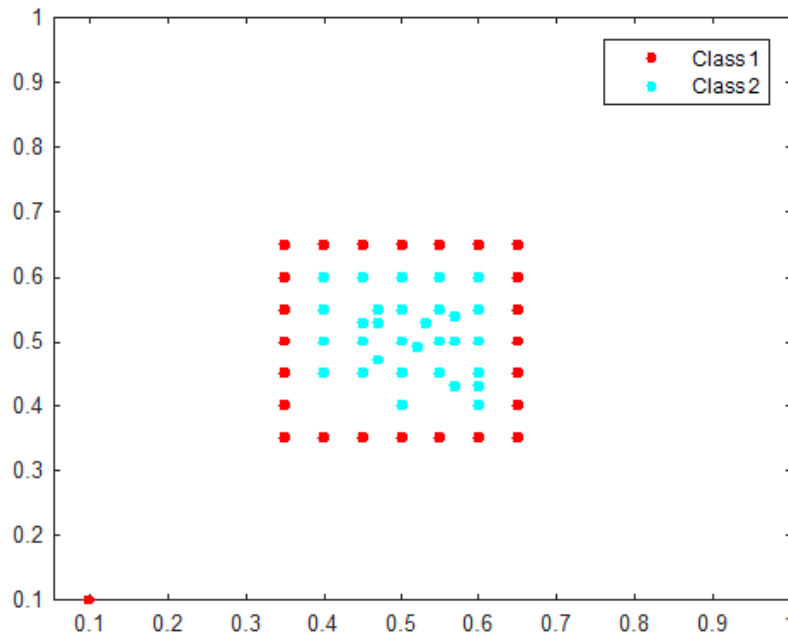


Figure 3.15: Example of linearly non-separable two classes

OR

$$w^T x_i + b < 0 \tag{3.45}$$

x_i belongs to class 2 shown in figure 3.14. That is, y_i , which is the label of x_i , is equal to -1.

The extended version of the hard margin SVM is the soft margin method. In the soft margin method, data belonging to a class is allowed to be on the other side of the decision boundary. In case of the margin is smaller or all data points are not labeled correctly, the soft margin extension of the SVM algorithm can be used[9]. For more information about the soft margin method, please examine references [158][9][156] [157].

Figure 3.15 is an example of a linearly non-separable case in two-class SVM algorithms. These two classes cannot be separated using the linear SVM algorithm. By using various kernel functions, data vectors are mapped to higher-dimensional space

Table 3.1: Types of kernel functions

Types of Kernel Functions	Parameters
Gaussian or Radial Basis Function(RBF)	Standard deviation(sigma)
Polynomial	Standard deviation(sigma) and degree

so that data vectors in this dimensional space are linearly seperable[172]. The kernel function types used can be seen in the table 3.1.

CHAPTER 4

RESULTS AND DISCUSSIONS

In this chapter, the results of the simulations, the results and the performances of the algorithms described in the previous chapter will be presented. Also, the algorithms used for image segmentation, (which are between-class variances, entropy-based segmentation, and K-means clustering) feature extraction, (which are the textural based method, and HoG) and classification (which are SVM) will be compared in terms of performance. Various discussions will also be presented about through the wall imaging and detecting.

4.1 Dataset and Simulation Results

In this thesis, humans and various objects in a room, behind the wall, are simulated by using gprMax software[173][174][175]. Although gprMax software is generally used in Ground Penetrating Radar studies, it is used in the TWRI application as it is known in this thesis. gprMax is an open-source software that simulates electromagnetic wave propagation by solving Maxwell's equations in 3D using the Finite-Difference Time-Domain(FDTD) method[173]. To examine the FDTD method in detail, the references [176], [177], and [178] can be glanced. A sample of gprMax input file and some points to consider when creating models in gprMax are given in Appendix A.

In this thesis, 108 different scenarios are simulated by using gprMax software to detect human and other objects by utilizing image processing and classification algorithms. There are common and different points in these scenarios. Size of models, the values of the discretization spatial and temporal steps of models, number of cells in models, the time window of models, iteration numbers, number of threads used,

the position of room in models, size of room in models, electromagnetic properties of the human material, type, center frequency and amplitude of waveform, type of transmitter and receiver antennas, step size of transmitter and receiver for forming B-Scan image, step size of transmitter and receiver for forming C-Scan image, distance of transmitter and receiver to wall, distance between transmitter and receiver antennas etc. are common points in these scenarios. Size of simulation models is $80 \times 60 \times 15 \text{ cm}^3$. Compared to real life, all dimensions in simulation models have been reduced to the same extent due to the memory, processing capacity of the computer and time. The dimensions in real life are approximately 18 times the simulation model dimensions. The values of the discretization spatial steps in these scenarios are $2 \times 2 \times 2 \text{ mm}^3$. The value of the discretization temporal step in these scenarios is nearly equal to 3.85×10^{-12} . The number of cells in these scenarios is 9×10^6 . The time window of models is 4ns. Iteration number in these scenarios is nearly equal to 1040. Refer to Appendix A for the calculation method of the value of the discretization temporal step, number of cells, and iteration number. The number of threads used in these scenarios is 8. Size of simulation model, the values of the discretization spatial and temporal steps, number of cells in model, which depends on size of simulation model and the values of the discretization spatial steps as shown in Appendix A, time window of model, iteration number, which depends on time window of model and the value of the discretization temporal step as shown in Appendix A, and number of threads used are important factors in influencing simulation speed. The time it takes to obtain an A-Scan data in various parameters for 2 threads used is shown in figure 4.1. For figure 4.1 a, size of model is $80 \times 60 \times 15 \text{ cm}^3$, the values of discretization spatial steps is $2 \times 2 \times 2 \text{ mm}^3$, the value of discretization temporal step is 3.85 ps , and time window of model is 4ns. For figure 4.1 b, size of model is $40 \times 30 \times 15 \text{ cm}^3$, the values of discretization spatial steps is $2 \times 2 \times 2 \text{ mm}^3$, the value of discretization temporal step is 3.85 ps , and time window of model is 4ns. For figure 4.1 c, size of model is $80 \times 60 \times 15 \text{ cm}^3$, the values of discretization spatial steps is $4 \times 4 \times 4 \text{ mm}^3$, the value of discretization temporal step is 7.7 ps , and time window of model is 4ns. For figure 4.1 d, size of model is $80 \times 60 \times 15 \text{ cm}^3$, the values of discretization spatial steps is $2 \times 2 \times 2 \text{ mm}^3$, the value of discretization temporal step is 3.85 ps , and time window of model is 2ns. As shown in figure 4.1, if the size of the model is decreased, or the values of discretization spatial and temporal steps are increased, or time window of

the model is decreased, the time it takes to obtain an A-Scan data decreases. However, when determining the above-mentioned parameters, besides the memory, the processing capacity of the computer used and the simulation speed, another consideration is the spatial resolution of the B-Scan and the C-Scan images. The increase in the discretization spatial steps shortens the simulation time whereas it reduces the spatial resolution of the B-Scan and C-Scan images as shown in figure 4.2. For obtaining figure 4.2, Scenario 1 which can be seen in Appendix B, C, and D is used. For figure 4.2 a and b, discretization spatial steps are $2x2x2mm^3$. For figure 4.2 c and d, discretization spatial steps are $4x4x4mm^3$. For figure 4.2 e and f, discretization spatial steps are $5x5x5mm^3$. Also, the value of the time window is another factor affecting spatial resolution in the B-Scan and C-Scan images. As shown in figure 4.3, the spatial resolution increases if the value of the time window is increased. For obtaining figure 4.3, Scenario 1 which can be seen in Appendix B, C, and D is used. For figure 4.3 a, time window is 1ns. For figure 4.3 b, time window is 2ns. For figure 4.3 c, time window is 4ns. Taking into account all of the above-mentioned cases, which are memory, processing capacity of a computer used, simulation speed and the spatial resolution of the B-Scan and C-Scan images, the above-mentioned parameters were selected at their optimal values.

gprMax software includes modeling of antenna types such as bowtie antenna model, wire dipole antenna model, and Hertzian dipole etc[173]. For these scenarios, the Hertzian dipole and Gaussiandot waveform which has 1.5 GHz center frequency and 10 Amps amplitude are used as a transmitter, receiver antennas, and waveform, respectively. Gaussiandot is the first derivative of a Gaussian waveform. Representation of time domain and power spectrum of the Gaussian waveform which has 1.5 GHz center frequency and 10 Amps amplitude can be seen in figure 4.4. Because the spatial resolution of B-Scan and C-Scan images obtained with Hertzian dipole is lower than other antenna types, it becomes more meaningful to test image processing and classification algorithms. Therefore, in this thesis, Hertzian dipoles are used as transmitter and receiver antennas. Also, as mentioned in the previous chapters, center frequency selection is important for dispersion, attenuation, and spatial resolution. 1.5 GHz center frequency is used in these scenarios because it gives positive results in terms of dispersion, attenuation, and spatial resolution. Apart from gaussiandot,

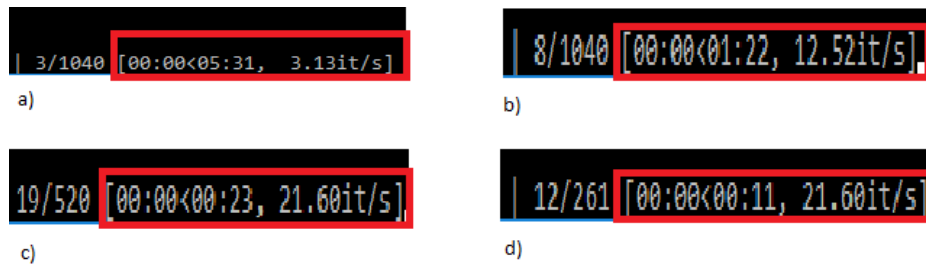


Figure 4.1: a) Size of model at $80 \times 60 \times 15 \text{ cm}^3$, the values of discretization spatial steps at $2 \times 2 \times 2 \text{ mm}^3$, the value of discretization temporal step at 3.85 ps, time window of model:4ns b) Size of model at $40 \times 30 \times 15 \text{ cm}^3$, the values of discretization spatial steps at $2 \times 2 \times 2 \text{ mm}^3$, the value of discretization temporal step at 3.85 ps, time window of model:4ns c) Size of model at $80 \times 60 \times 15 \text{ cm}^3$, the values of discretization spatial steps at $4 \times 4 \times 4 \text{ mm}^3$, the value of discretization temporal step at 7.7 ps, time window of model:4ns d) Size of model at $80 \times 60 \times 15 \text{ cm}^3$, the values of discretization spatial steps at $2 \times 2 \times 2 \text{ mm}^3$, the value of discretization temporal step at 3.85 ps, time window of model:2ns

various waveform models can be used in the gprmax software such as gaussian, gaussiandotnorm, gaussiandotdot, gaussiandotdotnorm, ricker, sine, contsine. gaussian is Gaussian waveform, gaussiandotnorm is the normalized first derivative of a Gaussian waveform, gaussiandotdot is the second derivative of a Gaussian waveform, gaussiandotdotnorm is the normalized second derivative of a Gaussian waveform, ricker is a Ricker (or Mexican Hat) waveform, sine is a single cycle of a sine waveform, contsine is a continuous sine waveform[173].

The size of the room is $80 \times 60 \times 10 \text{ cm}^3$ for all scenarios. The position and size of the room in these scenarios can be seen in figure 4.5. The distance of the transmitter and receiver to the wall is 2cm and the distance between transmitter and receiver antennas is 2cm as shown in figure 4.6.

The electromagnetic properties of the human material in these scenarios can be seen in table 4.1. Humans have different electromagnetic properties at different frequencies. The gprMax software contains a human's electromagnetic model called AustinMan [173]. However, AustinMan could not be utilized due to the memory and ram capacity of the computer used in this thesis. Also, electromagnetic modeling of the human

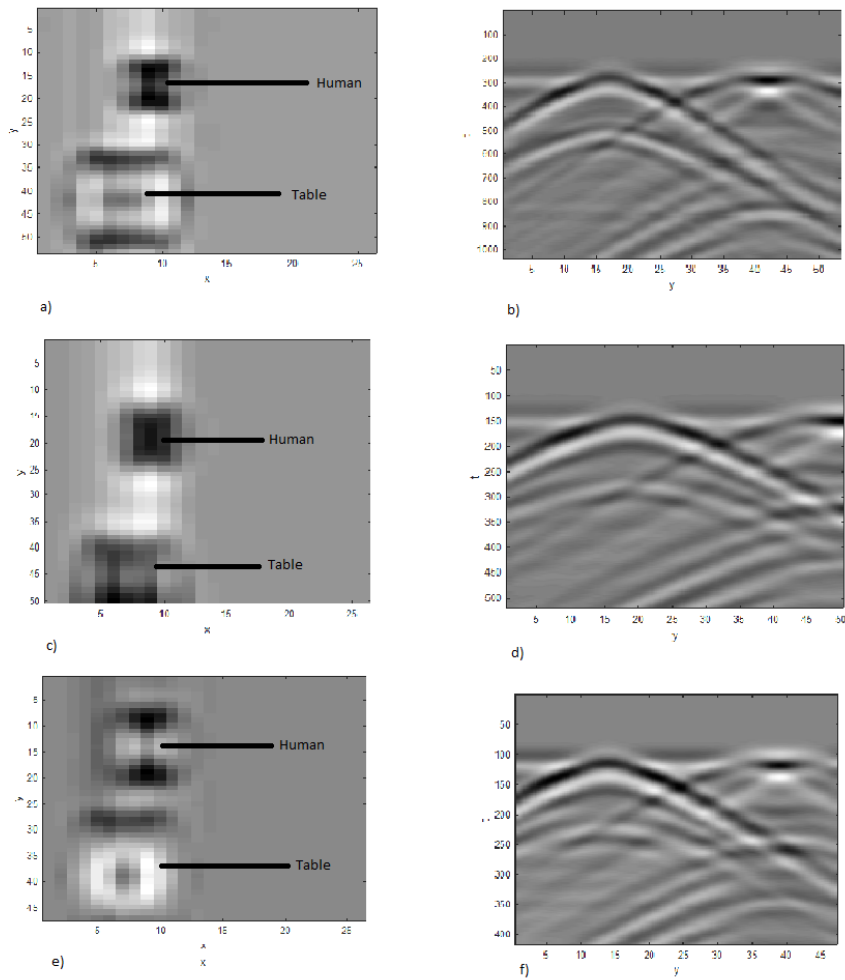


Figure 4.2: a) C-Scan image which have $2 \times 2 \times 2$ discretization spatial steps b) B-Scan image which have $2 \times 2 \times 2$ discretization spatial steps c) C-Scan image which have $4 \times 4 \times 4$ discretization spatial steps d) B-Scan image which have $4 \times 4 \times 4$ discretization spatial steps e) C-Scan image which have $5 \times 5 \times 5$ discretization spatial steps f) B-Scan image which have $5 \times 5 \times 5$ discretization spatial steps

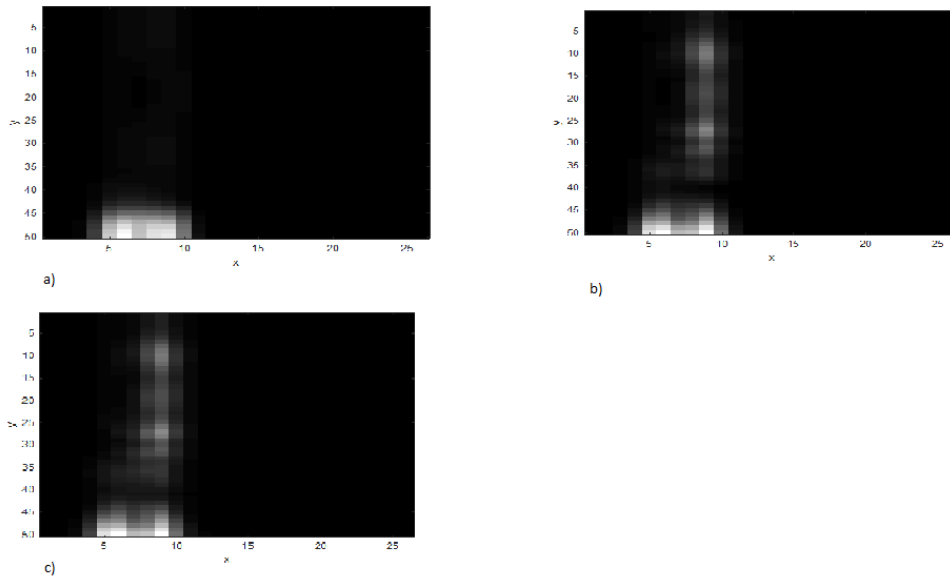


Figure 4.3: a) Time window = 1ns b) Time window = 2ns c) Time window = 4ns

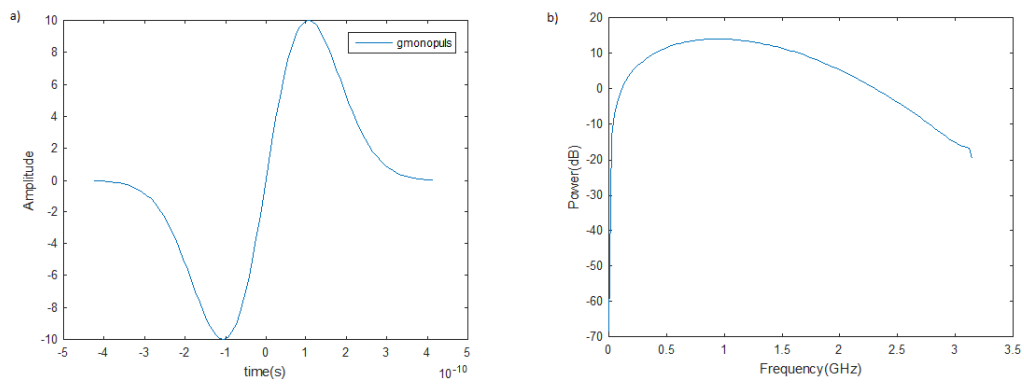


Figure 4.4: a) Representation of time domain of the gaussian waveform b) Representation of power spectrum of the gaussian waveform

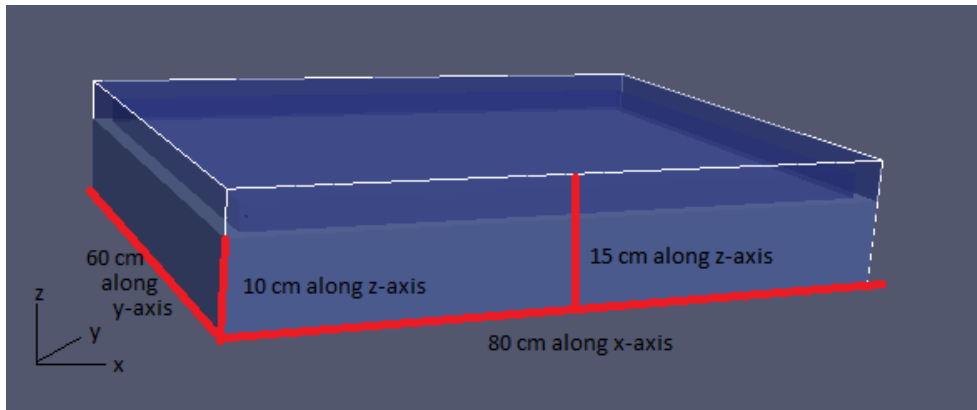


Figure 4.5: Representation of size and position of the room

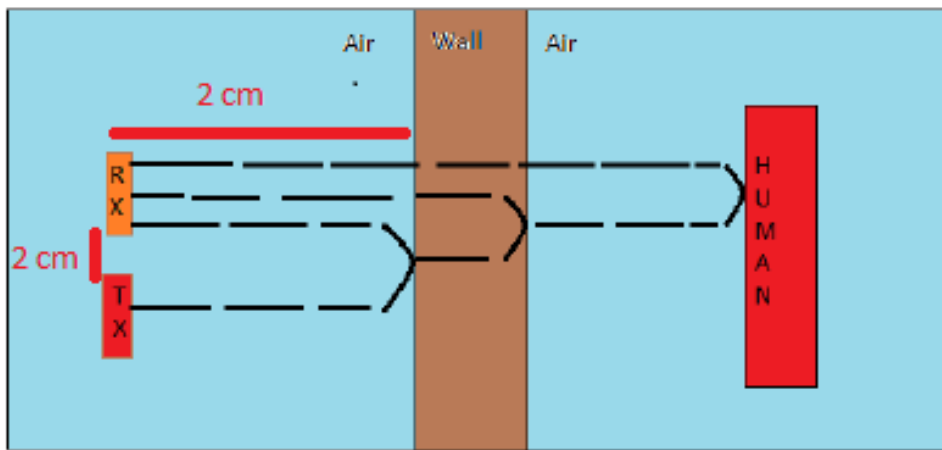


Figure 4.6: The distance between antennas and wall, and the distance between transmitter and receiver antennas

Table 4.1: Electromagnetic properties of the human material in 108 scenarios

Relative Permittivity	Conductivity	Relative Permeability	Magnetic Loss
8	0.065	1	0

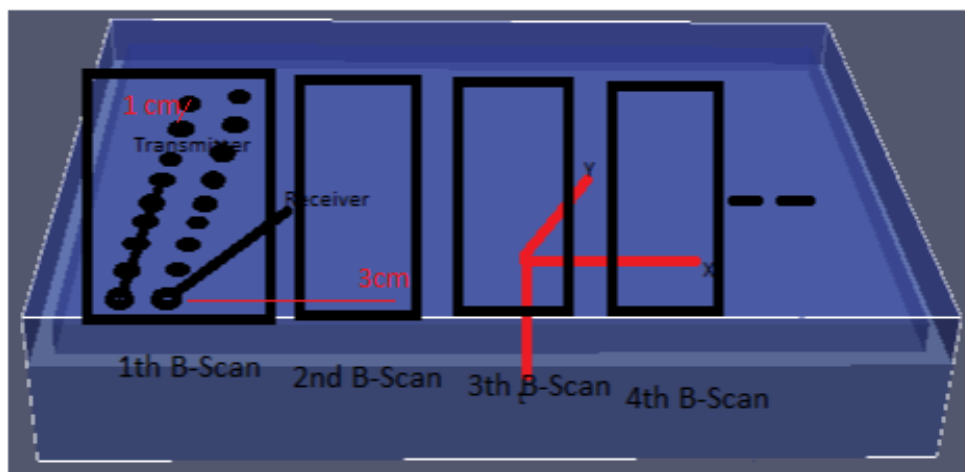


Figure 4.7: Representation of forming of B-Scan and C-Scan datas

head between 0.1 GHz and 5 GHz was performed in the reference[179]. Referring to these two sources, since the characteristics specified in table 4.1 are closest to electromagnetic properties of the skull, blood, white matter and fat parts of the human being, they are chosen as electromagnetic properties of human in these scenarios.

In these scenarios, the transmitter and receiver antennas are moved 59 times along the y-direction by 1 cm apart to form a B-scan image. That is, a B-Scan data consists of 59 A-Scan data. Also, in these scenarios, the C-Scan image and 3D data are the results of combining 26 B-Scan data. To obtain 26 different B-Scan data, the receiver and transmitter antennas are shifted 3 cm apart from the starting position along the x-direction. These situation can be seen in figure 4.7.

Electromagnetic properties of the room material, electromagnetic properties of the object(not human) material, the thickness of the wall, size of human, position of human, the model of the object (not human), position of the object (not human) are different points in these scenarios.

As is known, in real life, through the wall imaging and detecting applications are not

Table 4.2: Electromagnetic properties of different wall types in 108 scenarios

Wall Type	1	2	3	4	5	6
Relative Permittivity	3	4	5	7	9	10
Conductivity	0.01	0.01	0.01	0.01	0.01	0.01
Relative Permeability	1	1	1	1	1	1
Magnetic Loss	0	0	0	0	0	0

applied to one type wall. As mentioned above, the different wall materials are used in this thesis. In this thesis, 6 different wall materials are used. The wall material has a uniform structure in itself. The electromagnetic properties of the wall materials can be seen in table 4.2. As shown in table 4.2, conductivity, relative permeability and magnetic loss of 6 different materials are the same. In this study, wall materials without magnetic loss and wall materials which have relatively low conductivity are selected. Moreover, because the walls used in this type of studies do not have magnetic properties, relative permeability is chosen as 1. Here, the relative permittivity determines the difference of materials. In the references [180], [16], and [181], studies have been conducted on the relative permittivity of different wall materials at 1.5 GHz center frequency. According to these studies, wall type 1 is plasterboard, wall type 2 is brick, wall type 3 is concrete, wall type 4 is glass, and wall type 5 and 6 consist of concrete portland cement, sand, small gravel and water in different amounts. Which wall type is used during the 108 scenarios can be seen from the tables C.1, C.2, C.3 and C.4 in Appendix C. The effect of the relative permittivity of the wall can be seen in figure 4.8. For obtaining figure 4.8, scenario 1 is used. For figure 4.8 a and c, the relative permittivity of the wall is 3. For figure 4.8 b and d, the relative permittivity of the wall is 10. Here, other factors are the same except the relative permittivity of the wall. The images are faint when the relative permittivity of the wall is higher.

As is known, in real life, through the wall imaging and detecting applications are not applied to one type object(not human). Objects with different electromagnetic properties and different models are used in this thesis. In this thesis, 15 different object materials and 12 different object model are used. The object material has a

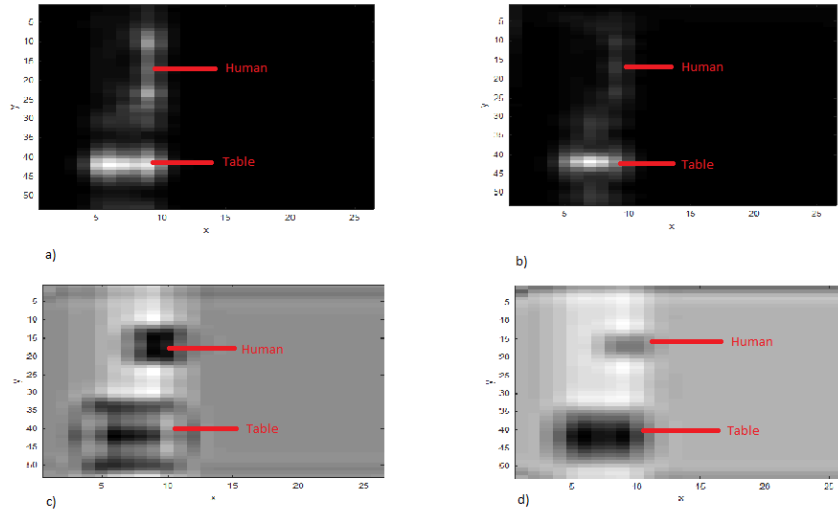


Figure 4.8: a) The image of the energy sum of the top view of the 3-D data created by combining the B-Scan data, wall relative permittivity=3 b) The image of the energy sum of the top view of the 3-D data created by combining the B-Scan data, wall relative permittivity = 10 c) C-Scan image, wall relative permittivity=3 d) C-Scan image, wall relative permittivity = 10

uniform structure in itself. The electromagnetic properties of the object materials can be seen in table 4.3. As shown in table 4.3, conductivity, relative permeability, and magnetic loss of 15 different materials are the same. In this study, object materials without magnetic loss and object materials which have relatively low conductivity are selected. Because relative permeability 1 is selected, the object does not have magnetic properties. In here, the relative permittivity determines the difference of materials. In the references [180], [16], and [181], studies have been conducted on the relative permittivity of different materials at 1.5 GHz center frequency. According to these studies, object type 1 is ceiling board, object type 2 is wood, object type 3 is chipboard, object type 4 is plaster board, object type 5 is floorboard, object type 6 is concrete, object type 7 is concrete, object types 8, 9, 10 are different type glass, object type 12, 13, 14, and 15 consist of concrete portland cement, sand, small gravel and water in different amounts. In addition, as mentioned above, 12 different types of object models are studied in this thesis. These are table, prism, sphere with radius 2 cm, sphere with radius 3 cm, sphere with radius 4 cm, two sphere with radius 2 cm, two sphere with radius 3 cm, two sphere with radius 4 cm, such as human a which

Table 4.3: Electromagnetic properties of different objects(not human) in 108 scenarios

Object Type	Relative Permittivity	Conductivity	Relative Permeability	Magnetic Loss
1	1.5	0.01	1	0
2	2	0.01	1	0
3	2.5	0.01	1	0
4	3	0.01	1	0
5	3.5	0.01	1	0
6	5	0.01	1	0
7	5.5	0.01	1	0
8	6	0.01	1	0
9	6.5	0.01	1	0
10	7	0.01	1	0
11	7.5	0.01	1	0
12	9	0.01	1	0
13	9.5	0.01	1	0
14	10	0.01	1	0
15	11	0.01	1	0

can be seen in table 4.5, such as human d which can be seen in table 4.5, such as human, and two cylinder with length 10 cm and radius 1 cm. Which object type and object model are used during the 108 scenarios can be seen from the tables C.1, C.2, C.3, C.4, C.5, C.6, C.7, and C.8 in Appendix C. Images of different object models can be seen in Appendix D. Images of scenario 7 are shown in figure D.1, images of scenario 25 are shown in figure D.2, images of scenario 37 are shown in figure D.3, images of scenario 43 are shown in figure D.4, images of scenario 49 are shown in figure D.5, images of scenario 55 are shown in figure D.6, images of scenario 61 are shown in figure D.7, images of scenario 67 are shown in figure D.8, images of scenario 73 are shown in figure D.9, images of scenario 79 are shown in figure D.10, images of scenario 85 are shown in figure D.11, images of scenario 103 are shown in figure D.12

In this thesis, through the wall imaging and detecting are applied to walls that have different thickness values. In this thesis, 3 different thickness walls are used through-

Table 4.4: Different wall thickness in 108 scenarios

Wall Thickness	2mm	4mm	6mm
----------------	-----	-----	-----

Table 4.5: Different human size in 108 scenarios

Human Type	Head(Sphere)	Body(Cylinder)
a	Radius with 1cm	Radius with 1cm and Length with 10cm
b	Radius with 1.5cm	Radius with 1.5cm and Length with 10cm
c	Radius with 0.9cm	Radius with 0.9cm and Length with 10cm
d	Radius with 1.1cm	Radius with 1.1cm and Length with 10cm
e	Radius with 1.3cm	Radius with 1.3cm and Length with 10cm

out 108 scenarios. The values of the thickness of walls used throughout 108 scenarios can be seen in table 4.4. As shown in table 4.4, the values of the thickness of walls used throughout 108 scenarios are *2mm*, *4mm*, and *6mm*. Which the values of thickness of wall are used during the 108 scenarios can be seen from tables C.1, C.2, C.3, and C.4 in Appendix C.

In this thesis, as the human model, the combined form of sphere and cylinder is used. A sphere with a certain radius is used as the human head. Cylinder with a certain radius and 10 cm in length is used as a human body. As is known, we all have different physical characteristics as human beings. In this study, this difference is reflected by using spheres and cylinders of the different radius when modeling human. Different types of humans can be seen in table 4.5. The cylinder and sphere used in the human type a have a radius of 1 cm. The cylinder and sphere used in human type b have a radius of 1.5 cm. The cylinder and sphere used in human type c have a radius of 0.9 cm. The cylinder and sphere used in human type d have a radius of 1.1 cm. The cylinder and sphere used in human type e have a radius of 1.3 cm. Which type of human is used during the 108 scenarios can be seen from tables C.1, C.2, C.3, and C.4 in Appendix C.

Position of human and position of object for 108 scenarios can be seen in Appendix B.

4.2 Textural Features / HoG Features SVM Classification for Entropy Based Segmentation Images and Comparison ROC Curves

For the simulated 108 scenarios mentioned above, the entropy-based segmentation and between-class variances are applied. However, as is known, objects (not human) and humans coexist in these 108 scenarios. Object and humans in some scenarios will not be used in the next steps because objects and humans in some scenarios cannot be fully segmented by using entropy-based segmentation and between-class variances. Human could not be fully segmented in scenarios 37, 38, 39, 40, 41, 42, 55, 56, 57, 58, 59, 60, 61, 62, 63, 64, 65, 66, and 88 using entropy-based segmentation. Moreover, object (not human) could not be fully segmented in scenarios 37, 38, 39, 40, 41, 42, 55, 56, 57, 58, 59, 60, 61, 62, 63, 64, 65, 66, 88, 91, 92, 93, 94, 95, and 96 using entropy-based segmentation. Human could not be fully segmented in scenarios 6, 37, 38, 39, 40, 41, 42, 55, 56, 57, 58, 59, 60, 61, 62, 63, 64, 65, and 66 using between-class variances segmentation. Moreover, object (not human) could not be fully segmented in scenarios 19, 20, 21, 22, 37, 38, 39, 40, 41, 42, 55, 56, 57, 58, 59, 60, 61, 62, 63, 64, 65, 66, 88, 91, 92, 93, 94, 95, and 96 using between-class variances segmentation. As a result of entropy-based segmentation, 89 human data and 83 object data can be used for the next steps. As a result of between-class variances segmentation, 89 human data, and 80 object data can be used for the next steps. As can be seen above, entropy-based segmentation causes less data loss than between-class variances segmentation. K-means clustering returns the same result as between-class variances for $K = 2$ so entropy-based segmentation causes less data loss than K-means clustering for $K=2$. Therefore, entropy-based segmentation is used in this study. For these data, textural features, and HoG features in this study are extracted. As it is known, textural features include contrast feature, correlation feature, energy feature, homogeneity feature, inverse difference moment feature, entropy feature, shade feature, and prominence feature. As mentioned in the above chapter, the glcm matrix is obtained for 4 different angles, which are 0^0 , 45^0 , 90^0 , and 135^0 and textural features are obtained from these glcm matrices. In addition, a textural feature vector are obtained from 4 different images, which are the image of the energy sum of the top view of the 3-D data created by combining the B-Scan data, C-Scan image for depth 300, C-Scan image for depth 325, and C-Scan image for depth 350, using a hu-

man or object data. As a result, a textural feature vector contains 128 elements in this study. Moreover, an HoG feature vector includes data obtained from 4 different images mentioned above. How many elements an HoG feature vector contains depends on the parameters used. 9 bins and cells which have 8x8 pixels are used to obtain the HoG feature vector in this study. As a result, an HoG feature vector contains 1440 elements in this study. In this section, for textural features, and HoG features, the SVM algorithm is used for classification. Initially, the best kernel match and optimum parameters are calculated for textural, and HoG features; then the performance metrics of these features are computed by using the pre-determined kernel functions. Initially, 40 human data are selected for the parameter optimization step as members of group 1 and another 40 human data are selected for performance evaluation step as members of group 1. Similarly, 40 object data (not human) are selected for parameter optimization step as members of group 1 and another 40 object data (not human) are selected for performance evaluation step as members of group 1 as shown in figure 4.9. Note that, the selected data for the parameter optimization step and performance evaluation step are different. Then, in this section, by selecting the new data group called group 2 so that the number of data is the same, it will be examined whether the selection of different data will affect the results. Moreover, in this section, the number of selected data will be changed to examine the effect of the selected data number on the performance evaluation. 30 human data are selected for the parameter optimization step and another 30 human data are selected for the performance evaluation step. Similarly, 30 object data (not human) are selected for the parameter optimization step and another 30 object data (not human) are selected for the performance evaluation step as shown in figure 4.10.

The selected data for the parameter optimization step is used to choose the best kernel function with the optimum parameters to achieve the highest performance. In the parameter optimization step, the same dataset is used for textural features, and HoG features to make a comparison. Afterwards, the selected data for performance evaluation step is used to evaluate the performance of textural features, and HoG features. The block diagram of the parameter optimization step and performance evaluation step can be seen in figure 4.11.

SVM is implemented by using "fitsvm" command of MATLAB.

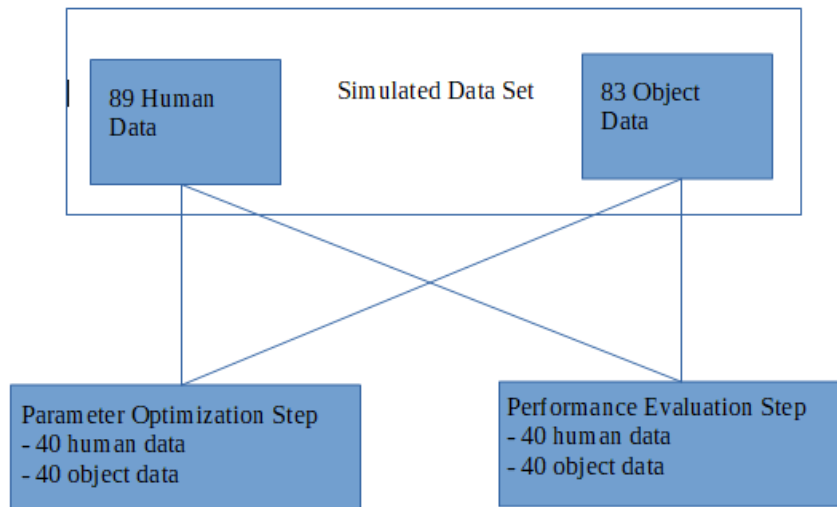


Figure 4.9: Data allocation for parameter optimization and performance evaluation

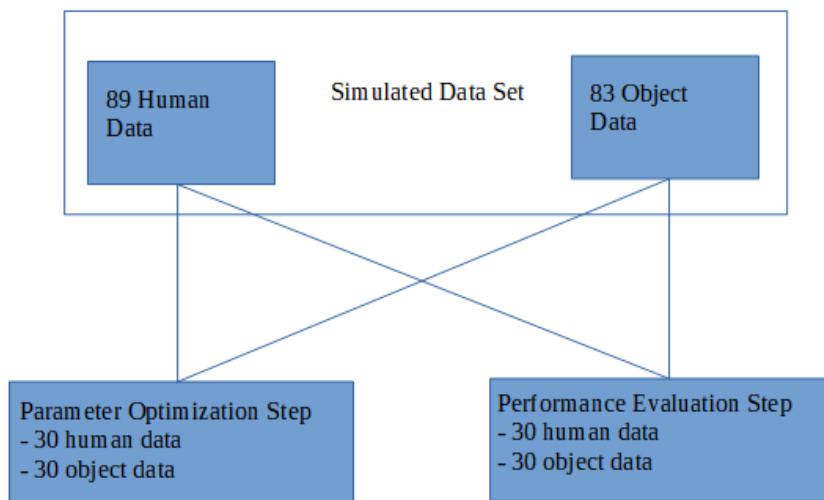


Figure 4.10: Data allocation for parameter optimization and performance evaluation-
2

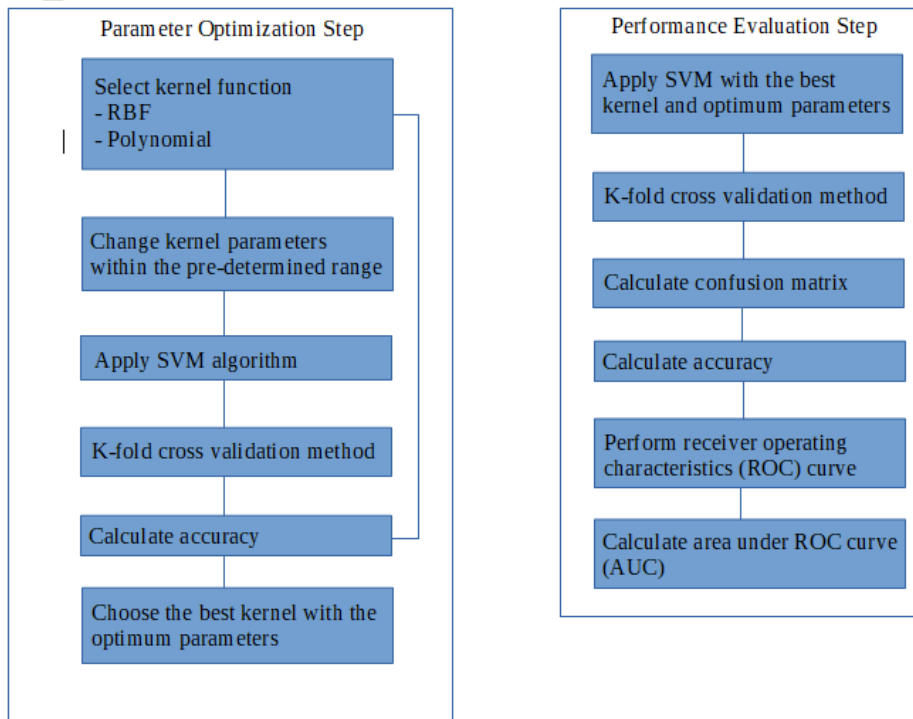


Figure 4.11: Parameter optimization and performance evaluation steps

10-fold cross-validation method is applied to evaluate the performance by using "cross-val" and "kfoldPredict" commands of MATLAB. Then, performance metrics, which are accuracy, receiver operating characteristics(ROC) curve and area under curve (AUC), are found and compared for three different features, which are textural features, and HoG features. ROC curve is obtained by using "perfcurve" command of MATLAB.

4.2.1 Kernel Selection and Parameter Optimization

In this section, as mentioned chapter 3, RBF and polynomial kernel functions are used in this thesis for SVM classification. Parameters of these kernels can be seen in table 3.1. When applying the parameter optimization step, the standard deviation value, which is represented by σ , is changed from 0 to 20. When applying the parameter optimization step, the polynomial degree value, which is represented by d , is changed from 2 to 5. As is known from chapter 3, RBF kernel function is optimized in one-dimensional parameter space, which is σ and polynomial kernel function is optimized

in two-dimensional parameter space, which are σ and d . For all different parameters of these kernels values, accuracies of SVM are found by using RBF and polynomial kernel functions. Accuracy value can be defined as seen from equation 4.1.

$$accuracy = \frac{TP + TN}{TP + FN + TN + FP} \quad (4.1)$$

where TP: True positive(a human is classified correctly - correct detection), TN: True negative(an object(not human) is classified correctly - correct rejection), FN: False negative(a human is classified as an object - miss), FP: False positive(an object is classified as a human - false alarm).

80 feature vector(40 human and 40 object) as member of group 1 are selected for parameter optimization step. In this study, textural features, and HoG features are extracted for these 80 data. Parameter optimization is applied to these textural features, and HoG features in this subsection. 40 human feature vector as member of group 1 for parameter optimization are composed of scenarios 1, 4, 6, 7, 10, 12, 13, 16, 18, 19, 22, 24, 25, 28, 30, 31, 34, 36, 43, 46, 48, 49, 52, 54, 67, 70, 72, 73, 76, 78, 79, 84, 85, 90, 91, 96, 97, 102, 103, and 108. 40 object feature vector as member of group 1 for parameter optimization are composed of scenarios 1, 4, 6, 7, 10, 12, 13, 16, 18, 19, 22, 24, 25, 28, 30, 31, 34, 36, 43, 46, 48, 49, 52, 54, 67, 70, 72, 73, 76, 78, 79, 82, 84, 85, 90, 97, 100, 102, 103, and 108.

Accuracy values of SVM for group 1 textural features by using RBF or Gaussian kernel function for different parameters can be seen in figure 4.12. According to figure 4.12., accuracy of SVM for group 1 textural features is maximum if σ is equal to 2. For this parameter, the accuracy of SVM is 0.75 for textural features.

Accuracy values of SVM for group 1 textural features by using polynomial kernel function for different parameters can be seen in figure 4.13. According to figure 4.13, the accuracy of SVM for group 1 textural features is maximum if σ , which is standard deviation, is equal to 4 and d , which is polynomial degree, is equal to 2. For these parameters, the accuracy of SVM is 0.85 for textural features.

Accuracy values of SVM for group 1 textural features by using polynomial and RBF kernel functions for different parameters are calculated. Results of kernel functions

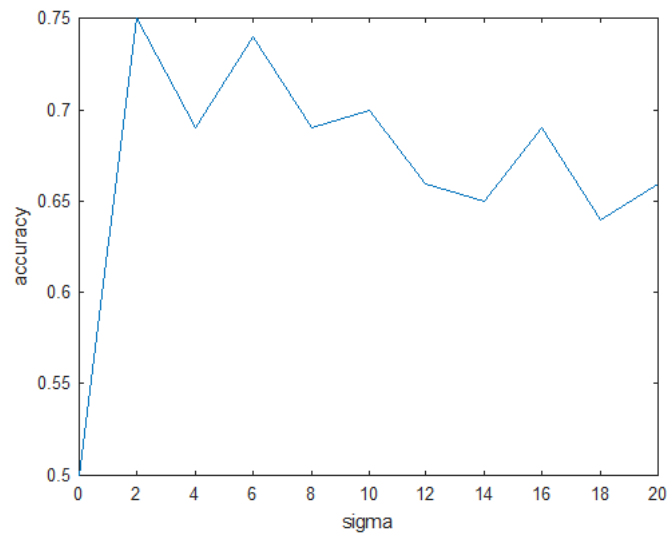


Figure 4.12: Accuracy values of SVM for group 1 textural features by using RBF kernel

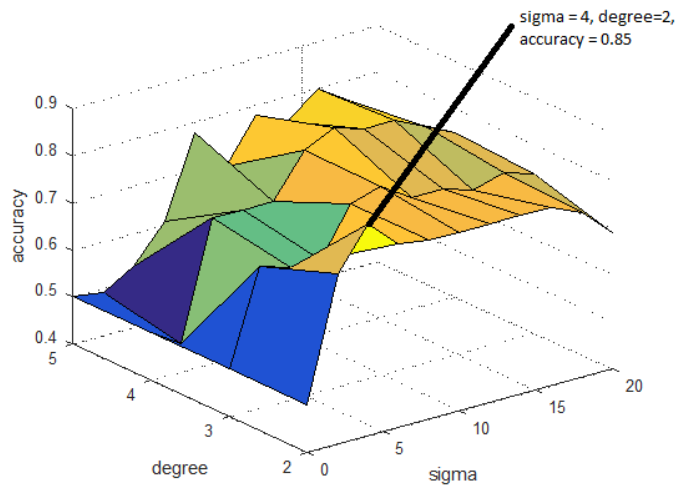


Figure 4.13: Accuracy values of SVM for group 1 textural features by using polynomial kernel

Table 4.6: Accuracy of SVM for group 1 textural features by using different kernels

Kernel	Optimum Parameters	Accuracy
RBF or Gaussian	Sigma = 2	0.75
Polynomial	Sigma = 4, and degree = 2	0.85

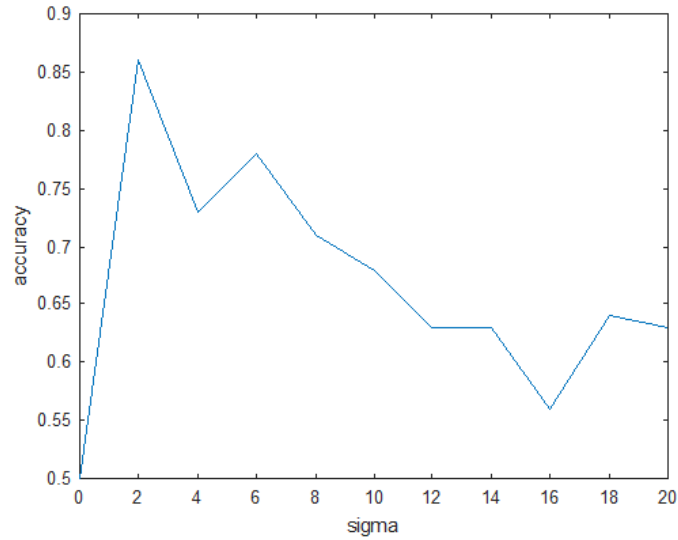


Figure 4.14: Accuracy values of SVM for group 1 HoG features by using RBF kernel

and optimum parameters are given in table 4.6.

Accuracy values of SVM for group 1 HoG features by using RBF or Gaussian kernel function for different parameters can be seen in figure 4.14. According to figure 4.14., accuracy of SVM for group 1 HoG features is maximum if σ is equal to 2. For this parameter, the accuracy of SVM is 0.86 for HoG features.

Accuracy values of SVM for group 1 HoG features by using polynomial kernel function for different parameters can be seen in figure 4.15. According to figure 4.15, the accuracy of SVM for group 1 HoG features is maximum if σ , which is standard deviation, is equal to 4 and d , which is polynomial degree, is equal to 5. For these parameters, the accuracy of SVM is 0.91 for HoG features.

Accuracy values of SVM for group 1 HoG features by using polynomial and RBF kernel functions for different parameters are calculated. Results of kernel functions

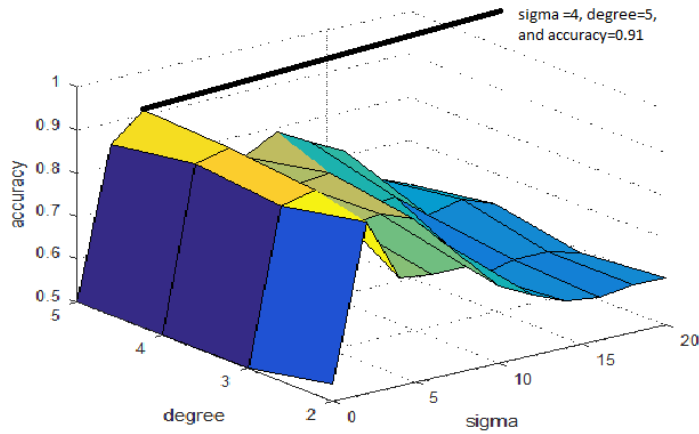


Figure 4.15: Accuracy values of SVM for group 1 HoG features by using polynomial kernel

Table 4.7: Accuracy of SVM for group 1 HoG features by using different kernels

Kernel	Optimum Parameters	Accuracy
RBF or Gaussian	Sigma = 2	0.86
Polynomial	Sigma = 4, and degree = 5	0.91

and optimum parameters are given in table 4.7.

According to the accuracy values given in tables 4.6, and 4.7, polynomial kernel functions gives the best accuracy for all feature types. The optimum parameters for textural features are $\sigma = 4$ and $degree = 2$. The optimum parameters for HoG features are $\sigma = 4$ and $degree = 5$. Polynomial kernels with these optimum parameter values will be used in performance evaluation calculations. However, since the RBF kernel is bound to a parameter, it is computationally more efficient than polynomial kernels.

For parameter optimization, let's select different feature vector groups for human and object and repeat the above operations. The objective is to determine whether the selected feature vector groups will have an effect on the performance results. 40 human feature vectors as member of group 2 for parameter optimization are composed of scenarios 1, 2, 3, 7, 8, 9, 13, 14, 15, 19, 20, 21, 25, 26, 27, 31, 32, 33, 43, 44, 45, 49,

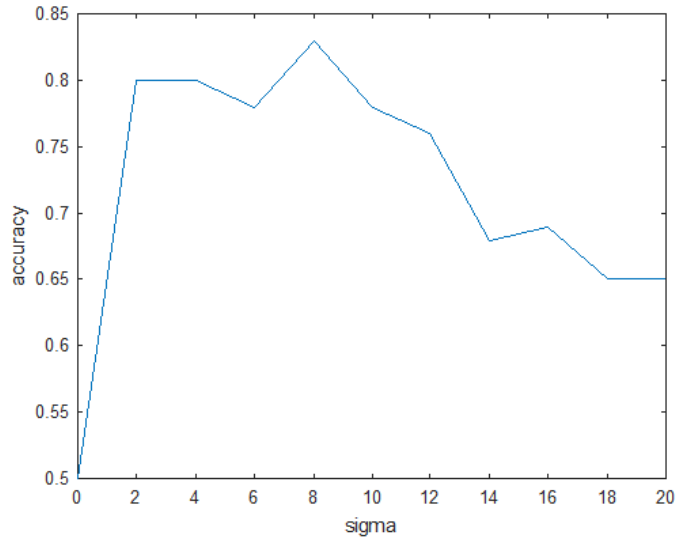


Figure 4.16: Accuracy values of SVM for group 2 textural features by using RBF kernel

50, 51, 67, 68, 69, 73, 74, 75, 79, 80, 85, 86, 91, 92, 97, 98, 103, and 104. 40 object feature vectors as member of group 2 for parameter optimization are composed of scenarios 1, 2, 3, 7, 8, 9, 13, 14, 15, 19, 20, 21, 25, 26, 27, 31, 32, 33, 43, 44, 45, 49, 50, 51, 67, 68, 69, 73, 74, 75, 79, 80, 81, 85, 86, 87, 97, 98, 103, and 104.

Accuracy values of SVM for group 2 textural features by using RBF or Gaussian kernel function for different parameters can be seen in figure 4.16. According to figure 4.16., accuracy of SVM for group 2 textural features is maximum if σ is equal to 8. For this parameter, the accuracy of SVM is 0.83 for textural features.

Accuracy values of SVM for group 2 textural features by using polynomial kernel function for different parameters can be seen in figure 4.17. According to figure 4.17, the accuracy of SVM for group 2 textural features is maximum if σ , which is standard deviation, is equal to 2 and d , which is polynomial degree, is equal to 2. For these parameters, the accuracy of SVM is 0.91 for textural features.

Accuracy values of SVM for group 2 textural features by using polynomial and RBF kernel functions for different parameters are calculated. Results of kernel functions and optimum parameters are given in table 4.8.

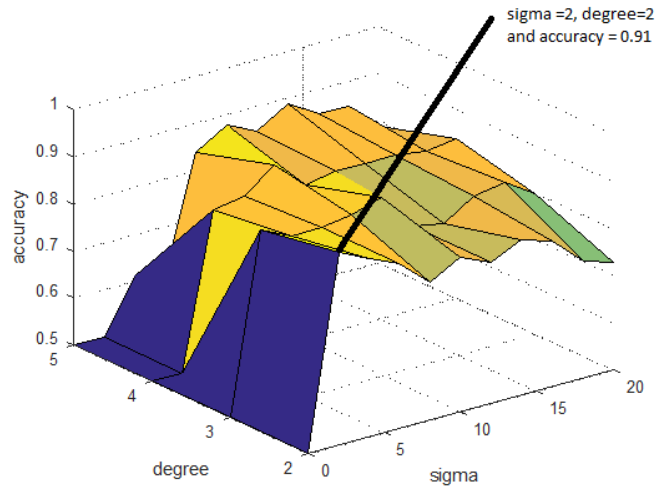


Figure 4.17: Accuracy values of SVM for group 2 textural features by using polynomial kernel

Table 4.8: Accuracy of SVM for group 2 textural features by using different kernels

Kernel	Optimum Parameters	Accuracy
RBF or Gaussian	Sigma = 8	0.83
Polynomial	Sigma = 2, and degree = 2	0.91

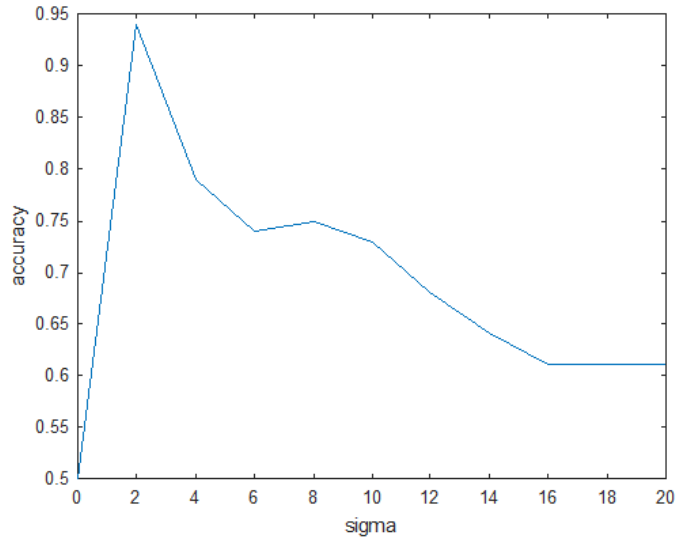


Figure 4.18: Accuracy values of SVM for group 2 HoG features by using RBF kernel

Table 4.9: Accuracy of SVM for group 2 HoG features by using different kernels

Kernel	Optimum Parameters	Accuracy
RBF or Gaussian	Sigma = 2	0.94
Polynomial	Sigma = 4, and degree = 4	0.99

Accuracy values of SVM for group 2 HoG features by using RBF or Gaussian kernel function for different parameters can be seen in figure 4.18. According to figure 4.18., accuracy of SVM for group 2 HoG features is maximum if σ is equal to 2. For this parameter, the accuracy of SVM is 0.94 for HoG features.

Accuracy values of SVM for group 2 HoG features by using polynomial kernel function for different parameters can be seen in figure 4.19. According to figure 4.19, the accuracy of SVM for group 2 HoG features is maximum if σ , which is standard deviation, is equal to 4 and d , which is polynomial degree, is equal to 4. For these parameters, the accuracy of SVM is 0.99 for HoG features.

Accuracy values of SVM for group 2 HoG features by using polynomial and RBF kernel functions for different parameters are calculated. Results of kernel functions and optimum parameters are given in table 4.9.

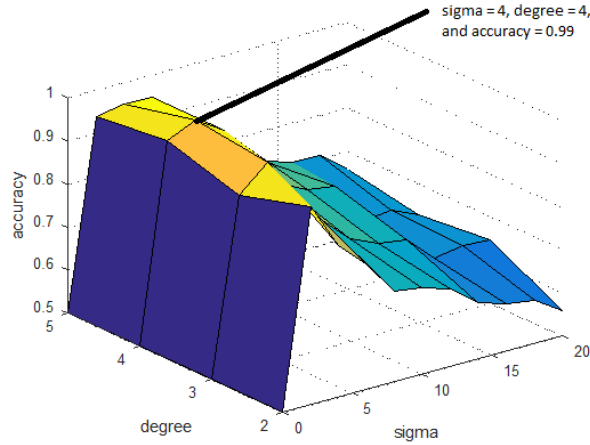


Figure 4.19: Accuracy values of SVM for group 2 HoG features by using polynomial kernel

According to the accuracy values given in tables 4.8, and 4.9, polynomial kernel functions gives the best accuracy for all feature types. The optimum parameters for textural features are $\sigma = 2$ and $degree = 2$. The optimum parameters for HoG features are $\sigma = 4$ and $degree = 4$. Polynomial kernels with these optimum parameter values will be used in performance evaluation calculations. When the difference between the two groups is examined, polynomial kernel functions with different optimum parameters give the best accuracy for both groups. However, the accuracy values of group 2 are higher in the parameter optimization step than group 1. It is not right to say something without looking at the Performance evaluation step. However, it is a fact that the selection of the feature vector group is an important factor affecting the result. In the parameter optimization step, the feature vector group should be selected to cover all cases as much as possible.

Finally, in this study, 30 human data and 30 object data are chosen for parameter optimization step and 30 human data and 30 object data are chosen for performance evaluation step. The objective is to determine whether the number of selected data will have an effect on the performance evaluation results. 30 human feature vectors are composed of scenarios 1, 6, 7, 12, 13, 18, 19, 24, 25, 30, 31, 36, 43, 48, 49, 54, 67, 72, 73, 78, 79, 84, 85, 90, 91, 96, 97, 102, 103, and 108. 30 object feature vectors are composed of scenarios 1, 3, 6, 7, 9, 12, 13, 18, 19, 24, 25, 30, 31, 36, 43, 48, 49, 54, 67, 72, 73, 78, 79, 84, 85, 90, 97, 102, 103, and 108.

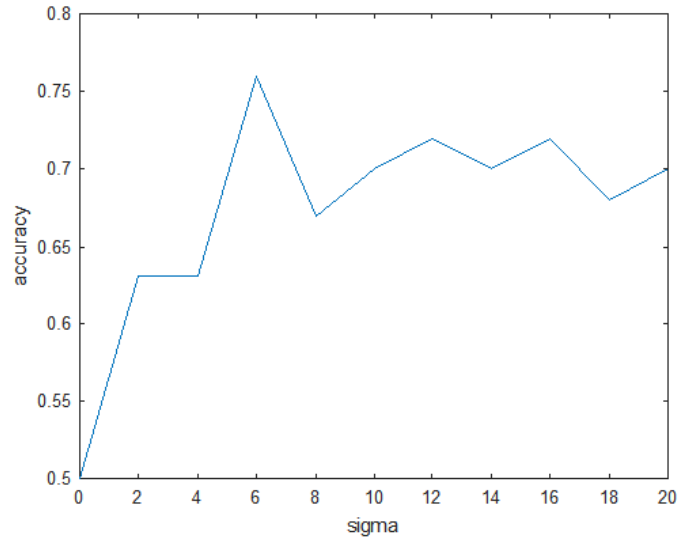


Figure 4.20: Accuracy values of SVM with 30 human and 30 object data for textural features by using RBF kernel

Accuracy values of SVM for textural features by using RBF or Gaussian kernel function for different parameters can be seen in figure 4.20. According to figure 4.20., accuracy of SVM for textural features is maximum if σ is equal to 6. For this parameter, the accuracy of SVM is 0.76 for textural features.

Accuracy values of SVM for textural features by using polynomial kernel function for different parameters can be seen in figure 4.21. According to figure 4.21, the accuracy of SVM for textural features is maximum if σ , which is standard deviation, is equal to 12 and d , which is polynomial degree, is equal to 2. For these parameters, the accuracy of SVM is 0.78 for textural features.

Accuracy values of SVM for textural features by using polynomial and RBF kernel functions for different parameters are calculated. Results of kernel functions and optimum parameters are given in table 4.10.

Accuracy values of SVM for HoG features by using RBF or Gaussian kernel function for different parameters can be seen in figure 4.22. According to figure 4.22., accuracy of SVM for HoG features is maximum if σ is equal to 2. For this parameter, the accuracy of SVM is 0.77 for HoG features.

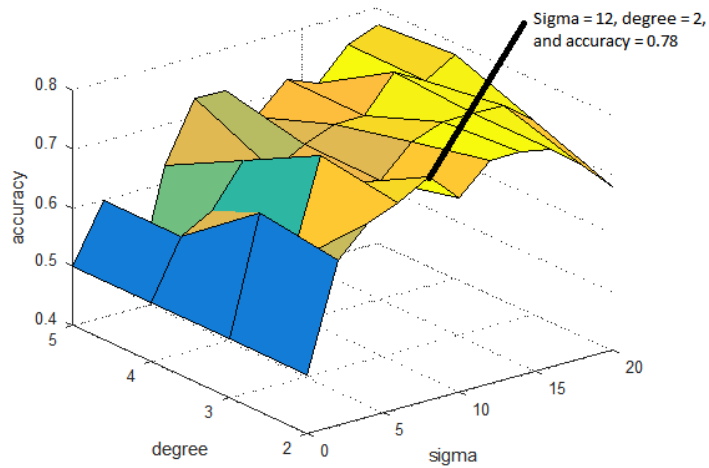


Figure 4.21: Accuracy values of SVM with 30 human and 30 object data for textural features by using polynomial kernel

Table 4.10: Accuracy of SVM with 30 object and 30 human data for textural features by using different kernels

Kernel	Optimum Parameters	Accuracy
RBF or Gaussian	Sigma = 6	0.76
Polynomial	Sigma = 12, and degree = 2	0.78

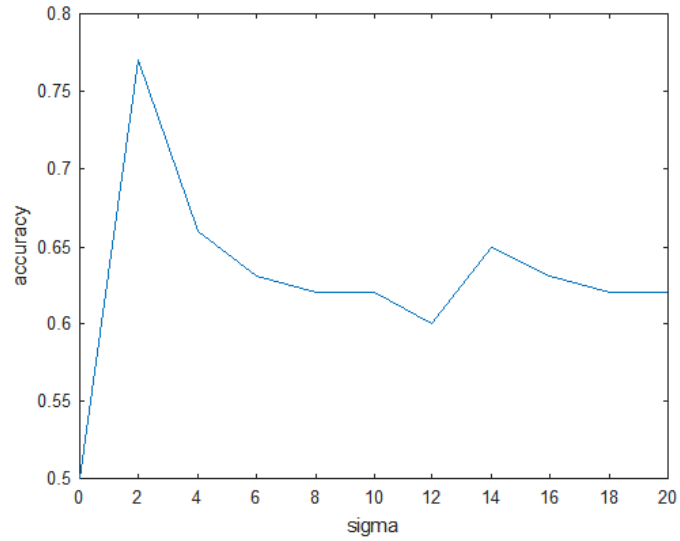


Figure 4.22: Accuracy values of SVM with 30 human and 30 object data for HoG features by using RBF kernel

Table 4.11: Accuracy of SVM with 30 object and 30 human data for HoG features by using different kernels

Kernel	Optimum Parameter	Accuracy
RBF or Gaussian	Sigma = 2	0.77
Polynomial	Sigma = 2, and degree = 2	0.80

Accuracy values of SVM for HoG features by using polynomial kernel function for different parameters can be seen in figure 4.23. According to figure 4.23, the accuracy of SVM for HoG features is maximum if σ , which is standard deviation, is equal to 2 and d , which is polynomial degree, is equal to 2. For these parameters, the accuracy of SVM is 0.80 for HoG features.

Accuracy values of SVM for HoG features by using polynomial and RBF kernel functions for different parameters are calculated. Results of kernel functions and optimum parameters are given in table 4.11.

According to the accuracy values given in tables 4.10, and 4.11, polynomial kernel functions gives the best accuracy for all feature types. The optimum parameters for textural features are $\sigma = 12$ and $degree = 2$. The optimum parameters for HoG

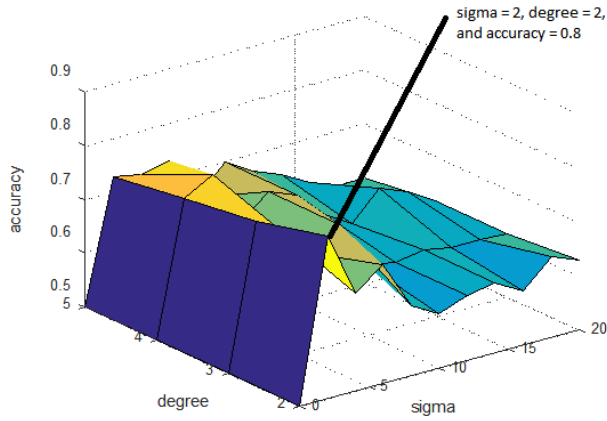


Figure 4.23: Accuracy values of SVM with 30 human and 30 object data for HoG features by using polynomial kernel

features are $\sigma = 2$ and $degree = 2$. Polynomial kernels with these optimum parameter values will be used in performance evaluation calculations. As shown in tables 4.8, 4.9, 4.10, and 4.11, accuracy values decrease as the number of data selected for parameter optimization decreases. However, the polynomial kernel give also the best accuracy, albeit with different optimum parameters.

4.2.2 Performance Evaluation

Firstly, in this subsection, the textural features, and HoG features of 40 human and 40 object data which are belonging to group 1 selected for the performance evaluation step are classified by SVM with polynomial kernel and the optimum parameters found in parameter optimization step. Then, the textural features, and HoG features of 40 human and 40 object data which are belonging to group 2 selected for the performance evaluation step are classified by SVM with polynomial kernel and the optimum parameters found in parameter optimization step. Finally, the textural features, and HoG features of 30 human and 30 object data selected for the performance evaluation step are classified by SVM with polynomial kernel and the optimum parameters found in parameter optimization step. After, 10-fold cross-validation method is applied to all classifications for obtaining the performance of textural, and HoG features. For performance evaluation, accuracy, receiver operating characteristics(ROC), and area

Table 4.12: Type of feature vectors, kernel and optimum parameters for all different datasets

Dataset	Type of feature vectors	Kernel	Optimum parameters
40 human and 40 object data	Textural	Polynomial	$\text{Sigma} = 4, d = 2$
40 human and 40 object data	HoG	Polynomial	$\text{Sigma} = 4, d = 5$
40 human and 40 object data group 2	Textural	Polynomial	$\text{Sigma} = 2, d = 2$
40 human and 40 object data group 2	HoG	Polynomial	$\text{Sigma} = 4, d = 4$
30 human and 30 object data	Textural	Polynomial	$\text{Sigma} = 12, d = 2$
30 human and 30 object data	HoG	Polynomial	$\text{Sigma} = 2, d = 2$

Table 4.13: Confusion matrices and accuracy values of SVM for group 1 textural, and HoG features by using polynomial kernel and optimum parameters

	Textural Features		HoG Features	
Confusion Matrix	TP 33	FP 3	TP 39	FP 3
	FN 7	TN 37	FN 1	TN 37
Accuracy	0.88		0.95	

under curve(AUC), and the confusion matrices are calculated. The type of the kernel function and the values of optimum parameters to be used for SVM classification of the selected dataset are given in the table 4.12.

40 human feature vector as member of group 1 for performance evaluation are composed of scenarios 2, 3, 5, 8, 9, 11, 14, 15, 17, 20, 21, 23, 26, 27, 29, 32, 33, 35, 44, 45, 47, 50, 51, 53, 68, 69, 71, 74, 75, 77, 80, 83, 86, 89, 92, 95, 98, 101, 104, and 107. 40 object feature vector as member of group 1 for performance evaluation are composed of scenarios 2, 3, 5, 8, 9, 11, 14, 15, 17, 20, 21, 23, 26, 27, 29, 32, 33, 35, 44, 45, 47, 50, 51, 53, 68, 69, 71, 74, 75, 77, 80, 81, 83, 86, 89, 98, 99, 101, 104, and 107. Confusion matrices and the accuracy values for group 1 are given in table 4.13.

ROC curves of group 1 textural, and HoG features can be seen in figure 4.24.

The AUC value of textural features of group 1 is 0.9769. The AUC value of HoG features of group 1 is 0.9969. According to accuracy values, ROC curves and the areas under these curves (AUC values), HoG features for group 1 in this study has

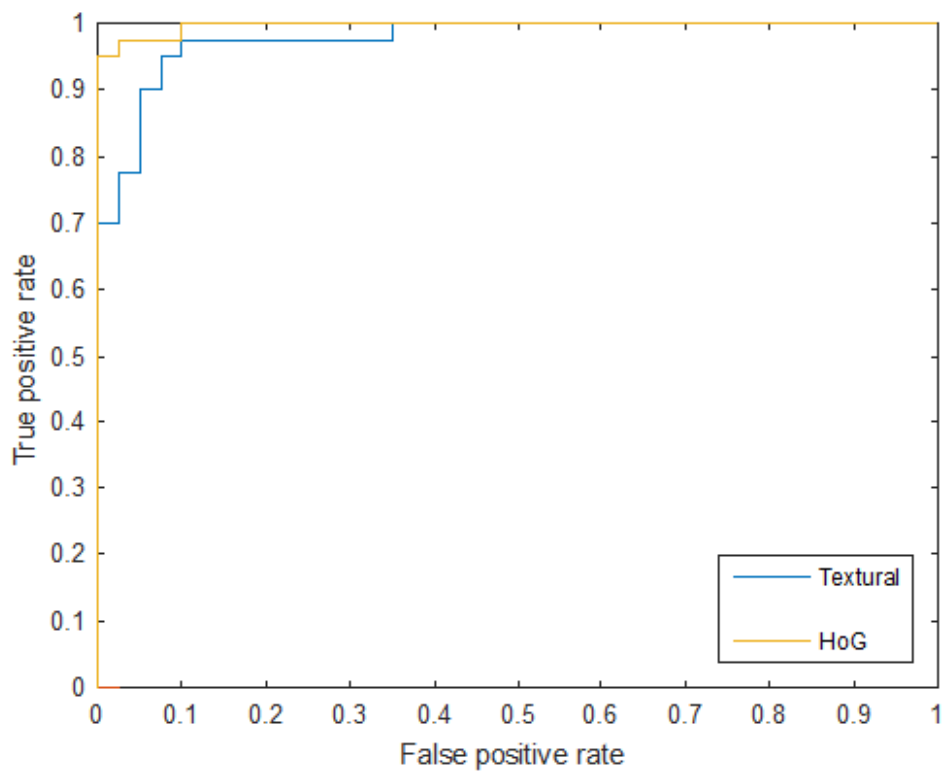


Figure 4.24: ROC curves of the textural features/ HoG features of group 1

Table 4.14: Confusion matrices and accuracy values of SVM for group 2 textural, and HoG features by using polynomial kernel and optimum parameters

	Textural Features		HoG Features	
Confusion Matrix	TP 35	FP 5	TP 38	FP 4
	FN 5	TN 35	FN 2	TN 36
Accuracy	0.88		0.93	

higher discrimination performance than textural features.

40 human feature vectors as member of group 2 for performance evaluation are composed of scenarios 4, 5, 6, 10, 11, 12, 16, 17, 18, 22, 23, 24, 28, 29, 30, 34, 35, 36, 46, 47, 48, 52, 53, 54, 70, 71, 72, 76, 77, 78, 82, 83, 89, 90, 94, 95, 100, 101, 106, 107. 40 object feature vectors as member of group 2 for performance evaluation are composed of scenarios 4, 5, 6, 10, 11, 12, 16, 17, 18, 22, 23, 24, 28, 29, 30, 34, 35, 36, 46, 47, 48, 50, 51, 52, 70, 71, 72, 76, 77, 78, 82, 83, 84, 89, 90, 91, 100, 101, 106, and 107. Confusion matrices and the accuracy values for group 2 are given in table 4.14.

ROC curves of group 2 textural, and HoG features can be seen in figure 4.25.

The AUC value of textural features of group 2 is 0.9388. The AUC value of HoG features of group 2 is 0.94. According to accuracy values, ROC curves and the areas under these curves (AUC values), HoG features for group 2 in this study has higher discrimination performance than textural features. As a result, HoG features for both group 1 and group 2 has higher discrimination performance than other features. In addition, although the polynomial kernel is used with different optimum parameter values in both groups, the results for HoG features and textural features are satisfactory. For the performance evaluation step, HoG features of group 1 give better results than HoG features of group 2. The choice of data groups to be used in parameter optimization and performance evaluation steps is important for the results.

30 human feature vectors for performance evaluation are composed of scenarios 2, 5, 8, 11, 14, 17, 20, 23, 26, 29, 32, 35, 44, 47, 50, 53, 68, 71, 74, 77, 80, 83, 86, 89, 92, 95, 98, 101, 104, and 107. 30 object feature vectors are composed of scenarios 2, 4,

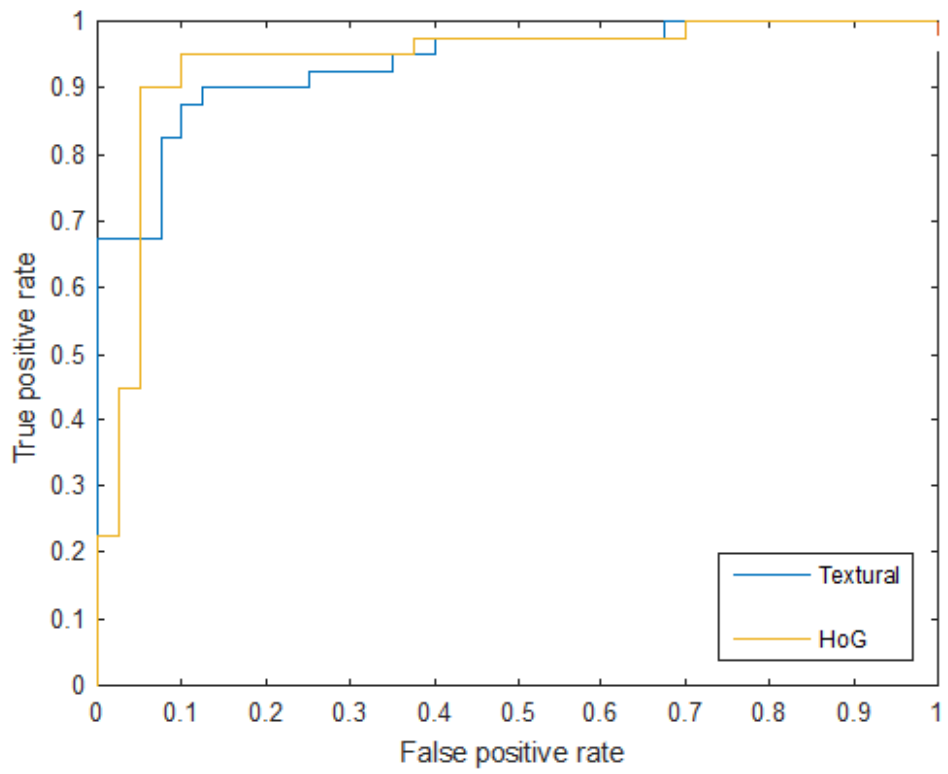


Figure 4.25: ROC curves of the textural features/ HoG features of group 2

Table 4.15: Confusion matrices and accuracy values of SVM for textural, and HoG features of 30 human and 30 object data by using polynomial kernel and optimum parameters

	Textural Features		HoG Features	
Confusion Matrix	TP 27	FP 10	TP 25	FP 3
	FN 3	TN 20	FN 5	TN 27
Accuracy	0.78		0.87	

5, 8, 10, 11, 14, 17, 20, 23, 26, 29, 32, 35, 44, 47, 50, 53, 68, 71, 74, 77, 80, 83, 86, 89, 98, 101, 104, and 107. Confusion matrices and the accuracy values for 30 object and 30 human data are given in table 4.15.

ROC curves of textural, and HoG features of 30 human and 30 object data can be seen in figure 4.26.

AUC value of textural features of 30 object and 30 human data is 0.8733. AUC value of HoG features of 30 object and 30 human data is 0.93. According to accuracy values, ROC curves and the areas under these curves (AUC values), HoG features for 30 object and 30 human data in this study has higher discrimination performance than textural features. As shown in the above studies, when the number of data used decreases, classification performance decreases.

4.2.3 Comparison of Accuracy of Textural Features

In subsection 4.2.2, performance of the textural features is given. As is known, in this study, textural features contain contrast, correlation, energy, homogeneity, inverse difference moment, entropy, shade, and prominence features. In this subsection, the accuracy values of contrast, correlation, energy, homogeneity, inverse difference moment, entropy, shade, and prominence features are computed separately and the success of each individual feature is clarified.

As is known, during this study, 108 human and 108 object data are simulated. By using the entropy-based segmentation technique, 89 human and 83 object data are

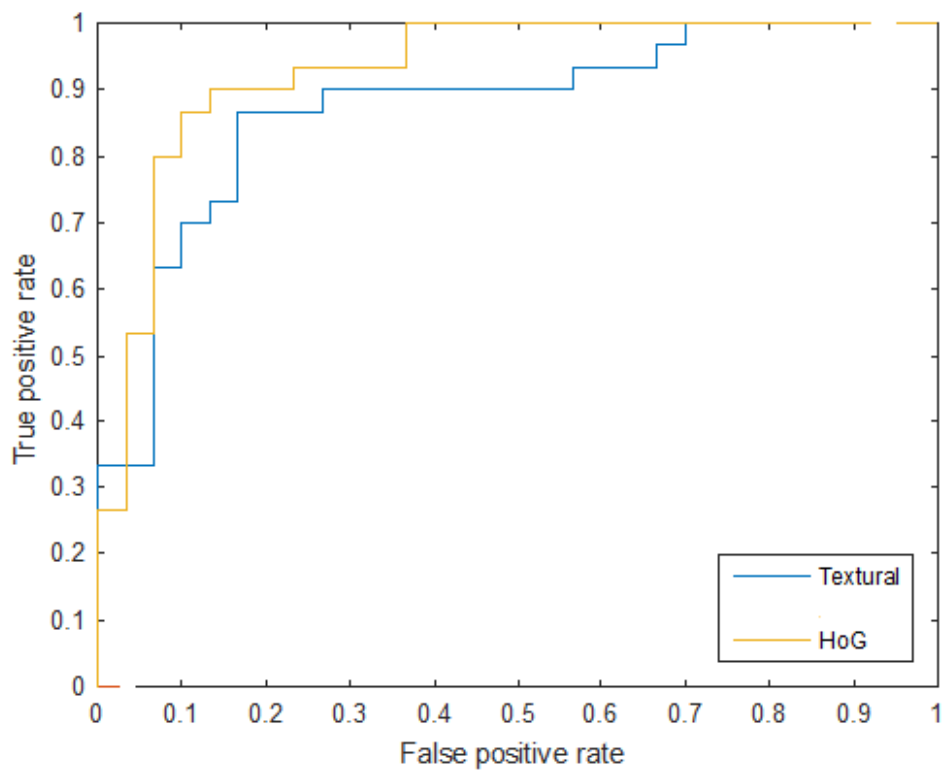


Figure 4.26: ROC curves of the textural features/ HoG features of 30 object and 30 human data

obtained. As mentioned in subsections 4.2.1, and 4.2.2, simulated data is divided into two different sets. 40 human data and 40 object data are chosen for parameter optimization. 40 human data and 40 object data are chosen for performance optimization. In this subsection, the dataset of performance evaluation of group 2 is used. 40 object and 40 human data are classified by SVM with the polynomial kernel and optimum parameters for the textural features and its elements.

In subsection 4.2.2, the accuracy of the textural features of group 2 for the data set of performance evaluation step is 0.88. For the same data set, accuracy of the contrast feature is 0.79, accuracy of the correlation feature is 0.83, accuracy of the energy feature is 0.51, accuracy of the homogeneity feature is 0.64, accuracy of the inverse difference moment feature is 0.60, accuracy of the entropy feature is 0.55, accuracy of the shade feature is 0.65, accuracy of the prominence feature is 0.65. As can be seen from the accuracy values given above, contrast and correlation features give the most satisfactory results. Therefore, contrast and correlation features give around 0.85 accuracy together. Moreover, contrast, correlation, energy, and homogeneity features give around 0.86 accuracy together.

4.3 Comparison of This Study and Reference Paper

Before starting these studies, paper [92] is taken as a reference and is examined in detail. In paper [92], textural feature-based target detection is applied in through-the-wall radar imagery. In this thesis, the textural feature-based target detection is also examined. However, there are several differences between this thesis and reference paper [92]. First of all, in this thesis, the GPR system is used to obtain simulations. Hertzian dipoles are used as receiver and transmitter antennas of the GPR system. The transmitter antenna transmits the gaussian pulse at 1.5GHz to capture images. In reference to paper [92], the UWB MIMO radar system developed by DRDC is used to obtain real images. The MIMO radar contains two transmit antennas and an eight-element receive array. Compact Y-shaped printed bowtie antennas which have approximately 60° beamwidth in elevation and 150° beamwidth in azimuth are used as receiver and transmitter antennas of UWB MIMO radar system. The transmitter antennas transmit a frequency-modulated continuous-wave(FMCW) signal covering

the 0.8 to 2.7 GHz frequency band to capture images. When the antennas and radar systems used are examined, the images obtained in paper [92] are of higher quality than images obtained in this thesis. Furthermore, the images obtained in paper [92] are real data, while the images obtained in this thesis are the result of the simulation.

Secondly, in this thesis, 40 human and 40 object data are used as the training dataset. 40 human and 40 object data are used as test dataset. In the reference paper, 20 human and 20 clutter data are used as the training dataset. However, the number of humans and the clutter of the test dataset is not specified. As a result, the number of data used in the referenced paper is smaller than the number of data used in this thesis. As it is known, the higher the number of data, the more realistic results will be obtained. Moreover, as can be seen from the reference paper, the results were tried to be obtained in a scenario. The location of the people, wall thickness, wall type, etc. have not been changed. This compromises the reliability of the results.

Finally, in both studies, entropy-based segmentation is used in the segmentation stage and feature vectors are extracted from images by using GLCM. In reference to the paper, feature vectors contain contrast, correlation, energy, and homogeneity features and consist of 16 elements. In this thesis, feature vectors contain contrast, correlation, energy, homogeneity, inverse difference moment, entropy, shade and prominence features and consist of 128 elements. As is known from subsection 4.2.3, If the feature type in the feature vector is increased, the accuracy value increases. In the reference paper, Mahalanobis distance metrics are used for the classification step, while SVM is used for the classification step in this thesis. Furthermore, there is little information about performance evaluation in the reference paper.

CHAPTER 5

CONCLUSION

This study proposes an algorithm to detect and classify humans in through-the-wall imaging. After simulating 108 scenarios, including human and object, entropy-based segmentation and between-class variances segmentation are applied to the obtained images of the energy sum of the top view of the 3-D data created by combining the B-Scan data. Since data loss is less in entropy-based segmentation, entropy-based segmentation is used in the segmentation stage of this study. Image of the energy sum of the top view of the 3-D data created by combining the B-Scan data, C-Scan image for depth 300, C-Scan image for depth 325, and C-Scan image for depth 350 are masked with masks obtained as a result of entropy-based segmentation. Next, textural feature vectors, and HoG feature vectors are obtained from these images. Finally, these feature vectors are classified by SVM. Results show that the HoG features in this study increase discrimination performance when compared to textural. HoG features provide satisfactory results as it provides information on how and to what extent changes in the object or human occur. Moreover, since textural properties are distinctive in humans and objects, satisfactory results are obtained from textural features and it is found to be suitable for this study.

In this study, as the number of data used for classification increases, accuracy has been observed to increase. To obtain more realistic results, the number of data used should be higher. Moreover, the importance of the dataset chosen for training and test is also shown in this study. For the results to be realistic, the selected dataset must be inclusive of the scenarios created.

In the future, this study should be tested on real human and object data set. Also, more realistic results as seen in E.1 should be obtained by using more simulation data.

Moreover, different algorithms can be used in the classification, feature extraction, and segmentation stages.

REFERENCES

- [1] *I. M. Aftanas*, “Through Wall Imaging with UWB Radar System ” Technical University of Kosice, 2009.
- [2] *ADIB, F., AND KATABI, D.*, 2013. See through walls with Wi-Fi! In ACM SIGCOMM.
- [3] *Yang, Y.*, “Development of a Real-time Ultra-wideband See Through Wall Imaging Radar System.” PhD diss., University of Tennessee, 2008.
- [4] *Amin, M.*, [Through the Wall Radar Imaging], CRC Press, Boca Raton, (2010).
- [5] *Amin, M. G. and Ahmad, F.*, “Wideband synthetic aperture beamforming for through-the-wall imaging,” *IEEE Signal Process. Mag.* 25(4), 110–113 (2008).
- [6] *M. Dehmollaian, M. Thiel, and K. Sarabandi*, “Through-the-Wall Imaging Using Differential SAR, ” *IEEE Transactions on Geoscience and Remote Sensing*, vol. 47, pp. 1289–1296, May 2009.
- [7] *E. Ertin and R. L. Moses*, “Through-the-Wall SAR Attributed Scattering Center Feature Estimation, ” *IEEE Transaction On Geoscience and Remote Sensing*, vol. 47, no. 5, pp. 1338-1348, May 2009.
- [8] *S.E. Borek*, “An overview of through the wall surveillance for homeland security,” in *Proc. 34th Applied Imagery and Pattern Recognition Workshop*, Oct.2005.
- [9] *A. Genc*, “Multi-Feature Fusion For GPR-Based Landmine Detection and Classification,” retrieved from Middle East Technical University, (2019).
- [10] *D., Mesut, and T. S., Gonul*, “Through-the-wall target detection using gpr A-Scan data: Effects of different wall structures on detection performance”, 2017.

- [11] *M. Farwell, J. Ross, R. Luttrell, D. Cohen, W. Chin, T. Dogaru*, “U.S. Army sense through the wall system development and design considerations,” *J. Franklin Inst.*, vol. 345, no. 6, July 2008.
- [12] *E. Ertin and R. Moses*, “Through-the-wall SAR attributed scattering center feature estimations,” in *Proc. 2008 IEEE Int. Conf. Acoustics, Speech, and Signal Processing*, Apr. 2008, pp. 5177–5180.
- [13] *A. Lin and H. Ling*, “Through-wall measurements of a Doppler and direction-of-arrival (DDOA) radar for tracking indoor movers,” in *Proc. 2005 IEEE APS Int. Symp.*, July 2005, vol. 3B, pp. 322–325.
- [14] *R.M. Narayanan*, “Through wall radar imaging using UWB noise waveforms,” *J. Franklin Inst.*, vol. 345, no. 6, July 2008.
- [15] *P. Withington, H. Fluhler, and S. Nag*, “Enhancing homeland security with advanced UWB sensors,” *IEEE Microwave Mag.*, vol. 4, no. 3, pp. 51–58, 2003.
- [16] *A. H. Muqaibel, A. Safaai-Jazi, A. Bayram, A. M. Attiya, and S. M. Riad*, Ultrawideband. through-the-wall propagation, *IEE Proceedings on Microwave Antennas Propagation*, 152(6), 581–588, December 2005.
- [17] *I. Cuinas and M. G. Sanchez*, Measuring, modeling, and characterizing of indoor radio channel at 5.8 GHz, *IEEE Transactions on Vehicular Technology*, 50(2), 526–535, March 2001.
- [18] *P. Jaturatussanai, M. Chamchoy, and S. Promwong*, Characteristics of UWB propagation through building materials, in *Proceedings of the International Symposium on Communications and Information Technology*, vol 1, Beijing, China, October 2005.
- [19] *G. Tesserault, N. Malhouroux, and P. Pajusco*, Multi-frequencies characterization of buildings materials: Angular and polarization analysis, in *The Second European Conference on Antennas and Propagation (EuCAP)*, pp. 1–5, Edinburgh, U.K., November 2007.

- [20] *D. Pena, R. Feick, H. D. Hristov, and W. Grote*, Measurement and modelling of propagation losses in brick and concrete walls for the 900-MHz Band, *IEEE Transactions on Antennas and Propagation*, 51(1), 31–39, January 2003.
- [21] *F. Sagnard and G. El Zein*, In Situ characterization of building materials for propagation modeling: Frequency and time responses, *IEEE Transactions on Antennas and Propagation*, 53(10), 3166–3173, October 2005.
- [22] *Y. Yang and A. Fathy*, Development and Implementation of a Real-Time See-Through-Wall Radar System Based on FPGA, *IEEE Transactions on Geoscience and Remote Sensing*, 2008, Submitted and under revision.
- [23] *Setlur, P., Amin, M. and Ahmad, F.*, “Indoor Imaging of targets enduring simple harmonic motion using Doppler radars,” *Proc. Int. Symp. Signal Process. Information Tech.*, Athens, Greece, December 2005.
- [24] *Stimson, G. W.*, “Introduction to Airborne”, Chapter 1 (13pp).
- [25] *Ramakrishnan, S., Demarcus, V., Ny, J. L., Patwari, N., Gussy, J.*, “Synthetic Aperture Radar Imaging Using Spectral Estimation Techniques.”, University of Michigan.
- [26] *DJ, D.*, “Ground Penetrating Radar (2nd ed.)”, Knoval (Institution of Engineering and Technology). pp. 1–4.
- [27] *Ferris Jr., D. D., Currie, N. C.*, “A Survey of Current Technologies for Through-The-Wall Surveillance (TWS),” *Proc. SPIE*, vol. 3577, pp. 62-72, 1998.
- [28] *Falconer, D. G., Steadman, K. N., Watters, D. G.*, “Through-the-Wall Differential Radar,” *Proc. SPIE*, vol. 2938, pp. 147-151, November 1996.
- [29] *Kirscht, Martin, and Rinke, C.*, “3D Reconstruction of Buildings and Vegetation from Synthetic Aperture Radar (SAR) Images.” MVA. 1998.
- [30] *Safaai-Jazi A., Riad S. M., Muqaibel A. and Bayram, A.*, “Ultra-wideband. propagation.measurements.and.channel.modeling” .Technical.Report.,Bradley. De-

partment.of.Electrical.Engineering,.Virginia.Polytechnic.Institute.and.State.
University,.Blacksburg,.VA,.November.2002.

- [31] *Komanduri V. R., A. Hoorfar, and N. Engheta*, “Wideband printed antenna elements for through-wall microwave imaging applications, ” Proceedings of 2004 IEEE Sarnoff Symposium, Princeton, NJ, pp. 61–64, April 2004.
- [32] *Kumar G. and K.P. Ray*, “Broadband Nicrostrip Antennas ”Norwood, MA:Artech House, 2003.
- [33] *Wong K. L.*, “Compact and Broadband Nicrostrip Antennas ”New York: Wiley, 2002.
- [34] *Mayes P. E.*, “ Frequency-independent antennas and broad-band derivatives thereof ” IEEE Transactions on Antennas and Propagation, 104–111, January 1992.
- [35] *Huynh T. and K.F. Lee*, “Single-layer single-patch wideband microstrip antenna ” Electronic Letters, 31, 1310–1311, August 3, 1995.
- [36] *Weigand S., G. H. Huff, K. H. Pan, and J. T. Bernhard*, “Analysis and design of broad-band single-layer rectangular U-slot microstrip patch antennas ” IEEE Transactions on Antennas and Propagation, 51, 457–468, March 2003.
- [37] *Yang F.,X. X. Zhang, X. Ye, and Y. Rahmat-Samii*, “Wide-band E-shaped patch antennas for wireless communications ” IEEE Transactions on Antennas and Propagation, 49, 1094–1100, July 2001.
- [38] *Komanduri V. R.*, “Analysis and design of novel wideband printed antennas for through-wall microwave imaging applications ” MS.thesis, ECE Department, Villanova University, Villanova, PA July 2005.
- [39] *Komanduri V. R, A. Hoorfar, and N. Engheta*, “Low-profile array design considerations for through-the-wall microwave imaging applications ”2005 IEEE APS International Symposium Digest, Washington, DC, vol.3B, pp. 338–341, July 2005.
- [40] *Balanis C. A.*, “Antenna Theory, Analysis and Design ”3rd edn, Hoboken, NJ: Wiley, 2005.

- [41] *Brown G. H. and O. M. Woodward Jr.*, “Experimentally determined radiation characteristics of conical and triangular antennas ”*RCA Review*, 13(4), 425–452, December 1952.
- [42] *Kraus J. D.*, “Antennas ”2nd edn, New York: McGraw Hill, 1988, Chapter 7.
- [43] *Shin J. and D. H. Schaubert*, “Parameter study of stripline-fed Vivaldi notchantenna arrays ”*IEEE Transactions on Antennas and Propagation*, 47(5), 879–886, 1999.
- [44] *Thiele E. and A. Taflove*, “FDTD analysis of Vivaldi flared horn antennas and arrays ”*IEEE Transactions on Antennas and Propagation*, 42, 633–640, May 1994.
- [45] *Schaubert D. H. and T-H.Chio*, “Wideband Vivaldi arrays for large aperture antennas ”*Proceedings of NFRA SKA Symposium on Technologies for Large Antenna Arrays*, A.B. Smolders and M.P. van Haarlem (eds.), Dwingeloo, the Netherlands, pp. 49–58, 1999.
- [46] *Yang Y., Y. Wang, and A. E. Fathy*, “Design of compact Vivaldi antenna arrays for UWB see through wall applications ” *Progress in Electromagnetics Research*, 82, 401–418, 2008.
- [47] *F. Ahmad, Y. Zhang, and M. Amin*, “Threedimensional wideband beamforming for imaging through a single wall, ” *IEEE Trans. GeoSci. Remote Sensing Lett.*, vol. 5, no. 2, pp. 176–179, Apr. 2008.
- [48] *G.Wang and M.G.Amin*, “Imaging through unknown walls using different standoff distances, ” *IEEE Trans.Signal Process.*, vol.54, no.10, pp.4015–4025, Oct. 2006.
- [49] *F. Ahmad, M.G. Amin, and G. Mandapati*, “Autofocusing of through-the-wall radar imagery under unknown wall characteristics, ” *IEEE Trans. Image Processing*, vol. 16, no. 7, July 2007, pp. 1785–1795. IEEE.
- [50] *K. M. Yemelyanov, J. A. McVay, N. Engheta, and A. Hoorfar*, “Adaptive polarization-difference imaging algorithms for through-the-wall microwave imaging scenarios, ” in *Proc. IEEE Int. Antennas Propag. Symp.*, Jul. 3–8, 2005, vol. 4B, pp. 114–117.

- [51] *K. M. Yemelyanov, J. A. McVay, A. Hoorfar, and N. Engheta*, “Polarization-contrast sensing in complex environment for through-the-wall microwave imaging applications, ” in Proc. IEEE Int. Antennas Propag. Symp., Jun. 9–15, 2007, pp. 1473–1476.
- [52] *C.-W. Wu and Z.-Y. Huang*, “Using the phase change of a reflected microwave to detect a human subject behind a barrier, ” *IEEE Trans. Biomed. Eng.*, vol. 55, no. 1, pp. 267–272, Jan. 2008.
- [53] *J. B. Keller*, “Geometrical theory of diffraction, ” *J. Opt. Soc. Amer.*, vol. 52, no. 2, pp. 116–130, Feb. 1962.
- [54] *C. V. Jakowatz, D. E. Wahl, P. H. Eichel, D. C. Ghiglia, and P. A. Thompson*, “Spotlight-Mode Synthetic Aperture Radar: A Signal Processing Approach, ” Norwell, MA: Kluwer, 1996.
- [55] *W. G. Carrara, R. S. Goodman, and R. M. Majewski*, “Spotlight Synthetic Aperture Radar, ” Norwood, MA: Artech House, 1995.
- [56] *R. Moses, L. Potter, and M. Çetin*, “Wide-angle SAR imaging, ” in Proc. SPIE—Algorithms for Synthetic Aperture Radar Imagery XI, E.G.Zelnio, Ed., Apr. 2004, vol. 5427, pp. 164–175 .
- [57] *M. Gerry, L. Potter, I. Gupta, and A. van der Merwe*, “A parametric model for synthetic aperture radar measurements, ” *IEEE Trans. Antennas Propag.*, vol. 47, no. 7, pp. 1179–1188, Jul. 1999.
- [58] *M. Çetin and W. C. Karl*, “Feature-enhanced synthetic aperture radar image formation based on nonquadratic regularization, ” *IEEE Trans. Image Process.*, vol. 10, no. 4, pp. 623–631, Apr. 2001.
- [59] *N. Ramakrishnan, E. Ertin, and R. Moses*, “Joint enhancement of multichannel SAR data, ” in Proc. SPIE Defense Security Symp.—Algorithms for Synthetic Aperture Radar Imagery XIV, Orlanda, FL, Apr. 2007, vol. 6568, p. 65680B.
- [60] *M. Soumekh*, “Synthetic Aperture Radar Signal Processing, ” Wiley, New York, 1999.

- [61] *T. Dogaru*, “AFDTD User’s Manual,” ARL-TR-5145, U.S. Army Research Laboratory, Adelphi, MD, March 2010.
- [62] *Remcom*. Web page. <http://www.remcom.com>.
- [63] *M.L. Stowell, B.J. Fasnfest, and D.A. White*, “Investigation of radar propagation in buildings: A 10-billion element Cartesian-mesh FETD simulation,” *IEEE Transactions on Antennas and Propagation*, 56, 2241–2250, August 2008.
- [64] *Science Applications International Corporation (SAIC)* Web page. <http://www.saic.com/products/software/xpatch>.
- [65] *T. Dogaru and C. Le*, “Validation of Xpatch Computer Models for Human Body Radar Signature,” ARL-TR-4403, U.S. Army Research Laboratory, Adelphi, MD, March 2008.
- [66] *T. Dogaru and C. Le*, “Simulated Radar Range Profiles of Simple Room as Computed by FDTD and Xpatch,” ARL-TR-4420, U.S. Army Research Laboratory, Adelphi, MD, April 2008.
- [67] *T. Dogaru, A. Sullivan, C. Le, and C. Kenyon*, “Radar signature prediction for sensing through the wall by Xpatch and AFDTD,” 2009 HPC Users Group Conference, San Diego, CA, June 2009.
- [68] *T. Dogaru and C. Le*, “SAR Images of a Simple Room Based on Computer Models,” ARL-TR-5193, U.S. Army Research Laboratory, Adelphi, MD, May 2010.
- [69] *T. Dogaru, L. Nguyen, and C. Le*, “Computer Models of the Human Body Signature for Sensing through the Wall Radar Application,” ARL-TR-4290, U.S. Army Research Laboratory, Adelphi, MD, September 2007.
- [70] *W. Zhang, and A. Hoorfar*, “A Generalized Approach for SAR and MIMO Radar Imaging of Building Interior Targets With Compressive Sensing,” *IEEE Antennas and Wireless Propagation Letters*, Vol.14,2015.
- [71] *T. Dogaru, and C. Le*, “Through-the-Wall Radar Simulations for Complex Room Imaging,” ARL-TR-5205, May 2010.

- [72] *F. Soldovieri, and R. Solimene*, “Through-Wall Imaging via a Linear Inverse Scattering Algorithm,” *IEEE Geoscience and Remote Sensing Letters*, Vol. 4, No. 4, October 2007.
- [73] *W. Zhang, and A. Hoorfar*, “Two dimensional diffraction tomographic algorithm for through-wall radar imaging,” *Prog. Electromagn. Res. B*, vol. 31, pp. 205–218, 2011.
- [74] *W. J. Zhong, C. M. Tong, L. Xin, and Y. Geng*, “A Novel Near Field Imaging Approach for Through-wall Imaging,” (Cross Strait Quad-Regional Radio Science and Wireless Technology Conference, Harbin, 2011), pp. 164–167.
- [75] *T. Dogaru, L. Nguyen, and C. Le*, “Computer Models of the Human Body Signature for Sensing Through the Wall Radar Applications,” ARL-TR-4290; U.S. Army Research Laboratory: Adelphi, MD, September 2007.
- [76] *R. J. Burkholder, P. Chang, Y. Bayram, R. Marhefka, and J. Volakis*, “Model-based near-field imaging of objects inside a room” in *Proc. IEEE Antennas Propag. Int. Symp.*, May 2007, pp. 1469–1472.
- [77] *J. Delliere, H. Maitre, and A. Maruani*, “SAR measurement simulation on urban structures using a FDTD technique” in *Proc. Urban Remote Sens. Joint Event*, Mar. 2007, pp. 1–8.
- [78] *F. Ahmad and M.G. Amin*, “Through-the-wall radar imaging experiments” in *Proc. IEEE Workshop Signal Processing Applications for Public Security Forensics*, 2007, pp. 1–5.
- [79] *M. Dehmollaian and K. Sarabandi*, “Analytical, numerical, and experimental methods for through-the-wall radar imaging” in *Proc. IEEE Int. Conf. Acoustics, Speech, Signal Processing (ICASSP)*, 2008, pp. 5181–5184.
- [80] *W. Zhang and A. Hoorfar*, “Three-dimensional real-time through-the wall radar imaging with diffraction tomographic algorithm” *IEEE Trans. Geosci. Remote Sens.*, vol.51, no.7, pp.4155–4163, Jul.2013.
- [81] *Q. Huang, L. Qu, B. Wu, and G. Fang*, “UWB through-wall imaging based on compressive sensing” *IEEE Trans. Geosci. Remote Sens.*, vol. 48, no. 3, pp. 1408–1415, Mar. 2010.

- [82] *W. Wang, D. Wang, and Y. Jiang*, “Multiple statuses of through-wall human being detection based on compressed UWB radar data” *Journal on Wireless Communications and Networking*, (2016) 2016:203.
- [83] *P. P. S. Chauhan, and D. Singh*, “Through-the Wall Imaging (TWI) Radar for detection, classification and identification of targets based on RCS” *National Conference on Recent Advances in Electronics and Computer Engineering, RAECE -2015, Feb.13-15, 2015, IIT Roorkee, India.*
- [84] *C. Debes, M. G. Amin and A. M. Zoubir*, “Target Detection in Single- and Multiple-View Through-the-Wall Radar Imaging ” *IEEE Transactions on Geoscience and Remote Sensing*, vol. 47, no. 5, May 2000.
- [85] *F. Ahmad*, “Multi-location wideband through-the-wall beamforming ” in *Proc. 33rd IEEE ICASSP, Las Vegas, NV, 2008*, pp. 5193–5196.
- [86] *A. Hunt*, “Image formation through walls using a distributed radar sensor array ” in *Proc. 32nd Appl. Imagery Pattern Recog. Workshop, Sep. 2003*, pp. 232–237.
- [87] *F. Ahmad and M. Amin*, “High-resolution imaging using capon beamformers for urban sensing applications” in *Proc. IEEE ICASSP, Mar. 2007*, vol. 2, pp. 985–988.
- [88] *J. E. Peabody, G. L. Charvat, J. Goodwin, and M. Tobias*, “Through-Wall Imaging Radar ” *Lincoln Laboratory Journal*, vol. 19, no. 1, 2012.
- [89] *T.S. Ralston, G.L. Charvat, and J.E. Peabody*, “Real-Time Through-Wall Imaging using an Ultrawideband MultipleInput Multiple-Output (MIMO) Phased-Array Radar System, ” *Proceedings of the IEEE International Symposium on Phased Array Systems and Technology*, pp. 551–558, 2010.
- [90] *F. Ahmad, G. J. Frazer, S. A. Kassam, and M. G. Amin*, “Design and implementation of near-field, wideband synthetic aperture beamformers,” *IEEE Trans. AES*, vol. 40, no. 1, pp. 206-220, Jan. 2004.
- [91] *C. Le, T. Dogaru, L. Nguyen, and M. A. Ressler*, “Ultrawideband (UWB) radar imaging of building interior: Measurements and predictions,” *IEEE Trans. Geosci. Remote Sens.*, vol. 47, no. 5, pp. 1409–1420, May 2009.

- [92] *A. Sengur, M. Amin, F. Ahmad, P. Sevigny, and D. DiFilippo*, “Textural Feature Based Target Detection in Through-the-Wall Radar Imagery,” Radar Imaging Lab, Center for Advanced Communications, Villanova University, 800 Lancaster Ave, Villanova, PA 19085, USA.
- [93] *Giordano, Nicholas*, “ College Physics: Reasoning and Relationships, ” Cengage Learning. pp. 421–424, 2009.
- [94] *Possel, Markus*, “ Waves, motion and frequency: the Doppler effect, ” Einstein Online, Vol. 5. Max Planck Institute for Gravitational Physics, Potsdam, Germany. Retrieved September 4, 2017.
- [95] *Henderson, Tom*, “ The Doppler Effect – Lesson 3, Waves, ” Physics tutorial. The Physics Classroom. Retrieved September 4, 2017.
- [96] *Chen, V.C.*, “Analysis of radar micro-Doppler signature with time-frequency transform,” Proceedings of the IEEE Workshop on Statistical Signal and Array Processing.(SSAP), Pocono, PA, pp. 463–466, 2000.
- [97] *Chen, V.C., F. Li, S. Ho, and H. Wechsler*, “ Micro-Doppler effect in radar—phenomenon, model, and simulation study, ” IEEE Transactions on Aerospace and Electronic System, 42(1), 2–21, 2006.
- [98] *Chen, V.C. and H. Ling*, “ Time-Frequency Transforms for Radar Imaging and Signal Analysis, ” Artech House, Boston, MA, 2002.
- [99] *Gupta, M.S.*, “ Definition of instantaneous frequency and frequency measurability, ” American Journal of Physics, 43(12), 1087–1088, 1975.
- [100] *Kay, S.M.*, “ A fast and accurate single frequency estimator, ” IEEE Transactions on Acoustics, Speech, and Signal Processing, 37(12), 1987–1990, 1989.
- [101] *Rife, D.C. and R.R. Boorstyn*, “ Single tone parameter estimation from discrete time observations, ” IEEE Transactions on Information Theory, 20(5), 591–598, 1974.
- [102] *.Cohen, L.*, “ Time-Frequency Analysis, ” Prentice Hall, New York, 1995.
- [103] *Qian, S. and D. Chen*, “ Introduction to Joint Time-Frequency Analysis—Methods and Applications, ” Prentice Hall, Englewood Cliffs, NJ, 1996.

- [104] *Time-Frequency Toolbox*: <http://tftb.nongnu.org/>.
- [105] *Baker, C.J. and B.D. Trimmer*, “ Short-range surveillance radar systems, ” *Electronics and Communication Engineering Journal*, 12(4), 181–191, August 2000.
- [106] *Setlur, P., Amin, M., and Ahmad, F.*, “ Analysis of micro-doppler signals using linear FM basis decomposition, ” ONR grant no. N00014-98-1-0176.
- [107] *S. Ram, C. Christianson, Y. Kim, and H. Ling*, “Simulation and analysis of human micro-dopplers in through-wall environments,” *IEEE Trans. Geoscience and Remote Sensing*, 2010.
- [108] *S. Ram, Y. Li, A. Lin, and H. Ling*, “Doppler-based detection and tracking of humans in indoor environments,” *Journal of the Franklin Institute*, 2008.
- [109] *S. Ram and H. Ling*, “Through-wall tracking of human movers using joint doppler and array processing,” *IEEE Geoscience and Remote Sensing Letters*, 2008.
- [110] *N. Maaref, P. Millot, P. Pichot, and O. Picon*, “A study of UWB FM-CW radar for the detection of human beings in motion inside a building,” *IEEE Trans. Geosci. Remote Sens.*, vol. 47, no. 5, pp. 1297–1300, 2009.
- [111] *S. Nag, M. A. Barnes, T. Payment., and G. Holladay*, “An ultra-wideband through-the-wall radar for detecting the motion of people in real time,” *Proceedings of SPIE: Radar Sensor Technology and Data Visualization*, July 2002, Vol. 4744, pp. 48-57.
- [112] *Wilson, J., and Patwari, N.*, “See-through walls: Motion tracking using variance-based radio tomography networks,” *In IEEE Transactions on Mobile Computing*, 2011.
- [113] *J. D. Black*, “Motion and ranging sensor through-the-wall surveillance system,” *Proc. SPIE*, Vol: 4708, pp: 114-121, 2002.
- [114] *S. Wu, G. Fang*, “Detection and Tracking of Moving Target Behind Wall using UWB Through-Wall Radar,” *Proceedings of IEEE on Intelligent System*

Design and Engineering Application (ISDEA), Changsha, 2010, pp. 605–608

- [115] *J. Li, Z. Zeng, J. Sun, F. Liu*, “Through-Wall Detection of Human Being’s Movement by UWB Radar,” *IEEE Geosci. Remote Sens. Lett.* 9(6), 1079–1083 (2012).
- [116] *H. Wang, R. Narayanan, and Z. Zhou*, “Through-wall imaging of moving targets using uwb random noise radar,” *IEEE Antennas and Wireless Propagation Letters*, 2009.
- [117] *Hunt, A. R.*, “Use of a Frequency-hopping Radar for Imaging and Motion Detection Through Walls,” *IEEE Transaction on Geophysics and Remote Sensing* May 2009, 47, 1402–1408.
- [118] *Adib, F., Hsu, C., Mao, H., Katabi, D., Durand, F.*, “Capturing the Human Figure Through a Wall,” *ACM Trans. Graph.* 34, 6, Article 219 (November 2015), 13 pages. DOI = 10.1145/2816795.2818072 <http://doi.acm.org/10.1145/2816795.2818072>, 2015.
- [119] *Chetty, K., Smith, G., and Woodbridge, K.*, “Through-the-wall sensing of personnel using passive bistatic wifi radar at standoff distances,” *IEEE Trans. Geoscience and Remote Sensing* 2012.
- [120] *B. Scheers*, “Ultra-Wideband Ground Penetrating Radar, with Application to the Detection of Antipersonnel Landmines (Doctoral Dissertation),” retrieved from Royal Military Academy, (2011).
- [121] *D. J. Daniels*, “Ground Penetrating Radar,” Institution of Electrical Engineers, London (2004).
- [122] *E. C. Utsi*, “Ground Penetrating Radar Theory and Applications,” Elsevier (Butterworth-Heinemann), Oxford (2017).
- [123] *X. L. Travassos et al.*, “A Review of Ground Penetrating Radar Antenna Design and Optimization,” *Journal of Microwaves, Optoelectronics and Electromagnetic Applications*, vol. 17, no. 3, pp. 385-402 (2018).

- [124] *F. Fioranelli*, “Through-the-Wall Detection Using Ultra Wide Band Frequency Modulated Interrupted Continuous Wave Signals (Doctoral Dissertation),” retrieved from Durham University, (2013).
- [125] *D. K. Cheng*, “Fundamentals of Engineering Electromagnetics,” Prentice-Hall, New Jersey (1993).
- [126] *R. E. Collin*, “Foundations for Microwave Engineering,” IEEE Press, New York (2001).
- [127] *S. J. Orfanidis*, “Electromagnetic Waves and Antennas,” Rutgers University Press, New Jersey (2008).
- [128] *E. Pasolli et al.*, “Automatic Detection and Classification of Buried Objects in GPR Images using Genetic Algorithms and Support Vector Machines,” IEEE International Geoscience and Remote Sensing Symposium, vol. 2, pp. 525-528 (2008).
- [129] *U. Pisipati*, “Techniques for Improving Landmine Detection using Ground Penetrating Radar (Master’s Thesis),” retrieved from University of Missouri (2006).
- [130] *B. Karlsten et al.*, “Comparison of PCA and ICA based Clutter Reduction in GPR Systems for Anti-Personal Landmine Detection,” 11th IEEE Signal Processing Workshop on Statistical Signal Processing, pp. 146-149 (2001).
- [131] *F. S. Tjora, E. Eide and L. Lundheim*, “Evaluation of Methods for Ground Bounce Removal in GPR Utility Mapping,” 10th International Conference on Ground Penetrating Radar, pp 1-4 (2004).
- [132] *L. van Kempen et al.*, “Signal Processing and Pattern Recognition Methods for Radar AP Mine Detection and Identification,” Second International Conference on the Detection of Abandoned Land Mines, pp. 81 - 85 (1998).
- [133] *Seng, C. H., Amin, M. G., Ahmad, F. and Bouzerdoun, A.*, “Segmentations of through-the-wall radar images,” Proc. IEEE Radar Conf., (2012).
- [134] *J. S. Lee, and I. Jurkevich*, “Segmentation of SAR images,” IEEE Trans. Geosci. Remote Sens., vol. 27, no. 6, pp. 674-680, 1989.

- [135] *R. Schoenmakers and L. Vuurpijl*, “Segmentation and classification of combined optical and radar imagery,” in Proc. Int. Geosci. Remote Sens. Symp., 1995, pp. 2151–2153.
- [136] *M. Sezgin and B. Sankur*, “Survey over image thresholding techniques and quantitative performance evaluation,” J. of Electronic Imag., vol. 13, no. 1, pp. 146–165, 2004.
- [137] *C. H. Seng, M. G. Amin, and A. Bouzerdoun*, “Image segmentations for through-the-wall radar target detection,” IEEE Transactions on Aerospace and Electronic Systems vol. 49, no. 3, July 2013.
- [138] *M. G. Amin, P. Setlur, F. Ahmad, P. Sevigny, and D. DiFilippo*, “Histogram-based segmentation for stationary target detection in urban environments,” retrieved from Villanova University.
- [139] *V. Kilaru, M. Amin, F. Ahmad, P. Sevigny, and D. DiFilippo*, “Gaussian mixture modeling approach for stationary human identification in through-the-wall radar imagery,” Journal of Electronic Imaging, Vol. 24(1), Feb 2015 .
- [140] *Harlick, R. M., Shanmugam, K. and Dinstein, I.*, “Textural features for image classification,” IEEE Trans. Systems, Man, Cybernetics SMC-3(6), 610-621 (1973).
- [141] *Reed, T.R. and Dubuf, J.M.H.*, “A review of recent texture segmentation and feature extraction techniques,” CVGIP: Image Understanding 57(3), 359-372 (1993).
- [142] *An-Zen Shih, Sie Jheng-Huei and Peng Kaiyang*, “Image classification by using a hybrid fractal-based method,” Proc. Int. Conf. on Machine Learning and Cybernetics 4, 1800-1803 (2011).
- [143] *Idrissa M. and Acheroy M.*, “Texture classification using Gabor filters,” Pattern Recognition Letters 23(7), 10951102 (2002).
- [144] *Ciesielski, V., Lam, B. and Minh Luan Nguyen*, “Comparison of evolutionary and conventional feature extraction methods for malt classification,” Proc. IEEE Congress Evolutionary Computation, 1-7 (2012).

- [145] *Lukashevich, M. and Sadykhov, R.*, “Texture analysis: Algorithm for texture features computation,” Proc. Intl. Conf. Problems of Cybernetics and Informatics, 1-3 (2012).
- [146] *C. Debes*, “Advances in Detection and Classification for Through-the-Wall Radar Imaging,” retrieved from Technischen Universitat Darmstadt(2010).
- [147] *T. M. Ferguson and D. Baker*, “Feature extraction using the Hough Transform,” (2002).
- [148] *U. Kazhagamani and E. Murugasen*, “A Hough Transform based feature extraction algorithm for Finger Knuckle Biometric Recognition System,” Advanced Computing, Networking and Informatics, vol. 1., (2014).
- [149] *N. Dalal and B. Triggs*, “Histograms of Oriented Gradients for Human Detection” IEEE Computer Society Conference on Computer Vision and Pattern Recognition, 2005.
- [150] *M. J. A. Patwary, S. Parvin, and S. Akter*, “Significant HoG-Histogram of oriented gradient feature selection for human detection” International Journal of Computer Applications, 2015.
- [151] *T. Kobayashi, A. Hidaka, and T. Kurita*, “Selection of histograms of oriented gradient features for pedestrian detection” Conference paper, November 2007.
- [152] *P. Carcagni, M. D. Coco, M. Leo, and C. Distanti*, “Facial expression recognition and histograms of oriented gradients : a comprehensive study” Published online 2015 Oct 26. doi: 10.1186/s40064-015-1427-3.
- [153] *T. D. Bufler and R. M. Narayanan*, “Radar classification of indoor targets using support vector machines,” IET Radar Sonar Navig., Vol. 10, Iss. 8, pp. 1468-1476, 2016.
- [154] *F. F. Wang and Y. R. Zhang*, “The support vector machine for dielectric target detection through a wall,” Progress In Electromagnetics Research Letters, vol. 23, 10.2528/PIERL11031106, 2011.
- [155] *C. Chen, C. Chen and C. Chen*, “A Comparison of Texture Features Based on SVM and SOM,” ICPR, vol. 2, pp. 630-633, 2006.

- [156] *A. C. Braun, U. Weidner and S. Hinz*, “Classification in high-dimensional feature spaces-Assessment using SVM, IVM and RVM with focus on simulated EnMAP data,” *IEEE Journal of Selected Topics in Applied Earth Observations and Remote Sensing*, vol. 5, no. 2, pp. 436-443 (2012).
- [157] *Y. Bazi and F. Melgani*, “Toward an optimal SVM classification system for hyperspectral remote sensing images,” *IEEE Transactions on Geoscience and Remote Sensing*, vol. 44, no. 11, pp. 3374-3385 (2006).
- [158] *Z. Gavrilov*, “SVM Tutorial (Doctoral Dissertation),” retrieved from Massachusetts Institute of Technology (2012).
- [159] *G. Smith and B. Mobasseri*, “Robust through-the-wall radar image classification using a target-model alignment procedure,” *IEEE transactions on image processing*, vol. 21, 10.1109/TIP.2011.2166967 (2011).
- [160] *J. Han, M. Kamber and J. Pei*, “Data Mining Concepts and Techniques,” Elsevier, Massachusetts (2012).
- [161] *K. M. A. Chai, H. T. Ng and H. L. Chieu*, “Bayesian Online Classifiers for Text Classification and Filtering,” *Proceedings of the 25th Annual International ACM SIGIR*, pp. 97-104 (2002).
- [162] *W. Wang and D. Wang*, “KNN Classification Algorithm for Multiple Statuses Detection of Through-Wall Human Being,” 10.1007/978-981-10-3229-5 (2018).
- [163] *M. Venkataramana*, “A review of recent texture classification:Methods,” *Journal of Computer Engineering*, vol. 14, issue 1, pp. 54-60, 2013.
- [164] *E. Fix and J. L. Hodges*, “Discriminatory analysis, nonparametric discrimination: consistency properties,” *International Statistical Review*, vol. 57, no. 3, pp. 238-247 (1989).
- [165] *J. M. Keller, M. R. Gray and J. A. Givens*, “A fuzzy K-Nearest Neighbor algorithm,” *IEEE Transactions on Systems, Man, And Cybernetics*, vol. 15, no. 4, pp. 580-585 (1985).

- [166] *A. A. Mostafa*, “Segmentation and Classification for through-the-wall radar imaging,” retrieved from Technischen Universitat Darmstadt(2013).
- [167] *A.D. Lillo, G. Motta, J.A. Storer*, “Multiresolution Rotation-Invariant Texture Classification Using Feature Extraction in the Frequency Domain and Vector Quantization,” DCC, pp. 452-461, 2008.
- [168] *V.N. Vasyukov, and N.V. Sysoev*, “Texture Image Segmentation Using Multi-scale Wavelet-Domain Hidden Markov Model,” IFOST, pp. 151-153, 2007.
- [169] *C. H. Seng*, “Image processing for enhanced through-the-wall radar imaging,” retrieved from University of Wollongong(2013).
- [170] *Mathworks Web Page www.mathworks.com*.
- [171] *C. Tomasi*, “Histograms of oriented gradients”, 2015.
- [172] *B. E. Boser, I. M. Guyon, and V. N. Vapnik*, “A training algorithm for optimal margin classifier,” Proceedings of the fifth annual workshop on Computational learning theory-COLT’92. p. 144.
- [173] *A. Giannopoulos and C. Warren*, “gprMax: Electromagnetic Modelling Software,”(2015)[www.gprmax.com].
- [174] *Warren, C., Giannopoulos, A., and Giannakis, I.*, “An advanced GPR modelling framework the next generation of gprMax,” In Proc. 8th Int. Workshop Advanced Ground Penetrating Radar (2015).
- [175] *Giannopoulos, A.*, “Modelling ground penetrating radar by GprMax,” Construction and Building Materials, 19(10), 755-762.
- [176] *K. S. Kunz and R. J. Luebbers*, “The finite difference time domain method for electromagnetics,” CRC press(1993).
- [177] *A. Taflove and S. C. Hagness*, “Computational electrodynamics,” Artech house(2005).
- [178] *A. Giannopoulos*, “The investigation of Transmission-Line Matrix and Finite-Difference Time-Domain Methods for the Forward Problem of Ground Penetrating Radar,” D. Phil thesis, Department of Electronics, University of York, UK, 1997.

- [179] *D. Ireland and A. Abbosh*, “Modeling human head at microwave frequencies using optimized debye models and FDTD method,” *IEEE Transactions on Antennas and Propagation*, vol. 61, no. 4, pp. 2352-2355, April 2013.
- [180] *Dr. R. Rudd, Dr. K. Craig, Dr. M. Ganley, and R. Hartless*, “Building Materials and Propagation,” retrieved from Aegis Systems Limited, 2014.
- [181] *B. Daout, M. Sallin, and H. Wipf*, “Measurement of complex permittivity of large concrete samples with an open-ended coaxial line” retrieved from Montena Technology, 2014.

APPENDIX A

GPRMAX INPUT FILE SAMPLE

A sample of gprMax input file can be seen in figure A.1. In this input file, title of model, size of model, the values of the discretization spatial steps of model, time window of model, number of threads used, electromagnetic properties of the room material, electromagnetic properties of the object(not human) material, electromagnetic properties of the human material, model of room, thickness of wall, model of human, position of human, model of object(not human), position of object(not human), gaussiandot waveform which has 1.5 GHz center frequency and 10 Amps amplitude, Hertzian dipole Tx start position, Hertzian dipole Rx start position, Tx step size, Rx step size are defined.

As seen from figure A.1, size of simulation model is $80 \times 60 \times 15 \text{ cm}^3$. The first, second and third values represent the size of the model in the x, y, and z directions, respectively. The values of the discretization spatial steps in this model are $2 \times 2 \times 2 \text{ mm}^3$. The first, second and third values represent Δx , Δy , and Δz , respectively. The time window of the model is 4ns, the number of threads used, which is an important factor for the speed of simulation and is related to the computer's processor, is 8. The relative permittivity, the conductivity, the relative permeability, and the magnetic loss of wall material in this simulation model are, respectively, 3, 0.01, 1, 0, the relative permittivity, the conductivity, the relative permeability, and the magnetic loss of the object (not human) material in this simulation model are, respectively, 5, 0.01, 1, 0, the relative permittivity, the conductivity, the relative permeability, and the magnetic loss of the human material in this simulation model are, respectively, 8, 0.065, 1, 0. The wall thickness is 2 mm in this model. A cylinder with a radius of 1 cm and a length of 10 cm is used as a human body. A sphere with a radius of 1cm is used as

```

#title: Through the wall radar imaging _____ Title of Model
#domain: 8.000e-01 6.000e-01 1.500e-01 _____ Size of model
#dx_dy_dz: 2.000e-03 2.000e-03 2.000e-03 _____ The values of the discretization spatial steps of model
#time_window: 4.000e-09 _____ Time window of model : 4ns
#num_threads: 8 _____ Number of threads used
#material: 3 0.01 1 0 wall _____ Electromagnetic properties of the room material
#material: 5 0.01 1 0 object _____ Electromagnetic properties of the object (not human) material
#material: 8 0.065 1 0 human _____ Electromagnetic properties of the human material
#box: 0.000e+00 0.000e+00 0.000e+00 8.000e-01 6.000e-01 1.000e-01 wall _____ Model of room
#box: 0.002e+00 0.002e+00 0.002e+00 7.980e-01 5.980e-01 0.980e-01 free_space _____
#cylinder: 0.2 0.2 0.05 0.3 0.2 0.05 0.01 human _____ Model of human
#sphere: 0.31 0.2 0.05 0.01 human _____
#box: 0.1 0.4 0.05 0.3 0.5 0.07 object _____ Model of object(Not human)
#cylinder: 0.2 0.45 0.03 0.2 0.45 0.05 0.02 object _____
#waveform: gaussiandot 10.000e+00 1.500e+09 src1 _____ Gaussian waveform at 1.5 GHz
#hertzian_dipole: x 0.010e-01 0.010e-01 1.200e-01 src1 _____ Hertzian dipole Tx start position
#rx: 0.210e-01 0.010e-01 1.200e-01 _____ Hertzian dipole Rx start position
#src_steps: 0.000e+00 1.000e-02 0.000e+00 _____ Tx step size
#rx_steps: 0.000e+00 1.000e-02 0.000e+00 _____ Rx step size

```

Figure A.1: Sample of gprMax input file

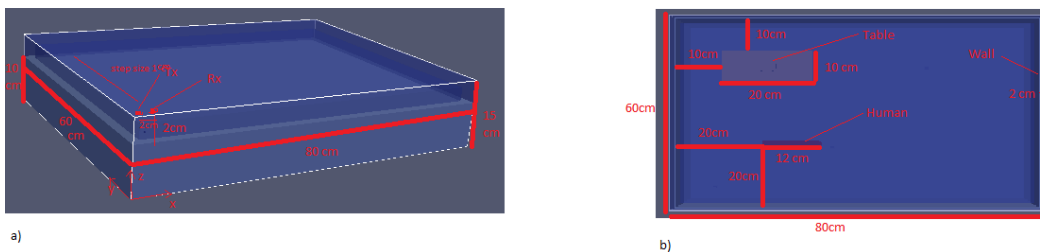


Figure A.2: a) External view of the model b) Inside view of the model

a human head. A table is designed as a non-human object in this simulation model. Gaussiandot waveform which has 1.5 GHz center frequency and 10 Amps amplitude is used as a waveform. Hertzian dipoles are used as transmitter and the receiver antennas. The transmitter and receiver are moved 59 times along the y-axis at a 1 cm interval to create a B-Scan image. The input file shown in the figure A.1 creates the models shown in the figure A.2.

There are some points to consider when creating models in gprMax. In the FDTD approach, Maxwell's equations are solved by discretizing both space and time continua. The discretization spatial Δx , Δy , and Δz and temporal Δt steps play important role in gprMax simulations because the smaller the values of discretization steps, the closer the model to real representation. However, due to the memory, the processing capacity of the computer used and time, there is a limitation in choosing how small the values of discretization steps will be. The designer must know these limitations and make the selection accordingly. Moreover, the values of the discretization spatial

and temporal steps are assigned dependently to provide stability condition[173]. The stability condition can be defined as[173]

$$\Delta t \leq \frac{1}{c \sqrt{\frac{1}{(\Delta x)^2} + \frac{1}{(\Delta y)^2} + \frac{1}{(\Delta z)^2}}} \quad (\text{A.1})$$

where c is the speed of light. As a result, the value of the discretization temporal step is bounded by the values of the discretization spatial steps[173]. As in this input file sample, if the value of the discretization temporal step is not specified in the gprMax input file, Δt is determined at the exact boundary according to the equation A.1 by the gprMax software. That is, in this sample, Δt is nearly equal to $3.85e^{-12}$ second. As can be seen in the equation A.1, if Δx , Δy , Δz have small values, Δt has a small value. As a result, it will be necessary to increase the number of iterations to reach the specified time window, as will be seen in the equation A.2.

Furthermore, the iteration number is an important factor that determines the speed of simulation and the size of the A-Scan and B-Scan data. Iteration number can be defined as

$$IterationNumber = \frac{t}{\Delta t} \quad (\text{A.2})$$

where t represents the time window of the model, and Δt represents the value of the discretization temporal step. In this sample, the iteration number is nearly equal to 1040. As shown in the equation A.2, if the specified time window value increases, the iteration number value increases. Therefore, the time taken to complete the simulation will increase.

Moreover, the number of cells in a gprMax model is another important factor that determines the speed of simulation and spatial resolution. The number of cells in a gprMax model can be defined as

$$NumberOfCells = \frac{x.y.z}{\Delta x.\Delta y.\Delta z} \quad (\text{A.3})$$

where $x.y.z$ represents the size of the model and $\Delta x.\Delta y.\Delta z$ represents the size of the

cell. In this sample, the number of cells is equal to $9e^6$. Also, it is important how many cells the objects created in the gprMax model consist of in terms of resolution[173]. For example, a cylinder or a sphere with a radius equal to one or two spatial steps does not look like a cylinder or a sphere[173].

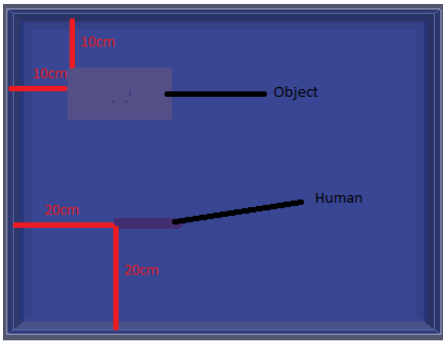
Moreover, in gprMax simulation model, the values of the discretization spatial steps should satisfy condition as seen in equation A.4 to prevent dispersion.

$$\Delta x, \Delta y \text{ or } \Delta z \leq \frac{\lambda}{10} \quad (\text{A.4})$$

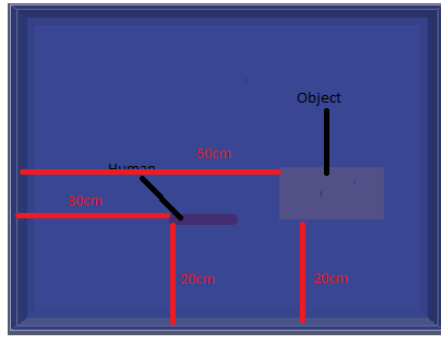
where λ represents wavelength. In this sample, the wavelength of the gaussian dot waveform at 1.5GHz is 0.2 m so condition at equation A.4 is satisfied. Moreover, PML and ABC are other important issues for the gprMax model. To learn PML and ABC, reference [173] should be examined in detail.

APPENDIX B

SIMULATION MODELS OF ALL 108 SCENARIOS

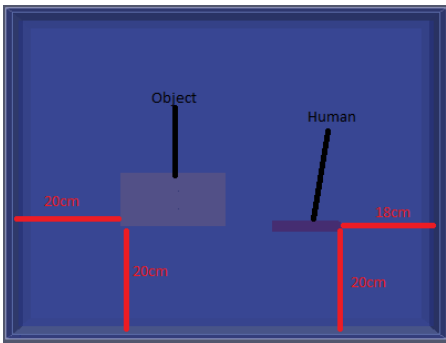


a)

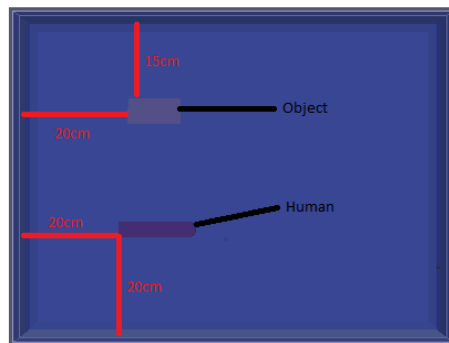


b)

Figure B.1: a) Simulation models of scenarios 1-6 b) Simulation models of scenarios 7-12

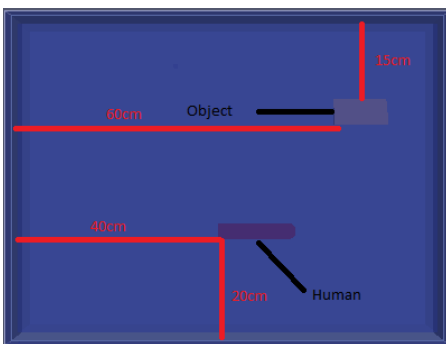


a)

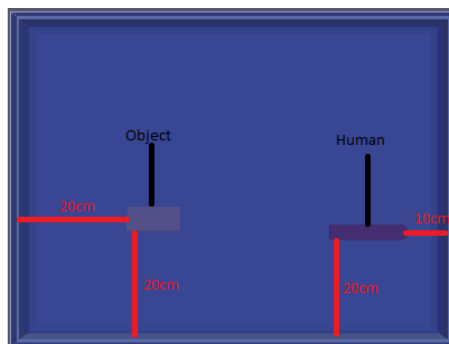


b)

Figure B.2: a) Simulation models of scenarios 13-18 b) Simulation models of scenarios 19-24



a)



b)

Figure B.3: a) Simulation models of scenarios 25-30 b) Simulation models of scenarios 31-36

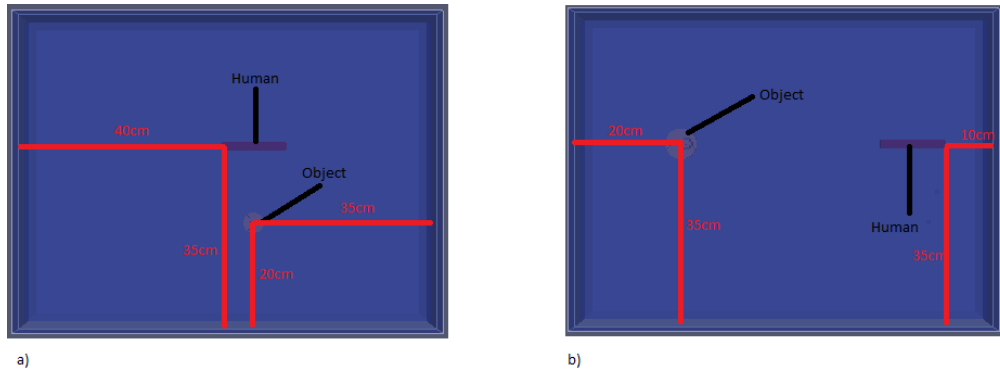


Figure B.4: a) Simulation models of scenarios 37-42 b) Simulation models of scenarios 43-48

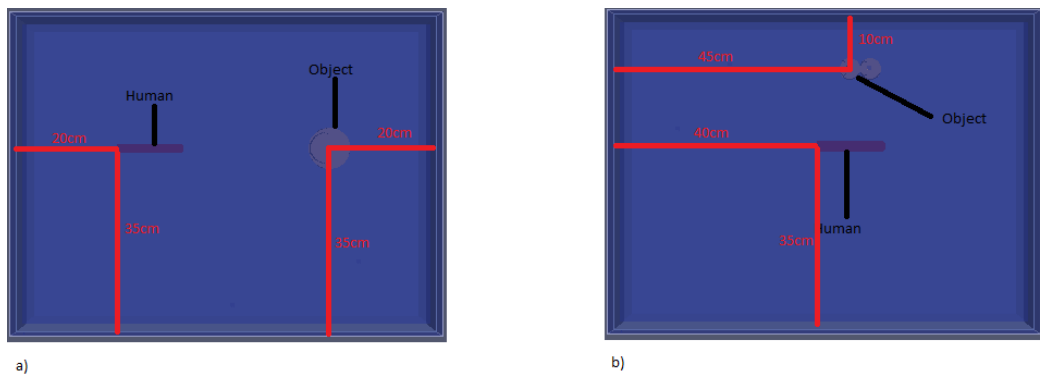


Figure B.5: a) Simulation models of scenarios 49-54 b) Simulation models of scenarios 55-60

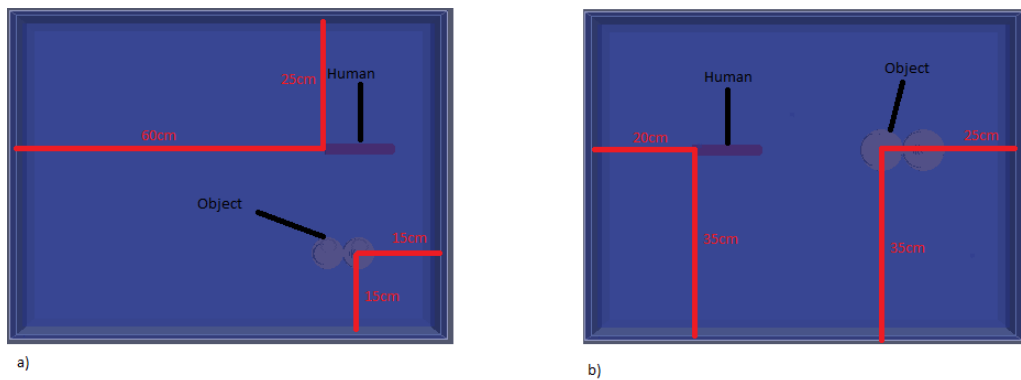
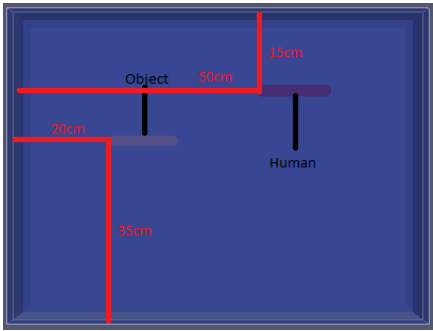
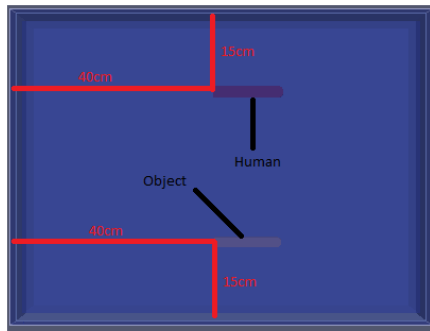


Figure B.6: a) Simulation models of scenarios 61-66 b) Simulation models of scenarios 67-72

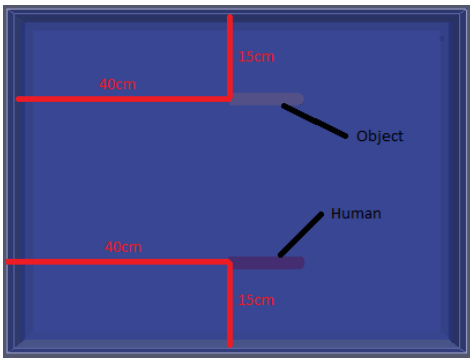


a)

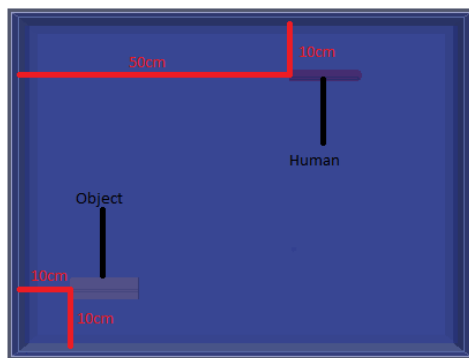


b)

Figure B.7: a) Simulation models of scenarios 73-78 b) Simulation models of scenarios 79-84

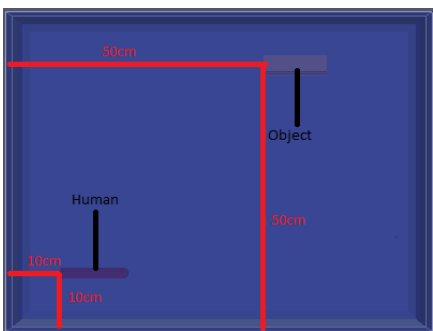


a)

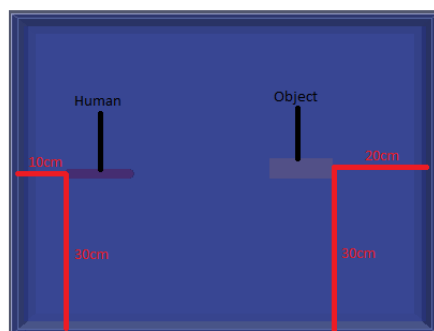


b)

Figure B.8: a) Simulation models of scenarios 85-90 b) Simulation models of scenarios 91-96



a)



b)

Figure B.9: a) Simulation models of scenarios 97-102 b) Simulation models of scenarios 103-108

APPENDIX C

**WALL PERMITTIVITY, OBJECT PERMITTIVITY, WALL THICKNESS,
HUMAN TYPE, OBJECT TYPE, OBJECT DEPTH, AND HUMAN DEPTH
OF ALL 108 SCENARIOS**

Table C.1: Wall permittivity, object permittivity, wall thickness and human type of scenarios between 1 and 27

Scenarios	Wall Permittivity	Object Permittivity	Wall Thickness(mm)	Human Type
1	3	5	2	a
2	3	5	4	a
3	3	5	6	a
4	10	5	2	a
5	10	5	4	a
6	10	5	6	a
7	3	7	2	a
8	3	7	4	a
9	3	7	6	a
10	10	7	2	a
11	10	7	4	a
12	10	7	6	a
13	3	11	2	a
14	3	11	4	a
15	3	11	6	a
16	10	11	2	a
17	10	11	4	a
18	10	11	6	a
19	3	2	2	b
20	3	2	4	b
21	3	2	6	b
22	10	2	2	b
23	10	2	4	b
24	10	2	6	b
25	3	6	2	b
26	3	6	4	b
27	3	6	6	b

Table C.2: Wall permittivity, object permittivity, wall thickness and human type of scenarios between 28 and 54

Scenarios	Wall Permittivity	Object Permittivity	Wall Thickness	Human Type
28	10	6	2	b
29	10	6	4	b
30	10	6	6	b
31	3	9	2	b
32	3	9	4	b
33	3	9	6	b
34	10	9	2	b
35	10	9	4	b
36	10	9	6	b
37	4	3	2	c
38	4	3	4	c
39	4	3	6	c
40	9	3	2	c
41	9	3	4	c
42	9	3	6	c
43	4	6	2	c
44	4	6	4	c
45	4	6	6	c
46	9	6	2	c
47	9	6	4	c
48	9	6	6	c
49	4	10	2	c
50	4	10	4	c
51	4	10	6	c
52	9	10	2	c
53	9	10	4	c
54	9	10	6	c

Table C.3: Wall permittivity, object permittivity, wall thickness and human type of scenarios between 55 and 81

Scenarios	Wall Permittivity	Object Permittivity	Wall Thickness	Human Type
55	4	2.5	2	d
56	4	2.5	4	d
57	4	2.5	6	d
58	9	2.5	2	d
59	9	2.5	4	d
60	9	2.5	6	d
61	4	5.5	2	d
62	4	5.5	4	d
63	4	5.5	6	d
64	9	5.5	2	d
65	9	5.5	4	d
66	9	5.5	6	d
67	4	7.5	2	d
68	4	7.5	4	d
69	4	7.5	6	d
70	9	7.5	2	d
71	9	7.5	4	d
72	9	7.5	6	d
73	5	3.5	2	e
74	5	3.5	4	e
75	5	3.5	6	e
76	7	3.5	2	e
77	7	3.5	4	e
78	7	3.5	6	e
79	5	6.5	2	e
80	5	6.5	4	e
81	5	6.5	6	e

Table C.4: Wall permittivity, object permittivity, wall thickness and human type of scenarios between 82 and 108

Scenarios	Wall Permittivity	Object Permittivity	Wall Thickness	Human Type
82	7	6.5	2	e
83	7	6.5	4	e
84	7	6.5	6	e
85	5	9.5	2	e
86	5	9.5	4	e
87	5	9.5	6	e
88	7	9.5	2	e
89	7	9.5	4	e
90	7	9.5	6	e
91	5	1.5	2	a
92	5	1.5	4	a
93	5	1.5	6	a
94	7	1.5	2	a
95	7	1.5	4	a
96	7	1.5	6	a
97	5	2.5	2	a
98	5	2.5	4	a
99	5	2.5	6	a
100	7	2.5	2	a
101	7	2.5	4	a
102	7	2.5	6	a
103	5	3.5	2	a
104	5	3.5	4	a
105	5	3.5	6	a
106	7	3.5	2	a
107	7	3.5	4	a
108	7	3.5	6	a

Table C.5: Object type, object depth, and human depth of scenarios between 1 and

27

Scenarios	Object Type	Object Depth(cm)	Human Depth(cm)
1	Table	3	4
2	Table	3	4
3	Table	3	4
4	Table	3	4
5	Table	3	4
6	Table	3	4
7	Table	3	4
8	Table	3	4
9	Table	3	4
10	Table	3	4
11	Table	3	4
12	Table	3	4
13	Table	3	4
14	Table	3	4
15	Table	3	4
16	Table	3	4
17	Table	3	4
18	Table	3	4
19	Prism	2	3.5
20	Prism	2	3.5
21	Prism	2	3.5
22	Prism	2	3.5
23	Prism	2	3.5
24	Prism	2	3.5
25	Prism	2	3.5
26	Prism	2	3.5
27	Prism	2	3.5

Table C.6: Object type, object depth, and human depth of scenarios between 28 and 54

Scenarios	Object Type	Object Depth(cm)	Human Depth(cm)
28	Prism	2	3.5
29	Prism	2	3.5
30	Prism	2	3.5
31	Prism	2	3.5
32	Prism	2	3.5
33	Prism	2	3.5
34	Prism	2	3.5
35	Prism	2	3.5
36	Prism	2	3.5
37	Sphere(r=2cm)	3	4.1
38	Sphere(r=2cm)	3	4.1
39	Sphere(r=2cm)	3	4.1
40	Sphere(r=2cm)	3	4.1
41	Sphere(r=2cm)	3	4.1
42	Sphere(r=2cm)	3	4.1
43	Sphere(r=3cm)	2	4.1
44	Sphere(r=3cm)	2	4.1
45	Sphere(r=3cm)	2	4.1
46	Sphere(r=3cm)	2	4.1
47	Sphere(r=3cm)	2	4.1
48	Sphere(r=3cm)	2	4.1
49	Sphere(r=4cm)	1	4.1
50	Sphere(r=4cm)	1	4.1
51	Sphere(r=4cm)	1	4.1
52	Sphere(r=4cm)	1	4.1
53	Sphere(r=4cm)	1	4.1
54	Sphere(r=4cm)	1	4.1

Table C.7: Object type, object depth, and human depth of scenarios between 55 and

81

Scenarios	Object Type	Object Depth(cm)	Human Depth(cm)
55	Two Sphere(r=2cm)	3	3.9
56	Two Sphere(r=2cm)	3	3.9
57	Two Sphere(r=2cm)	3	3.9
58	Two Sphere(r=2cm)	3	3.9
59	Two Sphere(r=2cm)	3	3.9
60	Two Sphere(r=2cm)	3	3.9
61	Two Sphere(r=3cm)	2	3.9
62	Two Sphere(r=3cm)	2	3.9
63	Two Sphere(r=3cm)	2	3.9
64	Two Sphere(r=3cm)	2	3.9
65	Two Sphere(r=3cm)	2	3.9
66	Two Sphere(r=3cm)	2	3.9
67	Two Sphere(r=4cm)	1	3.9
68	Two Sphere(r=4cm)	1	3.9
69	Two Sphere(r=4cm)	1	3.9
70	Two Sphere(r=4cm)	1	3.9
71	Two Sphere(r=4cm)	1	3.9
72	Two Sphere(r=4cm)	1	3.9
73	Such as human a	4	3.7
74	Such as human a	4	3.7
75	Such as human a	4	3.7
76	Such as human a	4	3.7
77	Such as human a	4	3.7
78	Such as human a	4	3.7
79	Such as human d	3.9	3.7
80	Such as human d	3.9	3.7
81	Such as human d	3.9	3.7

Table C.8: Object type, object depth, and human depth of scenarios between 82 and 108

Scenarios	Object Type	Object Depth(cm)	Human Depth(cm)
82	Such as human d	3.9	3.7
83	Such as human d	3.9	3.7
84	Such as human d	3.9	3.7
85	Such as human	3.8	3.7
86	Such as human	3.8	3.7
87	Such as human	3.8	3.7
88	Such as human	3.8	3.7
89	Such as human	3.8	3.7
90	Such as human	3.8	3.7
91	Two Cylinder(r = 1, l=10)	4	4
92	Two Cylinder(r = 1, l=10)	4	4
93	Two Cylinder(r = 1, l=10)	4	4
94	Two Cylinder(r = 1, l=10)	4	4
95	Two Cylinder(r = 1, l=10)	4	4
96	Two Cylinder(r = 1, l=10)	4	4
97	Two Cylinder(r = 1, l=10)	4	4
98	Two Cylinder(r = 1, l=10)	4	4
99	Two Cylinder(r = 1, l=10)	4	4
100	Two Cylinder(r = 1, l=10)	4	4
101	Two Cylinder(r = 1, l=10)	4	4
102	Two Cylinder(r = 1, l=10)	4	4
103	Two Cylinder(r = 1, l=10)	4	4
104	Two Cylinder(r = 1, l=10)	4	4
105	Two Cylinder(r = 1, l=10)	4	4
106	Two Cylinder(r = 1, l=10)	4	4
107	Two Cylinder(r = 1, l=10)	4	4
108	Two Cylinder(r = 1, l=10)	4	4

APPENDIX D

IMAGES OF DIFFERENT OBJECTS

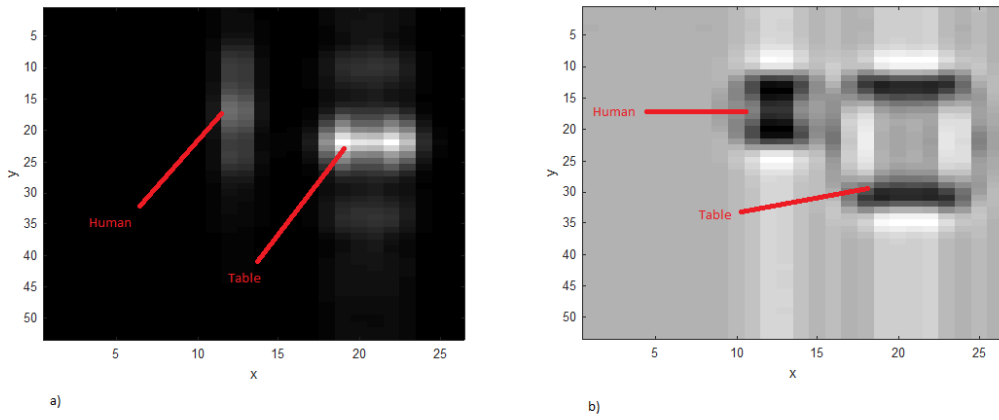


Figure D.1: a) The image of the energy sum of the top view of the 3-D data created by combining the B-Scan data b)C-Scan image at depth= 300

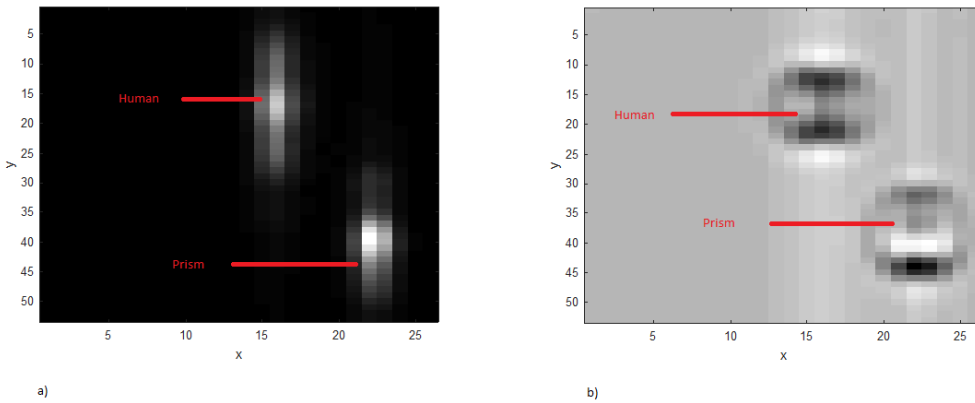


Figure D.2: a) The image of the energy sum of the top view of the 3-D data created by combining the B-Scan data b)C-Scan image at depth= 300

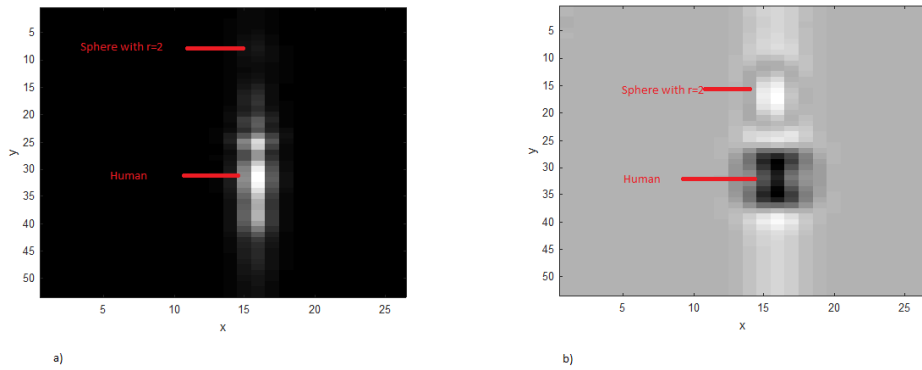


Figure D.3: a) The image of the energy sum of the top view of the 3-D data created by combining the B-Scan data b)C-Scan image at depth= 300

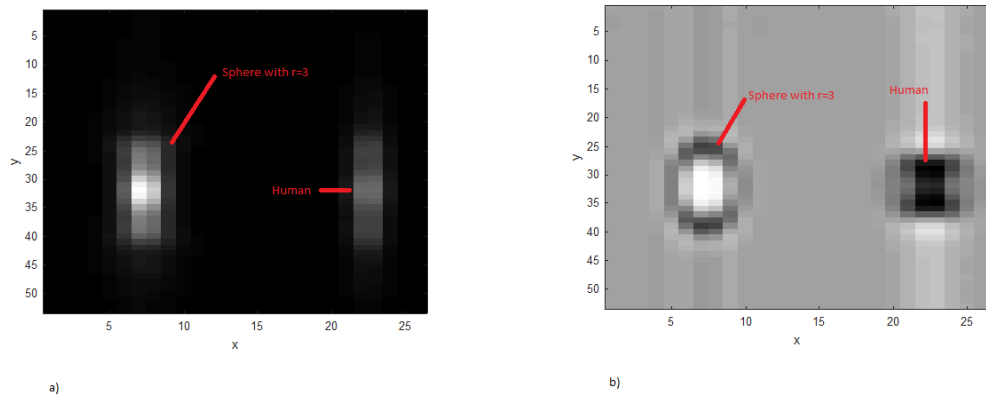


Figure D.4: a) The image of the energy sum of the top view of the 3-D data created by combining the B-Scan data b)C-Scan image at depth= 300

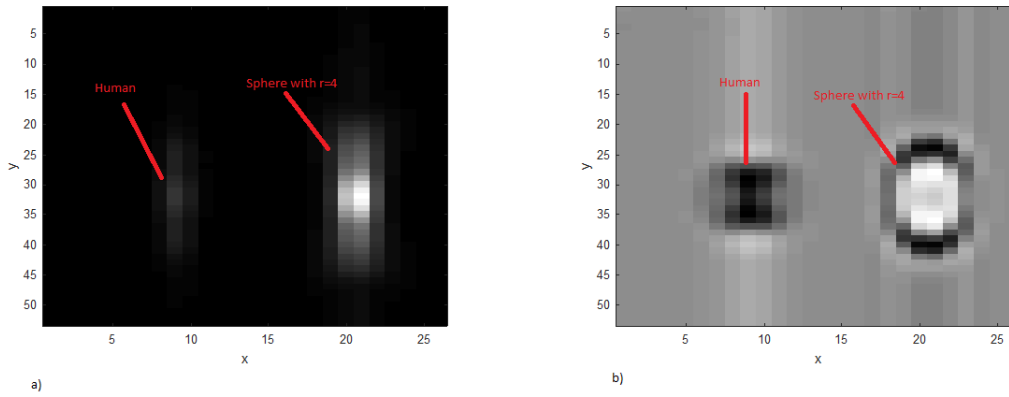


Figure D.5: a) The image of the energy sum of the top view of the 3-D data created by combining the B-Scan data b)C-Scan image at depth= 300

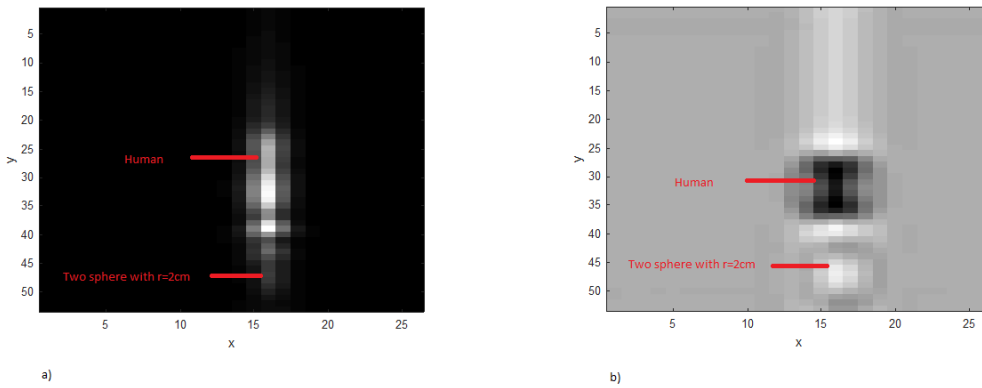


Figure D.6: a) The image of the energy sum of the top view of the 3-D data created by combining the B-Scan data b)C-Scan image at depth= 300

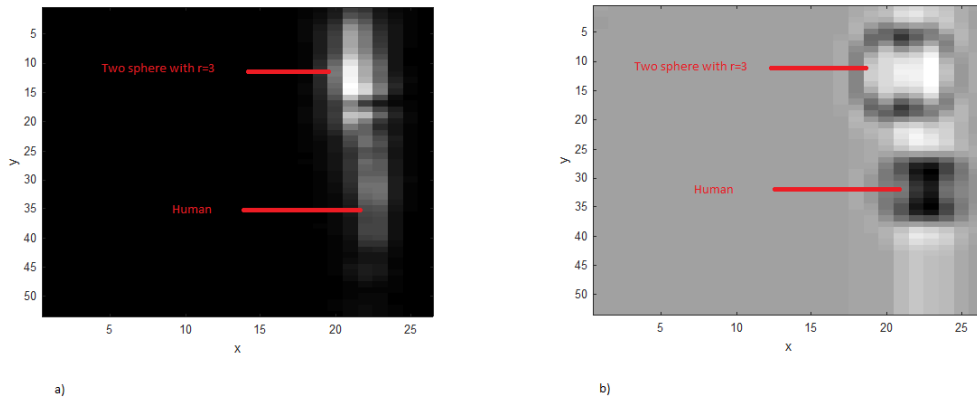


Figure D.7: a) The image of the energy sum of the top view of the 3-D data created by combining the B-Scan data b)C-Scan image at depth= 300

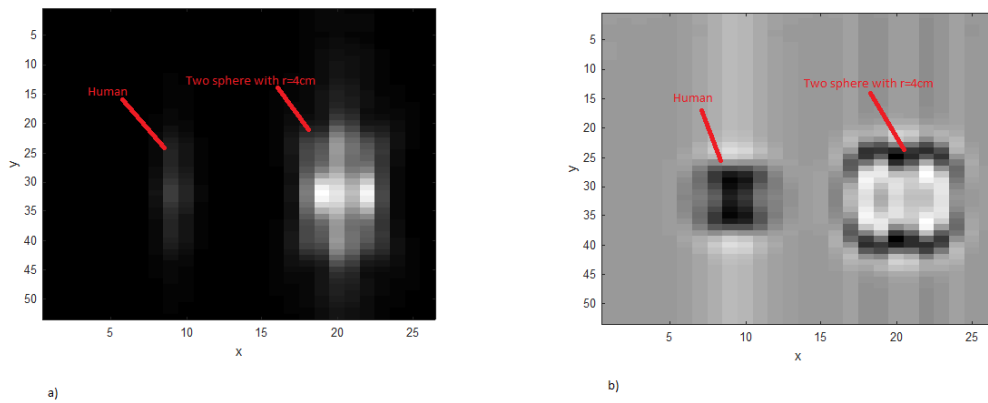
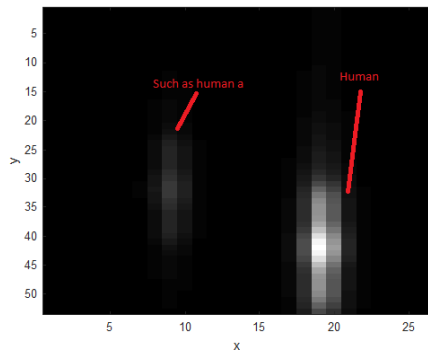
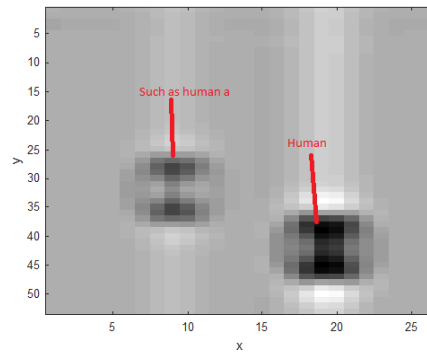


Figure D.8: a) The image of the energy sum of the top view of the 3-D data created by combining the B-Scan data b)C-Scan image at depth= 300

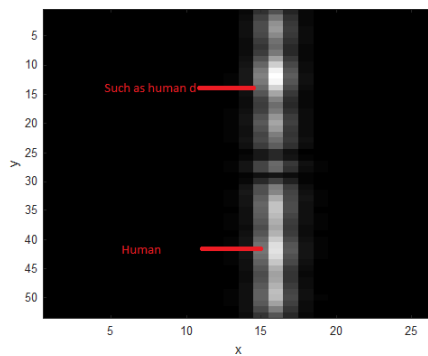


a)

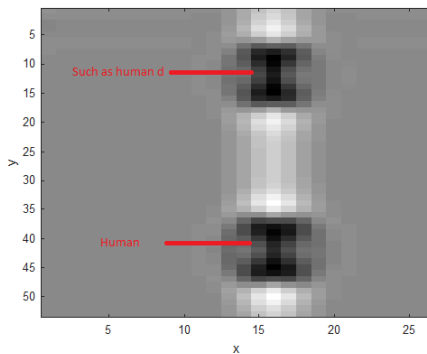


b)

Figure D.9: a) The image of the energy sum of the top view of the 3-D data created by combining the B-Scan data b)C-Scan image at depth= 300



a)



b)

Figure D.10: a) The image of the energy sum of the top view of the 3-D data created by combining the B-Scan data b)C-Scan image at depth= 300

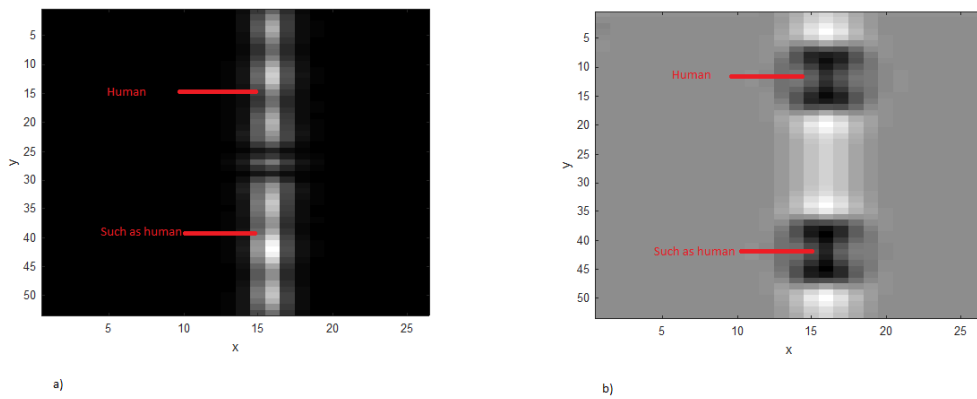


Figure D.11: a) The image of the energy sum of the top view of the 3-D data created by combining the B-Scan data b)C-Scan image at depth= 300

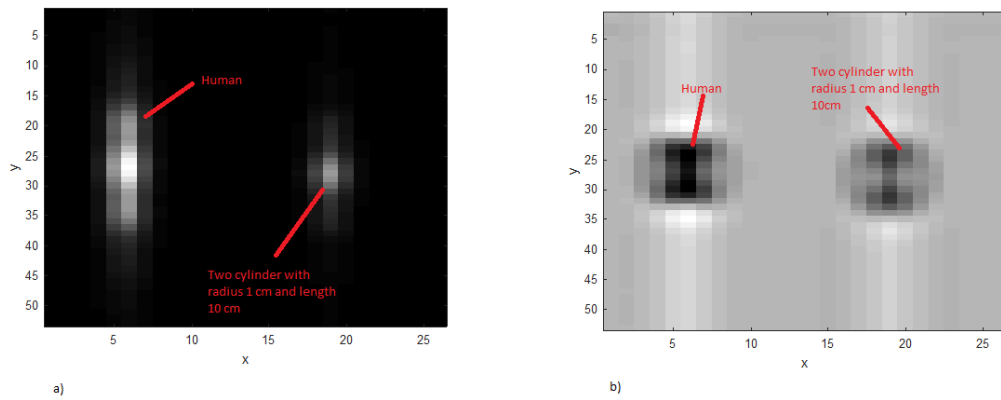


Figure D.12: a) The image of the energy sum of the top view of the 3-D data created by combining the B-Scan data b)C-Scan image at depth= 300

APPENDIX E

SIMULATION RESULT FOR 6 CM WALL

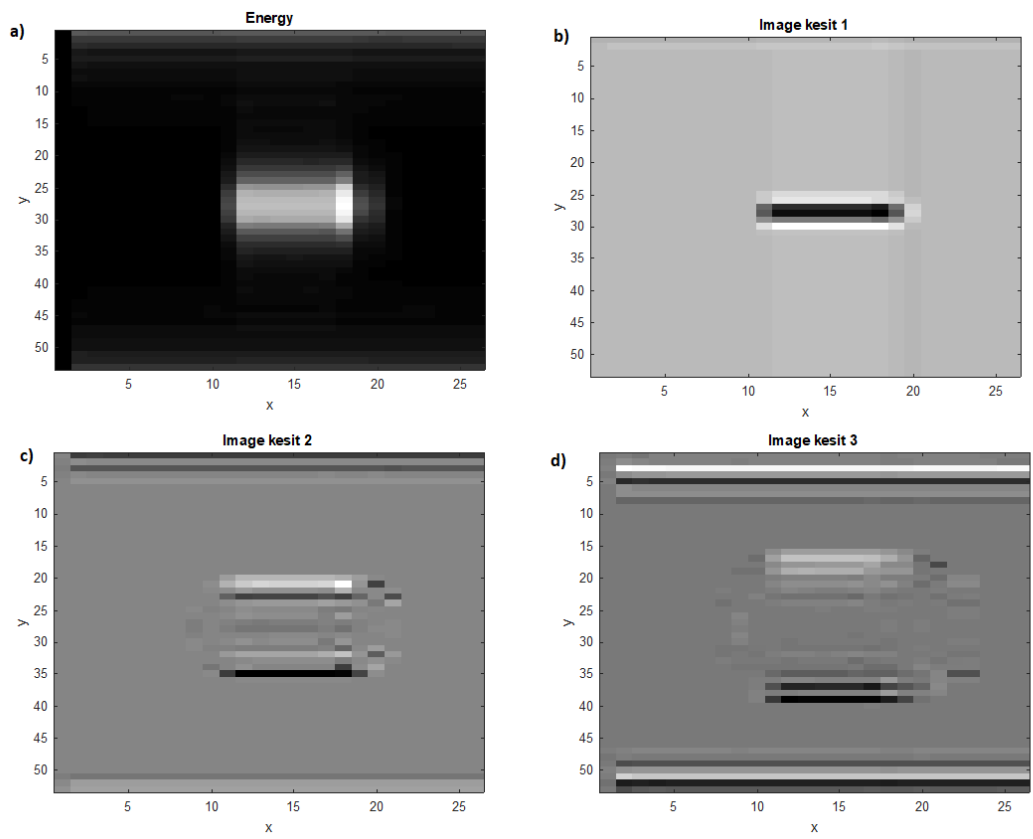


Figure E.1: a) The image of the energy sum of the top view of the 3-D data created by combining the B-Scan data b) C-Scan image at depth= 300 c) C-Scan image at depth= 450 d) C-Scan image at depth= 600